Stony Brook University

Development of a Simultaneous PET-MRI Breast Scanner

A Dissertation Presented

by

Bosky Ravindranath

to

The Graduate School

in Partial Fulfillment of the Requirements

for the Degree of

Doctor of Philosophy

in

Biomedical Engineering

Stony Brook University

August 2011

Stony Brook University

The Graduate School

Bosky Ravindranath

We, the dissertation committee for the above candidate for the Doctor of Philosophy degree, hereby recommend acceptance of this dissertation.

David J. Schlyer, Ph.D. – Dissertation Advisor
Adjunct Professor, Department of Biomedical Engineering
Senior Scientist, Brookhaven National Laboratory

Terry Button, Ph.D. – Chairperson of Defense
Associate Professor, Departments of Radiology and Biomedical Engineering

Paul Vaska, Ph.D.
Adjunct Professor, Department of Biomedical Engineering
Scientist, Brookhaven National Laboratory

Dardo Tomasi, Ph.D.
Senior Associate Scientist, Laboratory for Neuroimaging, National Institutes of Health

Craig Woody, Ph.D.
Senior Physicist
Physics Department, Brookhaven National Laboratory

This dissertation is accepted by the Graduate School.

Lawrence Martin
Dean of the Graduate School

Abstract of the Dissertation

Development of a Simultaneous PET-MRI Breast Scanner

by

Bosky Ravindranath

Doctor of Philosophy

in

Biomedical Engineering

Stony Brook University

2011

Imaging techniques have played a major role in the diagnosis, treatment and management of breast cancer. A significant drop in mortality rates among breast cancer patients was observed over the past decade and this has been attributed primarily to widespread screening programs using X-ray mammography. As we advance our knowledge of this disease and move towards more tailored treatment options, it has become apparent that there is a need for more advanced and dedicated imaging techniques that will allow for more thorough evaluation of the disease non-invasively.

To address this need, a simultaneous PET-MRI breast scanner was built. Positron emission tomography (PET) can provide functional or biological information of

the tumor under study. With advances in radiotracer chemistry, information that was only available after biopsy and evaluation of tumor tissue, can now be obtained non-invasively using PET imaging. The addition of Magnetic Resonance Imaging (MRI), an imaging modality that provides high-resolution structural image, will result in an imaging modality that combines the best of both worlds-anatomy and physiology. Hence, such a device will allow earlier diagnosis, and better patient care, along with being an important research tool.

The simultaneous PET-MRI system consists of a PET ring that is MRI compatible. The PET ring has a transaxial imaging field of view of 108 mm and axial height of 18 mm. The ring is mounted on a translation device that allows for greater area coverage as necessary. The PET ring is positioned within the radio frequency coil of a dedicated breast MRI system, onto which the patient is positioned in the prone position. The breast tissue as a result is in the field of view of both the PET and MRI systems, thereby facilitating simultaneous PET-MRI imaging. The system was tested and optimized to minimize inter-modality interference and simultaneous PET-MRI studies were conducted on breast cancer patients. The development of this device and its performance evaluation, both on the bench and in the clinical setting is the work of this thesis

Contents

List of Figures

List of Tables

Acknowledgements

The work presented in this thesis has only been possible through the help and contributions of many. Some people have been more directly involved, through discussions, through assistance and guidance in experiments, in finding solutions to the problems encountered and through their scientific perspective during the course of the project. Others have been less directly involved, but have been equally influential just through their presence in my life during the course of this work. This thesis is a reflection of the scientist and person I have strived to be with the help and example of my colleagues and mentors.

First and foremost, I would like to thank my advisor and mentor, Dr. David Schlyer. Thank you for accepting me into your group and bringing exciting projects my way. Thank you for your scientific guidance and vast and varied knowledge and experience that I have had the pleasure to draw from while dealing with the many perplexing challenges during the course of this work.

I would like to thank Dr. Craig Woody for his valuable insights, guidance and example that has helped keep the projects on track, Dr. Paul Vaska for his help with understanding PET data and analysis techniques and Dr. Martin Purschke for constantly introducing us to the "latest and greatest" in the field which allowed much of the computational work presented here to be done in an efficient manner and within a reasonable time frame.

I would like to thank Sean Stoll, Bill Lenz and Ritchie Ruggierio for making the numerous phantoms and mechanical devices that were essential for the work presented here, my Stony Brook colleagues- Dr. Sudeepti Southekal, Dr. Srilalan Krishnamoorthy and Dr. Sri Harsha Maramraju for sharing their knowledge with me, and all members of the radiotracer chemistry group for providing support - be it radiotracer delivery or subject recruitment.

I would like to thank colleagues from Aurora Imaging Technology - Dr. Xiaole Hong, Dr. Ken Cheng, Dr. Aiping Jiang, Dr. David Bennett, Dr P.-J Huang, Olivia Cheng, Jinnia Huang and the staff of the Taipei Medical University Hospital for making the clinical studies and MRI tests possible.

Finally, I would like to thank my family- my parents, R. Ravindranath and Vimala Ravindranath, my sister and now a teacher, Barkha Ravindranath and Dr. Anselm Vossen for being the people they are. This thesis is dedicated to you.

Overview

Imaging techniques have played a major role in the diagnosis, treatment and management of breast cancer. A significant drop in mortality rates among breast cancer patients was observed over the past decade and this has been attributed primarily to widespread screening programs using X-ray mammography. As we advance our knowledge of this disease and move towards more tailored treatment options, it has become apparent that there is a need for more advanced and dedicated imaging techniques that will allow for more thorough evaluation of the disease non-invasively.
To address this need, a simultaneous PET-MRI breast scanner was built. Positron emission tomography (PET) can provide functional or biological information of the tumor under study. With advances in radiotracer chemistry, information that was only available after biopsy and evaluation of tumor tissue, can now be obtained non-invasively using PET imaging. The addition of Magnetic Resonance Imaging (MRI), an imaging modality that provides high-resolution structural image, will result in an imaging modality that combines the best of both worlds- anatomy and physiology. Hence, such a device will allow earlier diagnosis, and better patient care, along with being an important research tool.
The simultaneous PET-MRI system consists of a PET ring that is MRI compatible. The PET ring has a transaxial imaging field of view of 108 mm and axial height of 18 mm. The ring is mounted on a translation device that allows for greater area coverage as necessary. The PET ring is positioned within the radio frequency coil of a dedicated breast MRI system, onto which the patient is positioned in the prone position. The breast tissue as a result is in the field of view of both the PET and MRI systems, thereby facilitating simultaneous PET-MRI imaging. The system was tested and optimized to minimize inter-modality interference and simultaneous PET-MRI studies were conducted on breast cancer patients. The development of this device and its performance evaluation, both on the bench and in the clinical setting is the work of this thesis.

The thesis is arranged in six chapters:

- Chapter 1 gives an overview of the anatomy of the breast and the different types of breast cancer. Both invasive and in situ carcinoma along with some of the challenges associated with each subtype with respect to breast cancer management is discussed.

An overview of the staging mechanism used by the AJCC is also given along with its corresponding prognosis. This chapter aims to emphasize the heterogeneity in breast cancer and also their apparent similarities, albeit their different prognosis, which makes their early and correct identification difficult and at the same time crucial.

- Chapter 2 gives an overview of the various imaging techniques employed in detection, diagnosis, staging and therapy evaluation of breast cancer. The current view of these techniques in the clinical setting and their drawbacks are also listed. The role of PET and MRI in breast cancer management along with the need for a simultaneous PET-MRI breast scanner is summarized.

- Chapter 3 focuses on PET physics and instrumentation. An overview of some of the current dedicated breast PET systems is given. A literature review of the development and current status of simultaneous PET-MRI instrumentation is presented.

- Chapter 4 describes the work done towards development of the various prototype PET systems for simultaneous PET-MRI breast imaging. This chapter describes the Monte Carlo simulations, benchtop PET tests and the simultaneous PET-MRI test results conducted with these prototype systems that lead to the development of the clinical prototype PET system.

- Chapter 5 describes the design of the clinical prototype PET system, the clinical protocol employed and data acquired using the simultaneous PET-MRI prototype scanner in breast cancer patients.

- Chapter 6 discusses the conclusions derived from this work along with future directions.

Chapter 1

Breast Cancer

Breast cancer is the second leading cause of cancer death in women. According to the American Cancer Society, in the year 2010, an estimated 207,090 cases of invasive breast cancer and 54,010 cases of in situ breast cancer will be diagnosed. It is estimated that 39,840 women will die of breast cancer in the year 2010 [8]. It is clear from several studies that the mortality rates of breast cancer have steadily declined over the last decade. This has been primarily attributed to the widespread screening programs using x-ray mammography as well as the overall awareness in women about this disease.

1.1 Breast Anatomy

In the human female, the breast parenchyma is made up of segments called lobes along with a network of ducts, while the stroma and subcutaneous tissue consists of cartilage, fat, blood vessels, lymphatics and nerves.
Typically, each breast can contain anywhere between 10-20 lobes. Within each lobe are smaller units called lobules each of a diameter of 0.5-0.6 mm. The lobules are the milk producing glands of the breast and along with its associated ducts, are hormonally sensitive. Each lobule further consists of 10-100 secretory units called the alveoli.
The ductal network starts at or opens into the nipple and each nipple has approximately 10 of these ducts. They have a diameter of approximately 2 mm and they branch off into smaller ducts deep into the breast, collecting from the lobular units. A sketch of the network of lobules and ducts within the breast is shown in Figure 1.1. In younger women, the breast is primarily made of the lobular tissue. With age, these shrink, and are replaced by fat. The lobules and ducts are important with respect to the study of breast cancer, as it is postulated that most of the cancers of the breast originate in one of them.

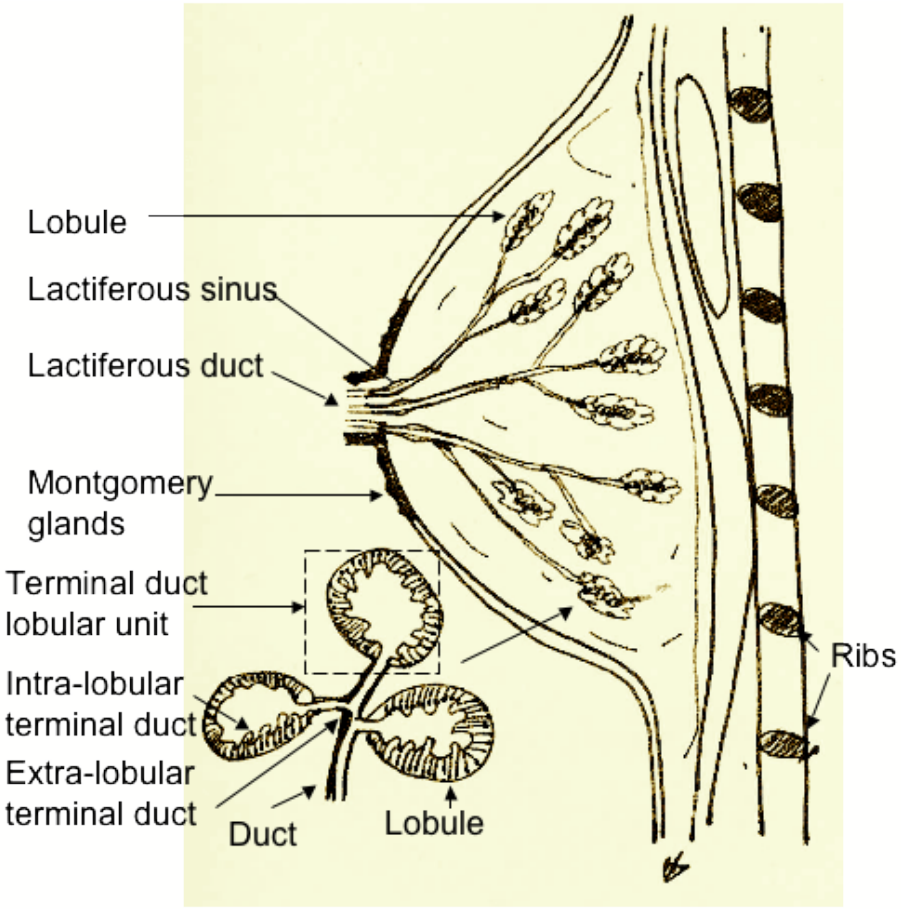

Figure 1.1: Micro anatomy of the breast

1.2 Types of Breast Cancer

1.2.1 In-situ Carcinoma

There are two kinds of in-situ carcinoma in breast cancer-Ductal Carcinoma In Situ or DCIS and Lobular Carcinoma In Situ or LCIS. As the name suggests, the neoplastic transformation develops within the duct or the lobules (the terminal ductal lobular unit) and are contained within the basement membrane-hence they are "carcinoma in situ". DCIS is the most common form of in situ carcinoma. In the year 2010, 54,010 new in-situ cases were expected to be diagnosed, with DCIS constituting 85% of it [1, 8].

- DCIS
  It is not exactly clear whether DCIS should be classified as cancer or not. Some clinicians choose to call it stage-0 carcinoma. The fraction of DCIS cases have been increasing over the past few decades. This is assumed to be mainly because of improvements in the detection capability of mammography units, although it cannot be ruled out that the incidence of DCIS itself has increased amongst women. Treatment for DCIS ranges from excision with radiation therapy to mastectomy [9]. The tricky aspect with DCIS is that although it is seen as a precursor to invasive lesions, not all DCIS will become invasive [10]. The key is to be able to identify and distinguish between the two so that patients can be treated appropriately.
  Architecturally, DCIS can be classified into 5 types-papillary, micropapillary, cribriform, solid and comedo.
  Another way to classify DCIS is by its nuclear grade. Nuclear grade refers to the size and shape of the nucleus and the percentage of tumor cells undergoing division. DCIS can be classified into 3 grades-Grade 1 or low grade, Grade 2 or intermediate grade, and Grade 3 or high grade. Patients with high grade lesions tend to have higher probability of local recurrence than low grade lesions. It has been noted that the comedo type of DCIS tend to be of high nuclear grade and are clinically aggressive, at the same time, it is possible that a single DCIS lesion may constitute several architectural subtypes. This poses a problem with respect to biopsy, where a small section of the tumor gets sampled, and hence may lead to inaccurate diagnosis.
  On a mammogram, DCIS in most cases presents itself in the form of micro-calcifications. However, these micro-calcifications are more pronounced and proportional to the size of the actual lesion in the comedo type of DCIS. Some of the non-comedo lesions (approximately 50 %) do not exhibit micro-calcifications and may be missed. Further, the extent of calcification in non-comedo lesions are not proportional to the physical extent of the associated DCIS, hence imaging with other techniques is needed to estimate the true size of the lesion [11].

- LCIS
  Lobular Carcinoma in situ, also known as lobular neoplasia, originates in the "terminal

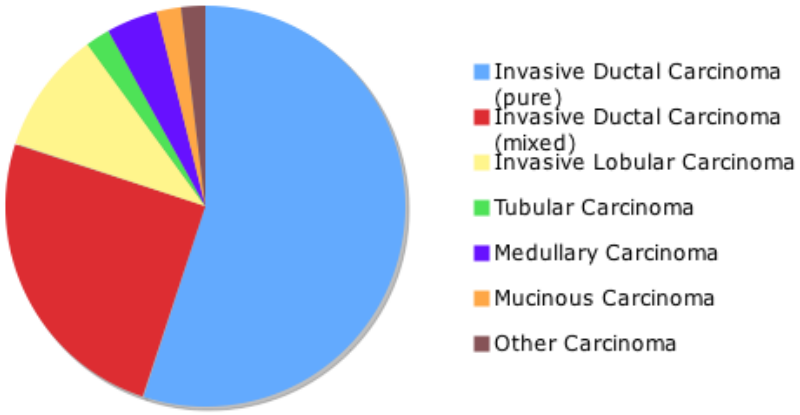

Figure 1.2: Relative occurrance of different kinds of invasive breast cancer in a population not screened by mammography, adapted from [2]

duct lobular unit" region of the breast. Its frequency of occurrance is low and its findings usually incidental-occasionally as microcalcifications on mammography and more likely as chance diagnosis in core biopsy specimens. It occurs mainly in younger women between 40-50 years of age. It is not clear what the occurence of LCIS means. It can be seen as marker of increased risk for subsequent infiltrating carcinoma [12]. Women with LCIS left untreated are at an 8-9 fold increased risk of developing invasive cancer than the general population [13].
Unlike DCIS, LCIS tends to be multifocal, multicentric and bilateral, which makes the treatment options difficult [14]. Treatment can range from mammography follow ups, to conservative treatment or excision. The challenge lies in identifying and distinguishing certain grades of LCIS from DCIS, as DCIS would require different management strategies, as they are more likely to grow quickly into infiltrating carcinoma. LCIS appears to grow into infiltrating carcinoma within 15-30 years post biopsy.

1.2.2 Invasive Carcinoma

The most common types of invasive carcinomas are invasive ductal carcinoma and invasive lobular carcinoma, which make up approximately 90 % of all invasive cancers. Figure 1.2 shows the relative fraction of the unscreened population that is diagnosed by various kinds of invasive breast cancer.

- Invasive Ductal Carcinoma
  This is most common form of invasive breast cancer and constitutes approximately 80 % of all invasive breast cancers. Invasive Ductal Carcinoma or IDC or IDC-NOS (Not Otherwise Specified), does not exhibit specific morphologic or histologic properties.

Usually, when a cancer does not fall in any other categories, it is considered to be of the IDC type. IDCs usually have spiculated margins, and their cells vary considerably in size. The 5 year overall survival rate for IDC is 84.1 % and they tend to metastasize into lungs, pleura, distant nodes and parts of the central nervous system.

- Invasive Lobular Carcinoma
  Invasive Lobular Carcinoma or ILC accounts for 8-14 % [1, 15, 16] of all invasive breast cancers. In comparison to IDC, ILC occurs in older, post-menopausal women. They tend to be multifocal, multi-central and bilateral in their occurrence and fail to form masses and have a diffuse structure that cannot be easily detected by a breast exam, mammography and even biopsy. Hence, it is difficult to catch ILCs at an early stage. Most ILCs, in comparison with IDCs, once detected, tend to be of larger size and have more hormone receptors (ER, PR). ILCs tend to metastasize into the peritoneum, ovaries and gastrointestinal tract [17]. The 5 year overall survival rate for ILC is 85.6 %

- Tubular Carcinoma
  Tubular carcinoma is a less frequently occurring invasive carcinoma, that occurs mostly in older women. Most tubular carcinomas are less than 1 cm in size, and appear as a spiculated mass on a mammogram. Pure tubular carcinoma is associated with very good prognosis, hence, it is crucial to identify the pure type from mixed tubular carcinoma, which makes thorough sampling of the lesion by biopsy crucial. If tubular carcinoma constitutes less than 50 % of the lesion, then the lesion is classified as invasive carcinoma NOS. Hence, an accurate means of quantifying the volumetric constitution of the tubular type is essential.

- Micropapillary and Papillary Carcinoma
  Invasive micropapillary and papillary carcinoma are rare forms of cancer, and make up 1 % and 2-3 % of all breast cancers respectively [2]. Prognostically, papillary carcinomas are associated with favorable outcomes while micropapillary carcinomas are reported to be clinically aggressive [18]. Micropapillary carcinomas are usually associated with axillary lymph node metastasis.

- Medullary Carcinoma
  Medullary carcinoma occurs in 2-5 % of all invasive breast cancers, and is usually associated with good prognosis [19]. They occur more frequently in women carrying the breast cancer (BRCA) gene mutation. When tumors contain more than 25 % of carcinoma of a type other than medullary, they are called atypical medullary carcinoma which has the characteristics of ductal carcinoma.

1.3 Staging and Prognosis in Breast Cancer

The American Joint Commission for Cancer (AJCC) recommends a classification technique for breast cancer based **T**umor size, presence of **N**odal metastasis, and presence of distant **M**etastases also known as TNM staging. TNM staging was introduced with the idea of standard classification of breast cancer for prognostic assesment and treatment options. With advancement in the understanding of breast cancer, and imaging techniques, the classification levels are updated accordingly. The most recent revision, the 7^{th} edition of the AJCC manual ([20]) for TNM classification of breast cancer is listed in Table 1.1, and the staging groups are shown in Table 1.2. The 5 year survival rates for breast cancer patients using the AJCC staging terminology in shown in Table 1.3

Primary Tumor (T)	
TX	Primary tumor cannot be assessed
T0	No evidence of primary tumor
Tis	Carcinoma in situ
Tis (DCIS)	Ductal Carcinoma in situ
Tis (LCIS)	Lobular Carcinoma in situ
Tis (Paget's)	Paget's disease of the nipple not associated with invasive carcinoma and or DCIS/LCIS
T1	Tumor $\leq$ 20 mm in greatest dimension
T1mi	Tumor $\leq$ 1 mm in greatest dimension
T1a	Tumor >1 mm but $\leq$ 5 mm in greatest dimension
T1b	Tumor > 5 mm but $\leq$ 10 mm in greatest dimension
T1c	Tumor >10 mm but $\leq$ 20 mm in greatest dimension
T2	Tumor > 20 mm but $\leq$ 50 mm in greatest dimension
T3	Tumor > 50 mm in greatest dimension
T4	Tumor of any size with direct extension to the chest wall and/or the skin
T4a	Extension to the chest wall, not including only pectoralis muscle adherence/invasion
T4b	Ulceration and/or ipsilateral satellite nodules and/or edema of the skin that do not meet the criteria for inflammatory carcinoma
T4c	Both T4a and T4b
T4d	Inflammatory carcinoma
Regional Lymph Nodes (N)	

Clinical	
NX	Regional lymph nodes cannot be assessed (eg- previously removed)
N0	No regional lymph node metastasis
N1	Metastases to movable ipsilateral level I, II axillary lymph node(s)
N2	Metastases in ipsilateral level I, II axillary lymph nodes that are clinically fixed or matted; or in clinically detected (eg- through imaging) ipsilateral internal mammary nodes in the absence of clinically evident axillary lymph node metastases
N2a	Metastases in ipsilateral level I, II axillary lymph nodes fixed to one another (matted) or to other structures
N2b	Metastases only in clinically detected ipsilateral internal mammary nodes and in the absence of clinically evident level I, II axillary lymph node metastases.
N3	Metastases in ipsilateral infraclavicular (level III axillary) lymph node(s) with or without level I, II axillary lymph node involvement; or in clinically detected ipsilateral internal mammary lymph node(s) with clinically evident level I, II axillary lymph node metastases; or metastases in ipsilateral supraclavicular lymph node(s) with or without axillary or internal mammary lymph node involvement.
N3a	Metastases in ipsilateral infraclavicular lymph node(s)
N3b	Metastases in ipsilateral internal mammary lymph node(s) and axillary lymph node(s)
N3c	Metastases in ipsilateral supraclavicular lymph node(s)
Pathologic(PN)	
pNX	Regional lymph nodes cannot be assessed
pN0	No regional lymph node metastasis identified histologically
pN0(I-) No regional lymph node metastases histologically, negative IHC	

pN0(I+) Malignant cells in regional lymph nodes no greater than 0.2 mm	
pN0(mol-)	No regional lymph node metastases histologically, negative molecular findings
pN0(mol+)	Positive molecular findings but no regional lymph node metastases detected by histology or IHC
pN1	Micrometastases or metastases in 1-3 axillary lymph nodes; and/or internal mammary nodes with metastases detected by sentinel lymph node biopsy but not clinically detected
pN1mi	Micrometastases (greater than 0.2mm and/or more than 200 cells, but none greater 2.0 mm)
pN1a	Metastases in 1-3 axillary lymph nodes, at least one metastasis greater than 2.0mm
pN1b	Metastases in internal mammary nodes with micrometastases or micrometastases detected by sentinel lymph node biopsy but not clinically detected
pN1c	Metastases in 1-3 axillary lymph nodes and in internal mammary lymph nodes wit micrometastases or macrometastases detected by sentinel lymph node biopsy but not clinically detected
pN2	Metastases in 4-9 axillary lymph nodes; or in clinically detected internal mammary lymph nodes in the absence of axillary lymph node metastases
pN2a	Metastases in 4-9 axillary lymph nodes (at least one tumor deposit greater than 2.0 mm)
pN2b	Metastases in clinically detected internal mammary lymph nodes in the absence of axillary lymph node metastases

pN3	Metastases in 10 or more axillary lymph nodes; or in infraclavicular (level III axillary) lymph nodes; or in clinically detected ipsilateral internal mammary lymph nodes in the presence of one or more positive level I, II axillary lymph nodes; or in more than three axillary lymph nodes and in internal mammary lymph nodes with micrometastases or macrometastases detected by sentinel lymph node biopsy but not clinically detected; or in ipsilateral supraclavicular lymph nodes
pN3a	Metastases in 10 or more axillary lymph nodes (at least one tumor deposit greater than 2.0 mm); or metastases to the infraclavicular (level III axillary lymph) nodes
pN3b	Metastases in clinically detected ipsilateral internal mammary lymph nodes in the presence of one or more positive axillary lymph nodes; or in more than three axillary lymph nodes and in internal mammary lymph nodes with micrometastases or macrometastases detected by sentinel lymph node biopsy but not clinically detected
pN3c	Metastases in ipsilateral supraclavicular lymph nodes
Distant Metastases	
M0	No clinical or radiographic evidence of distant metastases
cM0(I+)	No clinical or radiographic evidence of distant metastases, but deposits of molecularly or microscopically detected tumor cells in circulating blood, bone marrow, or other nonregional nodal tissue that are no larger than 0.2 mm in a patient without symptoms or signs of metastases
M1	Distant detectable metastases as determined by classic clinical and radiographic means and/or histologically proven larger than 0.2 mm

Table 1.1: TNM classification according to the 7th edition of the AJCC

Anatomic Stage/Prognostic Groups			
Stage 0	Tis	N0	M0
Stage IA	T1	N0	M0
Stage IB	T0	N1mi	M0
	T1	N1mi	M0
Stage IIA	T0	N1	M0
	T1	N1	M0
	T2	N0	M0
Stage IIB	T2	N1	M0
	T3	N0	M0
Stage IIIA	T0	N2	M0
	T1	N2	M0
	T2	N2	M0
	T3	N1	M0
	T3	N2	M0
Stage IIIB	T4	N0	M0
	T4	N1	M0
	T4	N2	M0
Stage IIIC	Any T	N3	M0
Stage IV	Any T	Any N	M1

Table 1.2: Staging according to the 7th edition of the AJCC

Stage	5 year survival rate
0	93 %
I	88 %
IIA	81 %
IIB	74 %
IIIA	67 %
IIIB	41 %
IIIC	49 %
IV	15 %

Table 1.3: 5 year survival rates for various stages of breast cancer [6]

Chapter 2

Imaging in Breast Cancer

2.1 X-Ray Mammography

X-Ray Mammography is the most widely used screening technique for breast cancer, and has been responsible for the decrease in the mortality rates associated with the disease. The American College of Radiology recommends annual mammography screening in women starting at the age of 40 years and for women with high risk of breast cancer, the age of 30 years. Although mammography is useful as a screening tool, there are a number of drawbacks associated with it.

Large randomized breast cancer screening trials such as Health Insurance Plan (HIP) of New York and Canadian National Breast Cancer Screening Studies (CNBSS-I and II) have helped understand the role of breast cancer screening using mammography. These studies have shown that screening using mammography results in earlier detection of breast cancer, hence, better survival rates. Retrospective examination of results from these studies has also shown that mammography itself is an independent prognostic factor, i.e. the fact that a tumor was detected using mammography leads to a better prognosis [21]. Tumors detected by mammography tend to be more slowly growing than those detected symptomatically. These findings indicate that mammography is biased towards detecting less dangerous tumors, increasing the importance for an imaging modality that can reliably image both slowly growing and more importantly, aggressive tumors, which are associated with poor survival rates.

Of relevance is the finding about interval or incidence cancers, i.e., cancers that are clinically detected less than one year after the last mammographic screening and more than one year later respectively. Interval/incidence cancers have poorer prognosis than screen detected cancers and have poor survival rates-not significantly different from the control group which did not receive mammographic screening. In the HIP trial, 40% and 7% of cancers detected in the interval/incident group were stage II and stage III/IV respectively, only 51% belonged to stage I. In contrast, 76% of cancers detected by screening mammography were

stage I; only 20% and 4% were stage II and III/IV respectively. In the CNBSS studies, interval/incidence cancers had the highest proportion of stage III/IV cancer-22% for CNBSS-1 and 18% for CNBSS-2. The adjusted relative risk for breast cancer death was 53% more in interval/incidence cancers than in the screen detected group, even greater than the relative risk in the control group where the risk was 36% greater than the screen detected group. Another study showed that the sensitivity of mammography for detecting invasive cancer was only 68.6% in younger women (less than 50 years of age) [22].

These findings call for a re-examination of the current emphasis placed on mammography as the primary screening tool. Interval/incidence cancers were either missed by mammography or occurred within the time period between annual screenings. Identification of such tumors could bring down breast cancer mortality rates significantly, especially in younger women [23]. Data indicates the need for imaging modalities capable of greater sensitivity to morphological changes (e.g.-MRI) as well as functional changes (e.g.-PET) since functional changes often precede morphological changes.

The false positive rate associated with mammography is substantial. Retrospective analyses of the Stockholm trials have shown that mammography presented at least one false positive result in 24% of women, majority of which resulted in a biopsy [24]. The uncertainty associated with mammographic findings and false positive rates have resulted in lower cancer yields per breast biopsy (% of women who had breast biopsy and received a diagnosis of breast cancer within 12 months of screening). The overall cancer yield per breast biopsy was only 25.8% in [22]. The overall positive predictive value (PPV-percentage of women with abnormal mammography who received a diagnosis of breast cancer within 12 months of screening) of mammography was only 3.1%. Women with at least one first-degree relative with breast cancer had higher PPV (3.7%) than those without (2.9%). This increase could be due to the increased attention paid by radiologists in determining the outcome of tests in patients with a known history of breast cancer as suggested in [22] hence indicating the role of additional information in improving PPV.

In the U.S. and the U.K., 2.3%-3.4 % of first screening mammograms and 0.8%-1.7% of subsequent mammograms result in a biopsy. PPV for breast biopsies performed as a result of abnormal mammograms range from 12% at 40 years of age, increasing steadily at a rate of 0.8%-1.0% every year to 46% at 79 years of age [25]. The improvement seen with age could be due to factors such as increase in breast cancer incidence with age as well as better mammographic interpretation due to lower breast density in older women. The low values for breast biopsy PPV could benefit immensely from better functional and structural characterization of observed abnormalities.

The psychological aspects of false positive mammograms (FPMO) are not minor and have consequently prompted studies which show increased stress, anxiety, pain, temporary reduction in the quality of life and long term worries about breast cancer in patients following such a finding [26]. In the Stockholm trials, 64% of false positive cases were declared cancer free only by the end of six months from initial screening [24]. Other studies have shown

that 29% of women with FPMO reported prevalent anxiety for as long as 18 months after screening. Of the FPMO cases biopsied, 27% reported pain in the breast and 5% reported a FPMO as the worst experience in their life [27].

Mammography sessions by themselves are often associated with pain and discomfort. A Finnish study (n=700) reported that 61% of patients experienced some pain, 59% reported discomfort and 4% experienced severe pain or discomfort during mammography [28]. A more recent Portuguese study (n=2164) reported that 90% of patients experienced discomfort, of which 12% reported intense pain [29]. Pain and discomfort is of particular concern for women who have undergone surgical treatments. The most common surgical treatments for women diagnosed with breast cancer are lumpectomy and mastectomy. Women undergoing lumpectomy often undergo radiation treatment and are asked to continue their annual screening mammograms to detect recurrence. Women who undergo lumpectomy with or without radiation experience significant pain during their mammographic examinations. A study showed that the pain associated with mammography is 43% greater in the treated breast in comparison to the untreated breast most likely due to sensitivity of the breast to compression. Women who have undergone lumpectomy and irradiation experience 60% greater pain in the treated breast as opposed to a 23% increase in the lumpectomy only group [30]. Although not shown to affect the diagnostic value yet, women undergoing post lumpectomy mammograms allow lesser compression of their breast.

The psychological impact and pain associated with mammography and FPMO has not been proven to deter women from subsequent screening, but the overall amount of discomfort associated with it is substantial and with the current screening recommendation for women over 40, breast cancer screening procedures must be as comfortable and stress free as possible.

2.2 Ultrasound

The role of ultrasound in breast cancer is primarily in distinguishing solid masses from cysts [1, 31]. Ultrasound has an accuracy ranging from 96-100 % in identifying simple cysts. Ultrasound is not recommended as a screening tool by itself, but as an adjunct to mammography or in circumstances where mammography is not possible or the findings are inconclusive. Examples of such cases are women with high density breasts with a palpable mass not readily seen on a mammogram, in cases where the mammogram is negative, in detection of breast abscess where mammography may not be possible due to pain on compression and in evaluating masses that are not accessible by mammography (e.g. too close to the chest wall or involving lymph nodes). Ultrasound is also useful in guiding biopsies such as aspiration of a cyst or solid mass as it can provide real time images for such procedures. However, the accuracy and performance of ultrasound is highly dependent on the technician using the system.

Distinguishing a solid mass as benign or malignant is not straightforward with ultrasound, and its use for this purpose is not widely accepted in the clinical community. There have

been attempts to find features that distinguish solid lesions into benign and malignant, e.g. it has been observed that benign masses tend to have an ellipsoid shape, while malignant masses tend to have irregular shapes. Despite this, the primarily role of ultrasound remains in identifying cysts and in guiding biopsies.

2.3 PET in Breast Cancer

PET can be used in all stages of breast cancer management, from initial diagnosis to monitoring of therapeutic response. However, its clinically accepted role is in monitoring therapeutic response, in identifying distant metastasis, in restaging breast cancer and when other imaging modalities do not offer a clear evaluation [32]. The rather limited role of PET in breast cancer is primarily due to the fact that commercially available PET scanners have a spatial resolution and sensitivity that does not allow accurate detection and quantitation of tumors of less than 1 cm in size [33]. Due to this, primary breast tumors, residual disease and lymph node involvement (which are often small and of low grade) cannot be reliably evaluated and hence PET cannot be used as a screening tool. Apart from this, PET is also an expensive imaging modality in comparison with a mammogram or an ultrasound, and involves radiation dose to the patient.

The most widely used radiotracer in PET for detecting cancer/metastases is [^{18}F]-FDG (or 2-Deoxy-2-[^{18}F]fluoroglucose). The use of this glucose analog in being able to identify cancers began with the identification of the "Warburg Effect". This effect is named after Otto Warburg, who observed that cancer cells exhibit increased aerobic glycolysis, and that the rate of glycolysis is proportional to the rate of tumor growth [34, 35]. PET exploits this phenomenon when using the [^{18}F]-FDG radiotracer to give a quantitative or qualitative estimates of the rate of glucose consumption. Tumor cells uptake FDG, and undergo phosphorylation to FDG-6P. Unlike glucose, that gets phosphorylated to Glucose-6P, and further undergoes glycolysis, FDG-6P remains metabolically trapped as it does not get dephosphorylated and is unable to further cross cell membranes [36]. Specific uptake value (SUV) is a qualitative measure of radiotracer uptake, and is commonly used in the clinic due to its ease of computation. SUV is defined as follows:

$$\text{SUV} = \frac{\text{mCi/cc in tissue}}{\text{mCi of tracer injection/body weight}} \tag{2.1}$$

SUV measure can be tracked for a patient over the course of treatment, and the change or lack of change in the SUV value could indicate whether the treatment is working or not. For example, studies have shown that a decline in SUV by around 50 % after therapy is indicator of a "responder", whereas no or modest change in the SUV indicates the patient is a "non responder" to that treatment. Hence, PET can be potentially used to identify if a treatment is not working and change it accordingly. Some studies have reported that this

can be identified as early as after the first round of treatment. For example, an SUV value below 55 % of the pre-treatment SUV, is indicative of a responder, and this can be identified correctly with a sensitivity and specificity of 100 % and 85 % respectively [37]. These changes reflected by PET occur before structural changes occur in the tumor, and hence cannot be identified by structural imaging techniques. Other studies have also demonstrated that more quantitative parameters such as changes in FDG rate parameters, e.g. a low glucose metabolism to glucose delivery ratio is indicative of favorable therapeutic response; glucose metabolism and transport rate were also found to be independent prognostic factors for disease free survival and overall survival rate [38]. FDG PET has a sensitivity of of 89 % and specificity of 84 % in identifying locoregional recurrence, and a sensitivity and specificity of 100 % and 97 % respectively for distant metastases respectively, hence making it a good follow up tool [39].

PET using radiotracers other than FDG have also been shown to predict tumor response to treatment. For example, the degree of ER blockade in patients with ER+ breast cancer treated with tamoxifen showed a significant decrease in FES (Flouroestradiol-17 beta) uptake between responder and non responders [40]. Other radiotracers with application in breast PET imaging are [^{18}F]-FLT (Fluorothymidine) for tumor proliferation imaging, [^{18}F]-Flouride, for imaging bone metastases, and [^{15}O]-Water for imaging blood flow [41]. Several studies have tried to find biological correlates to changes in FDG. A study by Bos and colleagues [42] found an association between FDG uptake and tumor microvasculature, Glut-1 expression, Hexokinase, concentration of tumor cells, tumor proliferation rate and hypoxia-inducible factor HIF-1 alfa. At the same time other studies show no or weak correlation between FDG and Glut-1 expression, steroid receptor status, percentage of tumor cells, and hence has not recommended FDG measures to reflect biological correlates such as cell profileration, histological grading, axillary lymph node involvement, and differentiation [43]. Other studies have found correlation between SUV and prognostic factors such as ER status (negative ER, higher SUV) and triple negativity (associated with higher SUV). Hence, the factors affecting FDG uptake in breast cancer is still under research, and is varied depending on the type of cancer. The Warburg effect, which triggered the role of PET in cancer imaging is being reconsidered to understand what truly causes the increase in glucose uptake in tumors.

2.4 MRI in Breast Cancer

MRI has been steadily gaining acceptance for its role in breast imaging-from initial detection to treatment monitoring. Although it is not recommended as a screening tool for the general population, the ACS has recommended MRI as an adjunct screening tool for those women who are at an increased risk for breast cancer (e.g.-family history, BRCA gene) [44]. Although MRI has been primarily viewed as an anatomical imaging technique due to its very high spatial resolution and excellent soft tissue contrast, newer techniques using MRI such as

dynamic contrast enhancement (or DCE) imaging provide functional information which is making it more attractive for breast imaging purposes. Several groups have applied this and other functional information that can be extracted from MRI in breast cancer patients under various stages of breast cancer management, with encouraging results. The application of MRI in breast imaging is a fast growing field and has probably not achieved its full potential yet. MRI has a reported sensitivity of 90 % and specificity of 72 %, as a result, MRI is seen as a high sensitivity but poor specificity device [45].

Morphologically, several criteria can be used to distinguish benign vs. malignant lesions [46]. If the boundary of the MRI detected lesion is spiculated as opposed to smooth, then that is indicative of malignancy. If the enhancement within a tumor is heterogenous, then this can be indicative of a lesion being malignant as opposed to a lesion that enhances uniformly. Another predictive factor of malignancy, can be the pattern of enhancement e.g.-a rim enhancement pattern is most likely indicative of malignancy. However, one needs to keep in mind that morphological characteristics by themselves cannot be used to make a diagnosis, since many benign lesions may also show some characteristics typically thought to indicate malignancy, e.g.-the rim enhancing pattern can also be observed in benign lesions with fat necrosis, and also cysts. Hence, another piece of information that can be obtained through contrast injection MRI is the time course of contrast kinetics (DCE kinetics) [47]. DCE involves MRI imaging of the lesion before and after a contrast injection (T1 relaxation time shortening, and usually Gadolinium based), and the time course of signal enhancement has been shown to have correlation with the type of tumor. If after contrast injection, the signal intensity in the lesion keeps on increasing with time during the intermediate phase (i.e. 2-3 mins. post injection), this kind of enhancement is called "progressive" enhancement. If the signal intensity within the lesion stops increasing and remains steady during the intermediate phase, it is called "plateau" enhancement. If the signal intensity, drops during the intermediate phase, this is called the "wash-out" pattern. This is illustrated in Figure 2.1.

The progressive pattern is associated with benign lesions, while the washout pattern is associated with malignant lesions. The plateau is a pattern with somewhat inconclusive diagnosis.

These patterns have also been used to predict response to therapy in breast cancer patients [48, 49]. Change in the size of the tumor and its volume is a major predictor of successful response to therapy [50]. For example, in a retrospective study by Loo and colleagues [51] in 54 breast cancer patients who underwent chemotherapy, it was observed that a change in the diameter of the lesion during the late enhancement period (450 s after contrast injection) is a predictor of final pathological response. The MRI scans were done after two courses of chemotherapy (patients were scheduled to receive three treatment courses). When the reduction in the size of the enhancement diameter is less than 25 %, it is an indicator of residual disease after therapy.

However, a more recent study by the same group also pointed out that the accuracy of MRI prediction of response to neoadjuvant chemotherapy is dependent on the type of

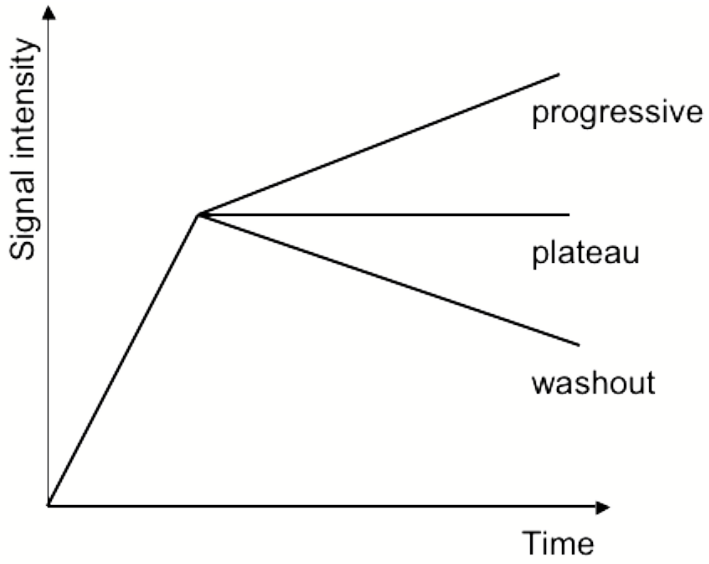

Figure 2.1: Dynamic contrast enhancement patterns

cancer [52]. The study noted that MRI parameters such as lesion morphology, size, and enhancement kinetics are accurate in predicting the response of triple-negative (ER, PR and HER-2 negative) or HER-2 positive disease but not in ER-positive or HER2-negative disease.

2.5 Need for a Simultaneous PET-MRI Breast Scanner

It is clear that no one imaging modality by itself can identify every type of breast cancer accurately, or provide enough information for prognosis or therapeutic strategies with reliability. Hence, the need for combined modality, that can use strengths of each modality to compliment the information provided by the other is evident. A dual modality, PET-MRI system is one such combination that can provide complimentary information and has the potential to improve patient care tremendously.

The main advantage of using this dual modality device will be its ability to characterize functional and structural status of the tumor simultaneously and in a shorter period of time than each modality separately. The device will have high sensitivity, afforded by MRI and the high specificity due to PET. Interval/incidence cancers will be detected with more accuracy using PET since biochemical changes precede morphological changes. PET/MRI is not limited by the density of breast and hence performs well in younger women or women undergoing hormone therapy. The PET ring will be adjustable in its size, hence is capable of imaging larger breasts. Since there is no compression involved, there will be minimal discomfort and due to the adjustable nature of the ring size, it is suitable for imaging overweight/obese women as well. The radiation dose will be similar for all patients.

This device will be useful in breast cancer screening as an adjunct to mammography. Due to the high false positive rates associated with mammography, positive or inconclusive MO findings could be followed by a scan using the PET-MR scanner before any biopsy or surgical intervention is ordered. It is envisioned that this scanner will replace mammography as a routine screening tool for women who fall in the high risk category, women with high breast density, women undergoing hormone therapy and those who have undergone surgical intervention [53].

2.5.1 Cancer Evaluation and Staging

TNM (Tumor size, Nodal Metastasis, Distant Metastasis) is the traditional system for staging breast cancer recognized by the AJCC. This staging mechanism is being constantly updated to include new findings or markers that have important prognostic value. Currently, there is no single imaging modality that can accurately stage a patient based on all the above three criteria. MRI with its high image resolution is the most appropriate for characterizing tumor size and extent. Nodal and distant metastasis can be characterized both using functional and morphological characteristics, i.e., with both PET and MRI. An ideal solution would be a whole body imaging modality using PET and MRI, however, such an instrument is currently not available and separate whole body MRI and PET scans are too expensive and cumbersome to be used on a routine basis. The proposed breast PET/MRI scanner provides a good compromise between the two imaging modalities, where one can obtain functional and structural information of cancer present in the breast using PET and MRI and use MRI for staging lymph nodes and distant metastasis. In addition to the use of FDG, the development of novel radiotracers and labeled drugs can be used to characterize other aspects of tumor biochemistry and also determine the bioavailability of a chemotherapeutic drug to the tumor. For example, [^{18}F]-FES can be used to identify the estrogen receptor (ER) status of the tumor [54]. Current methods of identifying ER status are invasive in nature (biopsy), however due to the heterogeneous nature of ER expression on tumors, inaccurate biopsy (sampling errors) and subsequent characterization of excised tumor sample can lead to false estimation of ER status. FES-PET using the proposed device can identify and quantify (with the aid of anatomic information using MRI) the ER receptor status and its hormone receptiveness, thereby reducing the number of biopsies and determining the most appropriate treatment course such as tamoxifen as opposed to conventional chemotherapy which is much more painful for the patient. In another example, the presence of hypoxia indicates the advanced nature of cancer; such cancers are not responsive to chemotherapy. Hypoxic tumors can be identified non-invasively using radiotracers such as FMISO ([^{18}F] fluoro-misonidazole) [55] and surgical intervention can be planned. Still another radiotracer ([^{18}F]-FLT) [56] allows the examination of tumor proliferative state [57]. Other radiotracers such as [^{18}F]-benzamides are being evaluated to image sigma receptors in breast cancer [58–60]. In addition, labeled drugs such as labeled taxanes anthracyclines can be envisioned to determine whether the drug gets to the tumor [61, 62] Recent advances in the field of MRI have shown its potential

in evaluating functional characteristics of a tumor. Contrast enhancement dynamics as well as more recent studies with the use of magnetic nanoparticles that can be coupled to antibodies show a promising future for the functional characterization of tumors using MRI. Tumor vascularity as seen on the MRI can be used to differentiate malignant from benign tumors [63]. Another advantage of simultaneous PET/MRI acquisition is the partial volume correction of PET data using the high resolution anatomical information provided by MRI. Partial volume correction will result in accurate quantification of standardized uptake values (SUV) and further improve the sensitivity and specificity of PET, especially for small tumors [64, 65]

The AJCC has been reviewing independent prognostic factors that can aid in the accurate staging of breast cancer. However, there is a lack of candidate factors that can be identified using non-invasive imaging techniques. With the advent of a multimodal imaging instrument such as the one proposed and its high image performance characteristics, quantitative measures such as SUV can become a prognostic factor and new non invasive measures can be identified. The use of a dedicated PET/MRI breast scanner could act as an invaluable tool to researchers in performing quantification and characterization studies due to superior functional and anatomic characterization with high accuracy and reliability. This will advance our understanding of qualitative and quantitative measures in both MRI and PET and potentially establish a relationship between the two.

2.5.2 Monitoring Response to Therapy

Monitoring the response of the tumor to therapy is a key factor in breast cancer management. Identifying the most appropriate treatment path is the first stage and PET-MRI has the potential to play a major role here. The development of new PET tracers which target different metabolic processes in the tumor as well as labeled chemotherapeutic drugs which will allow assessment of whether drug therapy actually reaches the tumor will even further enhance the capabilities of this device [58, 60]. As neoadjuvant chemotherapy becomes more widely used, the ability to predict chemotherapeutic response and the extent of residual disease by imaging methods is becoming increasingly important. Response monitoring revolves around tracking changes in functional and structural properties of the tumor. Both of these can be non-invasively quantified using PET and MRI. A drop in PET FDG SUV values have been seen for tumors that respond to therapy; SUV remains unchanged or increases when therapy is not working. FLT is another radiotracer that has shown promise in the evaluation of chemotherapeutic response; it is being used as an alternative to FDG because of its capability to image cellular proliferation hence providing a different perspective of tumor response. Volume changes in MRI have been found to predict tumor response and prognosis more accurately than simple tumor size measurements. PET becomes extremely useful in women who have undergone previous surgery because of its ability to differentiate scar tissue from tumor recurrence which is a challenge when using conventional imaging techniques such as mammography [53, 66].

Chapter 3

PET and PET/MRI- Physics and Instrumentation

3.1 PET Physics

The goal in PET imaging is the spatially accurate and quantitative mapping of radiotracer concentration and distribution within the object being imaged. The radionuclides used in the case of PET are proton rich and decay to their stable state through the emission of a positron along with a neutrino, as shown in Equation 3.1.

$$p^{+} \rightarrow n + e^{+} + \upsilon + energy \tag{3.1}$$

The positron interacts or annihilates with an electron in its surrounding medium and this results in the emission of two 511 KeV gamma rays that are 180 ± 0.25^{0} apart (as shown in Figure 3.1).

These two gamma rays are then detected by PET detector modules, and used for the reconstruction of distribution of the positron emitting radionuclide. The line joining the two interactions is termed as the "line of response" or LOR. The distance travelled by the positron before it annihilates with an electron depends on the kinetic energy of the element and the attenuation density of the medium through which the positron is traveling. This is called the positron range, and poses some of the fundamental limits in the resolution achievable by PET. Some of the commonly used radionuclides for PET imaging are flourine-

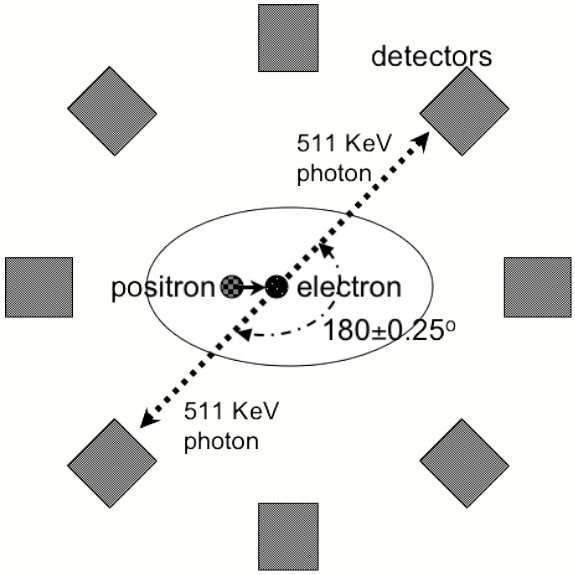

Figure 3.1: The Positron-Electron Annihilation

18 (^{18}F), carbon-11 (^{11}C), nitrogen-13 (^{13}N) and oxygen-15 (^{15}O). A summary of commonly used PET radioisotopes are presented in Table 3.1

Isotope	Half-life	Average β^+ Energy (MeV)	γ Energy (MeV)
C-11	20.4 m	0.385 (99.8%)	
O-15	122 s	0.735 (99.9%)	
F-18	110 m	0.250 (100%)	
I-124	4.18 d	0.686 (11.3%), 0.974 (11.3%)	1.691 (10.4%), 7.228 (10.0%), 1.509 (3.0%), 1.376 (1.7%), 1.325 (1.43%)

Table 3.1: Summary of commonly used PET radioisotopes

In order to obtain biologically meaningful images, the proton rich radionuclides are connected to compounds that can be used to study certain functions of the body or evaluate disease states. Consider the most common application of PET, i.e. detection of cancer. The most widely used radiotracer for this application is [^{18}F]-FDG or 2-Deoxy-2-[^{18}F]fluoroglucose is a glucose analog. This radiotracer can be used for tracking cancer cells because it has been observed that many types of cancers are glucose avid. Similarly, [^{15}O] $-$ H_2O can be used for studying flow, [^{11}C]-Raclopride can be used to study dopamine receptor status.

3.2 PET Instrumentation

The goal of any PET system is the detection and identification of the gamma rays emitted from a positron-electron annihilation event. PET scanners detect these gammas via detector modules that convert the gammas into a measurable quantity, usually a voltage and current pulse. These detector modules can assume several configurations, however, the most traditional and widely used configuration involves the use of scintillators along with electronic devices (photodetector) that convert the photons from the scintillators into an electrical signal. A schematic of a typical detector configuration is shown is Figure 3.2.

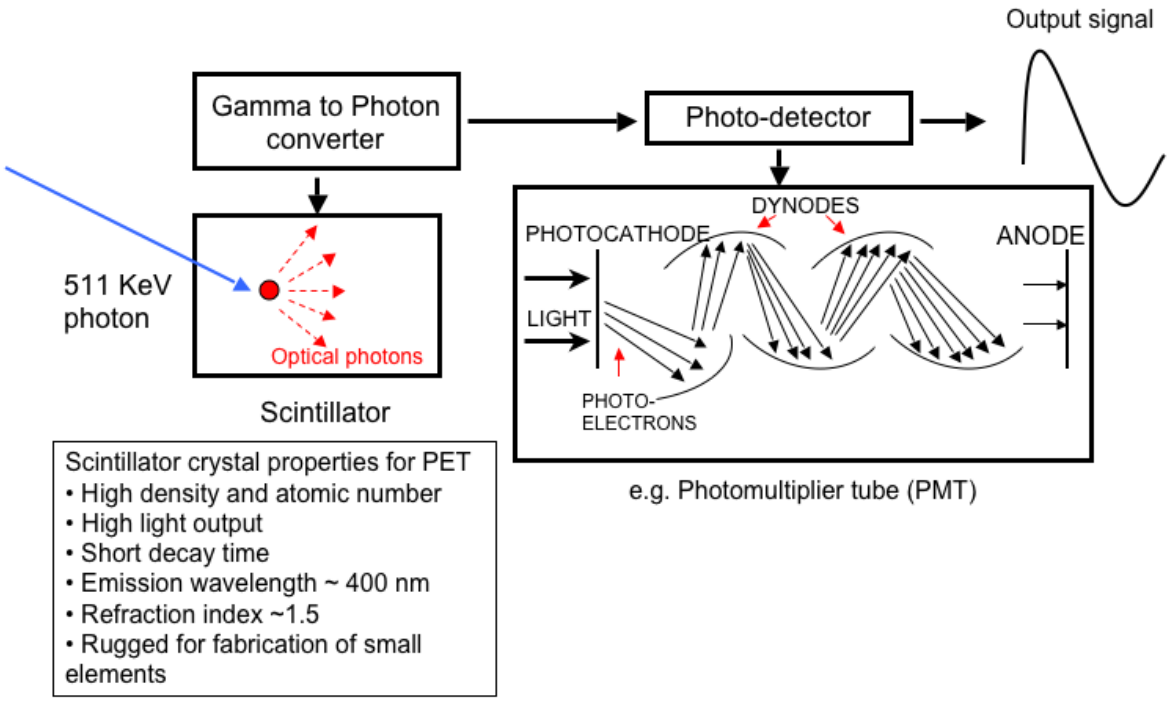

Figure 3.2: Schematic Arrangement of a PET Detector Module

Scintillators are high density crystals that can stop and convert a 511 KeV gamma ray into a photon shower. Some of the most commonly used scintillators in PET detectors along with their properties are summarized in Table 3.2. Photodetectors used in PET are explained in detail in Section 3.6.

The PET detector modules can be arranged in several different geometries, ranging from parallel plate to a cylindrical ring arrangement as shown in Figure 3.3.

Different geometric arrangements allow for different modes of data acquisition (e.g. tomographic vs. planar), LOR sampling efficiency, solid angle coverage of the object being imaged and hence the system sensitivity. Factors such as the cost of detector modules,

Scintillator	Density (gm/cm^3)	λmax(nm)	Photons/MeV	Decay Time (ns)
Lu_2SiO_5(Ce) or LSO	7.4	420	30,000	40
$Bi_4Ge_3O_12$ or BGO	7.13	480	8,200	60,300
BaF	4.89	185,220	1,800	0.8
		310	10,000	630
$Y_3Al_5O_{12}$(Ce) or YAG	4.55	590	11,000	50, 290
CsI(T1)	4.51	540	59,000	800
NaI(T1)	3.67	415	38,000	230
Y_2Si_5(Ce) or YSO	2.7	420	45,000	70

Table 3.2: Common Scintillators for PET and their Properties, adapted from [7]

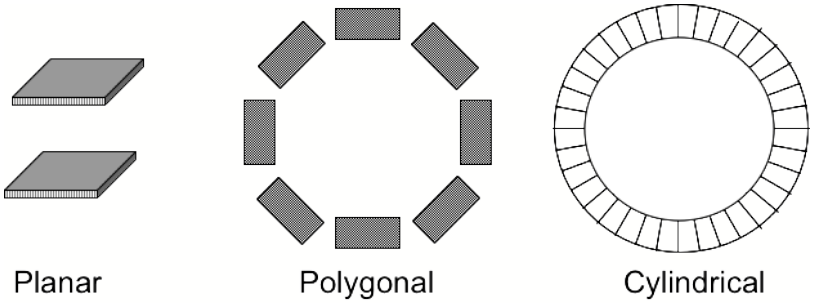

Figure 3.3: Various detector geometries in PET

space constraints and biological application dictate detector geometry. Most commercially available whole body systems have the PET detectors arranged in a cylindrical or ring configuration. Table 3.3 summarizes components and geometries of some of the commercially available systems.

3.3 Data Acquisition in PET

As described in the previous sections, PET data acquisition involves identification of the two gamma rays originating from a single positron decay or annihilation. This process is called coincidence detection, and is carried out by looking for two events occuring within a time window τ. Some PET scanners have electronics that perform the coincidence detection online (i.e. in hardware or firmware). Here, events that do not fall within the coincidence window are rejected, hence only coincidence events are recorded thereby reducing the amount of data that is captured by the scanner, and also reducing the requirement for high data rate capability of its associated electronics. Another data acquisition scheme involves recording all the events that trigger the PET system. This is called the "list mode format" data, and allows greater flexibility in data analysis and image processing, however, such schemes can

	GE-Advanced Nxi	ACCEL	ECAT HR+	ALLEGRO
Detector material	BGO	LSO	BGO	GSO
Crystal dimension (mm)	4x8.1x30	6.45x6.45x25	4.05x4.39x30	4x6x2
Crystals per detector block	36 (6x6)	64 (8x8)	64 (8x8)	-
Number of detector blocks	336	144	288	-
Detector ring diameter (mm)	927	824	824	860
Number of detector rings	18	24	32	-
Transaxial FOV (mm)	550	585	585	576
Axial FOV (mm)	152	162	155	180

Table 3.3: Summary of some of the commercially available whole body PET scanners

take up huge amounts of hard disk space, and also cause dead-time issues due to the high data rate requirement placed on the readout electronics.

The first step in PET data processing typically involves the correct identification of coincident events. Errors can be introduced at this stage either due to phenomenon such as scatter (due to Compton interactions) and randoms contributing to false coincidences as shown in Figure 3.4. Random coincidences occur when gammas from two separate positron annihilations fall within the system's timing window resulting in the detection of a false coincidence. To counter such problems, various data correction schemes can be applied to offset the introduced errors.

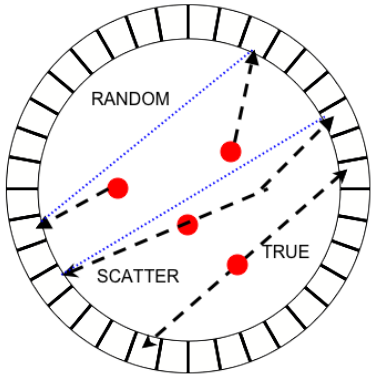

Figure 3.4: Coincidence detection in PET: black dashed lines indicates gamma ray track, blue dotted line indicates apparent line of response (LOR)

The detected coincidence events are arranged in what is called a sinogram. A sinogram is a representation or map of the number of coincidence events detected for a given line of response for a given dataset [67]. LORs are arranged as a 3D graph, where the Y axis denotes its angle and the X axis denotes the distance of the LOR from the center of the

scanner. The value at an X-Y position is the number detected coincidence events. Once the data has been sorted into a sinogram, image reconstruction can be carried out using iterative or analytical techniques.

3.4 PET Performance Measurements

The following parameters are commonly used to evaluate and compare performance of various PET scanners. The National Electrical Manufacturers Association (NEMA) has recommended ways to measure these parameters for both whole body system as well as small animal systems [68, 69]. However, no such standard for dedicated PET systems exist as of yet.

- Sensitivity

  The sensitivity of a system is a measure of the fraction of gamma rays that are detected by the PET system. The geometry of the PET scanner plays a major role in the system's sensitivity. Theoretically, it is a function of the geometric efficiency or the solid angle subtended by the system and the coincidence detection efficiency of its detector components as shown in the equations below [70].

$$\text{Coincidence Detection Efficiency}(\epsilon) = (1 - \mathrm{e}^{-\mu \mathrm{d}})^2 \phi^2 \tag{3.2}$$

  where μ is the attenuation coefficient of the detector or crystal, d is the thickness of the crystal and ϕ is the fraction of events detected.

$$\text{Geometric Efficiency } (\Omega) = 4\pi \sin[\tan^{-1}(A/D)] \tag{3.3}$$

  where, A and D are the axial length and diameter of the PET ring.

$$\text{Packing Fraction of detectors}(\psi) = \frac{\text{width x height}}{(\text{width} + \text{deadspace}) \text{ x } (\text{height} + \text{deadspace})} \text{ x } 100 \tag{3.4}$$

$$\boxed{\text{System Sensitivity } (\eta) = \frac{\epsilon^2 \psi \Omega}{4\pi} \text{x} 100} \tag{3.5}$$

  Sensitivity of a PET system is measured to a point source by estimating the coincidence count rate per second as a function of disintegrations per second of the source. Sensitivity can also be expressed as a percentage of coincidences detected per unit source of radioactivity.

- Spatial Resolution

  Spatial resolution is a measurement of the resolution with which two point sources can

be distinguished from one another. It is a function of several factors such as the width and height of the detectors which results in depth of interaction effects, the sensitivity of the system, the reconstruction techniques employed and on a more fundamental level is limited by the positron range and photon acollinearity of the radionuclide being imaged. Typically, spatial resolution is determined by imaging a point source less than 1 mm diameter, at various locations in the scanner FOV and measuring the point spread function of the reconstructed image. The point spread function is reported as the full width half maximum (FWHM) of the Gaussian fit of a profile plot of the point source. The resolution is measured at different locations within the field of view, primarily because of the varying sensitivity profile and depth of interaction effects. Depth of interaction is the uncertainty in the definition of the line of response width due to the incidence angle of the photon with respect to the detector.

- Count rate performance
  The count rate performance of the system is the efficiency with which a PET system and its associated electronics can acquire and record events as a function of the amount of radioactivity. PET systems usually have a dead time associated with them by virtue of the finite time taken by its associated electronics and detector modules to process an incoming event. Such dead times can pose a problem, and result in losses if the incoming data rate period is smaller than the system dead time.

- Energy Resolution
  This is a measure of the accuracy with which the energy of the annihilation photons can be determined. A system with good energy resolution is able to reject incoming photons that have undergone scatter (and thereby have less energy than the unscattered 511 KeV photons). Rejection of scatter events can reduce the number of false coincidences observed in the system, improving the image quality and count rate performance. Energy resolution of a system is usually measured by stepping the energy threshold of the system and measuring the singles or coincidence count rates.

- Timing Resolution
  Timing resolution is the accuracy with which time of the incoming annihilation photon can be determined and sets the width of the timing window for coincidence detection. Good timing resolution is essential for correct identification of coincidence events especially during high counting rates, and presence of background activity. The randoms fraction which is measure of false coincidences obtained from two unrelated annihilations is directly proportional on the width of the timing window and hence the timing resolution. The randoms rate between two detectors 1, 2 ($R_{1,2}$) can be expressed as:

$$\mathrm{R_{1,2}} = 2\tau \mathrm{N_1 N_2} \tag{3.6}$$

  where, N_1 and N_2 are singles count rates of detectors 1 and 2 respectively and 2τ is

the coincidence timing window width. Hence, good timing resolution is essential for effective randoms rejection.

3.5 Dedicated Breast PET Systems

Several research groups have been working on developing dedicated breast PET systems that have better performance than currently available whole body PET systems [71, 72]. The design and characteristics of some of these systems are summarized below:

Naviscan PEM System

The Naviscan PEM system is the only commercially available, FDA approved dedicated breast PET scanner [73, 74]. Detector Geometry: The PEM Flex Solo II, consists of two plates of detector arrays that translate across the breast held between compression paddles. The detector module consists of LYSO scintillation crystals (2 x 2 x 13 mm^3) coupled to position sensitive photomultiplier tubes. The two detector plates (each of imaging area 6 x 16.4 cm) translate and scan the breast area simultaneously, and hence are capable of an imaging field of view of 24 x 16.4 cm. Data is acquired in the list mode format and image reconstruction is performed using the Maximum Likelihood Expectation Maximization (MLEM) technique.

Performance Characteristics:

- Spatial Resolution- was measured using a capillary tube of 1 mm inner diameter. Images were reconstructed using MLEM. The mean in-plane spatial resolution was measured to be 2.58 $\pm$0.28 mm, 2.45 $\pm$ 0.32 mm and 2.39 $\pm$0.29 mm for a compression thickness of 3, 6 and 9 cm respectively. The cross plane spatial resolution of the system was worse and reported at 8.5 $\pm$0.32 mm, 7.34 $\pm$ 0.64 mm and 9.23 $\pm$0.65 mm at 3,6 and 9 compression respectively.

- Lesion Detectability- Spheres of diameter 4, 5, 8 and 20 mm were filled with activity of 4 x and 10 x the background. In visual detectability tests, the 4 mm sphere is not visible with 4 x activity levels, while for the 10x activity lesions, all the four spheres are discernible.

- Clinical Evaluation- 77 cases of biopsy proven or suspicious breast lesions were evaluated with the PEM device (PEM Flex). The device reported a sensitivity of 93 %, specificity of 83 %, PPV of 87 %, NPV of 91 %, and an overall accuracy of 88 %.

The PEM Flex Solo II system lacks a number of corrections such as for scatter, attenuation and count rate effects. As a result of this, quantitative inaccuracies in activity concentration were observed which ranged from 7 %- 85 %.

UC Davis dedicated breast PET/CT

This dedicated breast PET/CT system consists of two flat detector heads for PET imaging that is mounted on a gantry that allows translation in all three directions, and rotation along the main axis [75]. The PET system is operated in step and shoot mode. Each PET detector head consists of 16 modules of LSO crystal array-PSPMT combination arranged in a 4 x 4 matrix. Each crystal array is a 9 x 9 matrix of size 3 x 3 x 20 mm^3. The PET system has a field of view of 119 x 119 mm^2, and detector separation can be varied to accomodate different breast sizes.

Performance Characteristics:

- Spatial Resolution-was measured with a point source by filling a capillary tube of inner diameter 1 mm with [^{18}F]-FDG . These images were reconstructed using filtered back-projection algorithm. The measured average resolution at different locations within the field of view ranged from 2.53 mm (radially) and 3.01 mm (tangentially) FWHM at (x, y) location of (0 mm,-20 mm) to 3.52 mm FWHM (radially) and 3.77 mm (tangentially) at (- 10 mm, 0 mm). Spatial resolution was also measured using Maximum A-Priori (MAP) reconstruction, by placing a 0.8 mm line source in a uniform cylindrical phantom with source to background activity ratio of 400:1. Under this test condition, filtered back projection yielded a resolution (FWHM) of 3.28 mm radially, and 2.77 mm tangentially at the center of the scanner, while, MAP reconstruction yielded a resolution of 2.7 mm radially and 2.73 mm tangentially.

- Sensitivity-was measured using a 1 mm diameter [^{68}Ge] point source and was measured to be 1.64 % at the center of the scanner.

- Energy Resolution-Average energy resolution of the system was 25 %, and ranged from 18 % to 40 % within all the crystals.

The CLEAR PEM system

The Clear-PEM system consists of two parallel, planar detector heads. Each of the detector heads consists of 48 modules, wherein each module consists of a 4 x 8 array of LYSO crystal array coupled to a matching APD array (Hamamatsu S8550) on its front and back surface [76, 77]. This dual coupling provides depth of interaction information. Each LYSO crystal array element is of 2 x 2 x 20mm^3. Each planar head has an active area of 16.5 x 14.5 cm^2.
The scanner is designed mechanically to image patients in the prone position. The planar heads could rotate around the breast region to be imaged allowing sampling over multiple angles, as well as imaging of the axillary and chest wall region.
Image reconstruction is carried out using 3D-OSEM.

Performance Characteristics:

- Spatial Resolution-was measured using a 1 mm diameter ^{22}Na point source was 1.6 mm FWHM and 1.3 mm FWHM when deconvolving for the size of the source. These numbers represent the spatial resolution while taking the depth of interaction (DOI) information into account.
- Energy and Timing Resolution-The system has an energy resolution of 15.9% and a coincidence timing resolution of 5.2 ns FWHM.
- Sensitivity-was simulated using a point source with back to back 511 KeV photons was estimated to be 10.7 %, 6.6 %, 4.4 % and 3.2 % at detector separation of 5, 10, 15 and 20 cm respectively.

A large FOV PEM scanner-Duke University and Thomas Jefferson Laboratory

The system consists of two opposing panels, each consisting of 15 x 20 cm of detector elements of size 3.03 mm x 3.03 mm x 10 mm LGSO (lutetium gadolinium oxyorthosilicate) crystals coupled to a 6 x 8 array of position sensitive PMTs (R7600-00-C8, Hamamatsu). The breast is imaged under compression in this system (typical detector separation of 6-9 cm) [78], and this is achieved using the paddles of a X-ray mammography onto which this device is integrated. For X-ray only imaging, the PEM system is removed from the gantry.

Performance Characteristics:

- Spatial Resolution-Measured using a 0.5 mm inner diameter needle filled with ^{18}F, the spatial resolution ranges from 4.8 mm FWHM to 5.8 mm FWHM depending upon the acceptance angle range for the lines of response (5 degrees to 50 degrees).
- Sensitivity-Measured using 1.0 uCi (in 1 ml) sample in a 3 ml plastic syringe placed in the center of the field of view ranged from 100 counts/s/uCi for a 20 degree acceptance angle to 650 counts/s/uCi for a 45 degree acceptance angle.
- Lesion detectability-Spheres of diameter 3.0 to 8.5 mm (in 0.5 mm increments) were positioned in a cylinder containing F18 flouride such that the lesion to background ratio is 8:1. Lesions bigger than 3.0 mm spheres could be visualized following iterative image reconstruction.

The Positron Emission Mammography/Tomography (PEM/PET) System

The PEM/PET system is a dedicated breast imaging system with biopsy capability built into the design [79]. The patient is positioned in the prone position. The system consists of 4 planar detector heads, with 2 opposing heads functioning in coincidence with each other.

Each detector head, consists of a 96 x 72 array of 2 x 2 x 15mm^3 LYSO crystals, with an active field of view of 15 x 20 cm^2. Each crystal element is polished on all sides, and has a pitch of 2.1 mm with its neighboring crystal element(s). A 0.1 mm thick reflector material is part of the 2.1 mm pitch. One face of the crystal array surface is coupled to a 3 x 4 array of flat panel position sensitive photomultiplier tubes (PS-PMT, Hamamatsu H8500) via a 4 mm thick acrylic glass window. The acrylic glass serves the function of spreading the light from the scintillators onto the PS-PMT, which in turn results in better signal detection in areas where the crystal surface does not overlap with the PMTs. The opposing face of the crystal array is coated with white reflecting material and carbon fiber reinforced composite material. The detector modules are enclosed in aluminum housing with minimal allowable gaps and dead-space for maximal breast FOV coverage. The PSPMTs are read out by a resistive readout circuit that allows anode multiplexing. Each detector head has its own dedicated 64 channel ADC (FPGA based) which assigns positions, energy and timing information to each incoming event, which is further transmitted via USB to a dedicated computer for that detector module. Coincidence processing is done online, wherein data is acquired if two events are detected between the opposing planar heads within 3.5 ns. Each event in this case is indicated by the sum of all anode signals of a detector head. The detector heads are mounted on a gantry that allows x, y, z translation as well as rotation of the opposing detector heads. This allows data sampling in multiple angles.

Image reconstruction is carried using the OSEM (Ordered Subset Expectation Maximization) algorithm.

Performance Measurements:

- Spatial Resolution-was measured by scanning a capillary tube filled with [^{18}F]-FDG, and was imaged at various positions and angular acceptances. Spatial resolution achieved at the center was 2.01 +/- 0.09 mm (radial), 2.04 +/- 0.08 mm (tangential) and 1.84 +/- 0.07 mm (axial).
- Sensitivity-was measured using a point source and was 6.88 %, 5.73 %, 3.76 % and 1.75 % for a full acceptance angle, 30 deg, 20 deg and 10 deg maximum acceptance respectively.
- Lesion Detectability-was measured using two 3 mm diameter spheres with 5 mm center to center spacing and positioned in a uniform cylinder of diameter 8 cm. The spheres were filled with a lesion to background ratio of 8:1 and 10:1 and reconstructed images demonstrate good lesion detectability.

3.6 PET/MRI Instrumentation

The following section gives an overview of PET-MRI instrumentation development, starting from initial tests and proposal by Hammer and colleagues in the year 1990, small animal

PET-MRI systems to the more recent human PET-MRI scanners.

3.6.1 Initial PET Technology and Small Animal Systems

PET using PMTs and optical fiber technology

Some of the earliest commercially available PET scanners were primarily based on a detector design, where the scintillating crystals were coupled to a photomultiplier tube (PMT), e.g. the CTI/Siemens Animal Tomograph model 713 [80]. The first reported attempt to combine PET and MRI was reported by Hammer and colleagues [81]. The use of a PMT in close coupling with scintillator, is an approach that does not allow its integration into an MRI machine due to the fact that PMTs are sensitive to the magnetic fields and do not function normally in its presence. At the same time, metallic components of the PMTs distorts the magnetic field of the MRI which cause artifacts and distortion in the MRI image. Hence, the most logical first attempt was to modify the scintillator-PMT combination so that the PMT is positioned far away enough such that it can operate normally and at the same time have minimal effect on the MR field. This was accomplished by introducing light guides between the scintillator and PMT. The schematic arrangement for this configuration is shown in Figure 3.5 wherein the light guides transmit the optical photons from the scintillator to the PMT which is positioned outside the magnet bore. Such a design was implemented using two NaI (T1) scintillation crystals placed inside a 5T magnet[82]. The NaI crystals were coupled to the PMTs using a cylindrical Lucite rod. Experimental results from this system showed an improvement in the resolution of a Ge-68 source from 2.19 mm FWHM outside the bore to 1.64 mm FWHM inside the bore, as a result of reduction in the positron range inside the magnet environment.

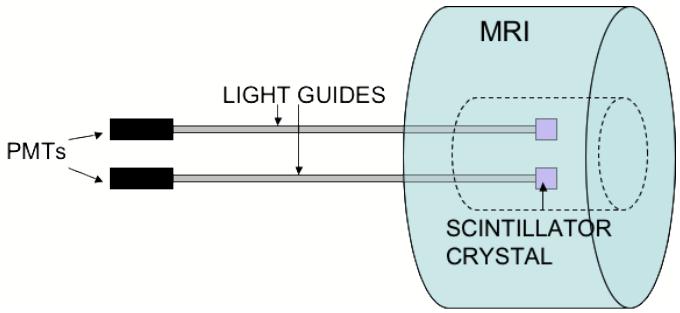

Figure 3.5: Schematic arrangement proposed for initial PET-MRI configurations

A more complete system was then developed by Cherry and colleagues, which used a modified version of the design of the Concord microPET high resolution small animal imaging system. The microPET system uses individual crystal elements stacked together and coupled on a one-to-one basis with an individual pixel of a multi-channel photomultiplier tube through optical fibers. This architecture was modified for the MRI environment by

using long optical fibers and placing the PMT in a low magnetic field area outside the magnet. This is the design of the McPET (MRI Compatible PET) system [83] system, which produced the first simultaneous PET-MRI images. The McPET I system consisted of a ring of 48 2 x 2 x 10 mm^3 Lutetium Oxyorthosilicate (LSO) crystals of inner diameter 38 mm, connected via 2 mm diameter, 4 m long double clad optical fibers to three multi channel PMTs (MC-PMT). Each 2 x 2 mm LSO crystal face was coupled to each individual element of the MC-PMT. The MC-PMTs were positioned at 3 m from the center of the MRIs bore, where the magnetic field was 0.1 mT and the MC-PMTs could be operated properly(B ¡10 mT). A steel box was used for shielding the PMTs and their associated readout electronics from ambient light, magnetic fields, and radio frequencies.

A second prototype system, called McPET II was fabricated consisting of seventy two 2 x 2 x 5mm^3 LSO crystals arranged in a ring with an inner diameter of 54 mm. McPET II stopping efficiency is 34 %, in comparison to 14 % in the McPET I. McPET II was used to acquire the first simultaneous PET P-31 NMR spectroscopy of an isolated perfused rat heart in the 9.4 T Bruker NMR spectrometer [84], the so called PANDA acquisition system (PET and NMR dual acquisition). The use of fiber optic cables to position MRI sensitive equipment far from the magnet, and avoiding ferromagnetic material in the PET system, minimizes interference between the two imaging modalities, and no significant artifacts due to such interferences [85].

PET using solid-state electronics

The major drawbacks of photomultiplier tubes that prevented their use in an MRI were overcome with the development of semiconductor detector technology. The APD working principle is based on the conversion of photon energy into free charge carriers in the semiconductor bulk, and their multiplication via the process of impact ionization. The basic element of the structure is the p-n junction. When a reverse bias is applied, a volume close to the junction is depleted of free charge carriers. The charge carriers created in the depleted region drift in the electric field towards the corresponding electrodes, and while traversing this region, acquire enough energy to produce electron-hole pairs by impact ionization. The newly created charge carriers may create new ones and thus an avalanche of electrons and holes move through the detector, which is detected through an external circuit.

APDs have good timing and energy resolution, and magnetic field insensitivity, and are hence suitable for PET-MRI. Another attractive feature of the APDs is their small size and ruggedness that allow coupling with very small crystals and high packing fraction not possible with traditional PMT based designs.

Rapid advances in semiconductor technology in the 1980s resulted in several improvements, such as higher gain and gain uniformity, due to better doping and growth techniques of the Si wafer, and higher quantum efficiency in the blue range of the spectrum (surpassing PMT quantum efficiencies) thereby making them suitable for coupling with scintillators. APDs also have an advantage over PMTs in not requiring high bias voltages to operate. Neverthe-

less, APDs are prone to high noise due to factors such as shot noise from internal and surface currents, capacitance noise from downstream electronics such preamplifiers, and statistical noise due to the avalanche processes. Hence, low noise front-end electronics are required to minimize the noise and assure a good signal to noise ratio from such detectors. Another disadvantage is that APD gains are sensitive to temperature and, consequently, temperature monitoring or control is needed when operating APD based devices [86, 87]
The first APD based small animal PET scanner was The Sherbrooke Avalanche Photodiode Positron Tomograph [86, 88, 89]. This scanner consisted of 256 BGO-APD detector modules [90] and a transaxial FOV of 118 mm and an axial FOV of 10.5 mm. With the introduction of Ce-doped LSO crystals, LSO-APD detector modules were assembled which were able to achieve nanosecond timing resolution [91, 92]. Detector configurations with one to one coupling between LSO and APD pixels were explored, along with position encoding APDs [93–95]. Various detector configurations were explored, such as the one to one coupling of LSO crystal arrays to a matching APD array (Figure 3.6) as well as position encoding using APDs [93–95]. The LSO-APD combination was tested in the MRI by Pichler and colleagues.

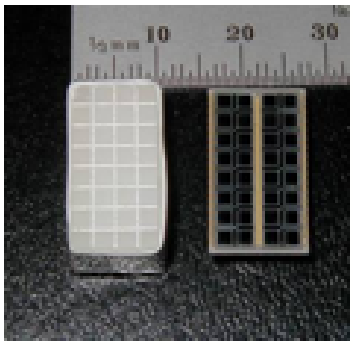

Figure 3.6: A 4 x 8 LSO crystal array next to a 4 x 8 array of non-magnetic APDs (Hamamatsu S8550)

Studies were conducted in the 9.4 T magnet [96] by coupling an LSO crystal to a 3 mm active diameter APD via a silicone rubber disc. The detector was positioned in the magnet bore, and was enclosed by an aluminum box in order to shield from MRI interference. The output of the preamplifiers connected to the APD output are then fed to a preamplifier shaper outside the magnet via an 11 m long coaxial cable. The studies demonstrated the stable performance of the LSO-APD detector module inside the 9.4 T, with no dependence in gain and energy resolution of APD on the magnetic field along with no dependence on the orientation of the APD with the magnetic field lines, hence establishing the feasibility of such an approach.

APD based small animal PET - MRI scanners have been successfully developed. Pichler and colleagues developed a system, wherein the PET system fits inside 7 T BioSpec 70/30

Ultra Shielded Refrigerated MR, or a 7 T ClinScan MR system (Bruker BioSpin MRI) [97]. The PET system is positioned between the RF coil and gradient system of the MRI scanners and has a transaxial FOV of 36 mm. The PET system consists of a ring of 10 detectors, wherein each detector module consists of a 12 x 12 array of individual 1.5 x 1.5 x 4.5 mm LSO crystal coupled via 3 mm long light guides to a 3 x 3 APD array. The PET detector modules are shielded using copper (10 micrometer thick). The output of the APD is routed to electronics modules that are placed in a low magnetic field area (less than 0.0005T).

The RatCAP based small animal PET-MRI scanner is also functional, and employs the use of APD-LSO modules [98, 99]. The detector module consists of a 4 x 8 array of 2.2 x 2.2 x 5mm^3 LSO crystals, directly coupled to a 4 x 8 APD array. Each of these detector modules is mounted on a socket on a rigid flex circuit (Figure 3.7) and twelve such detector modules make up the PET ring. The PET ring, which is identical in its architecture to the RatCAP system, is placed in the center of the magnet, while the TSPM is placed at the edge of the MRI bore. The TSPM is shielded using an aluminum box. Cables transferring signals from the PET ring to the TSPM are also shielded using segmented copper. Power supply units are positioned outside the MRI room, along with the data acquisition computer which transmits and receives events from the TSPM through optical fibers.

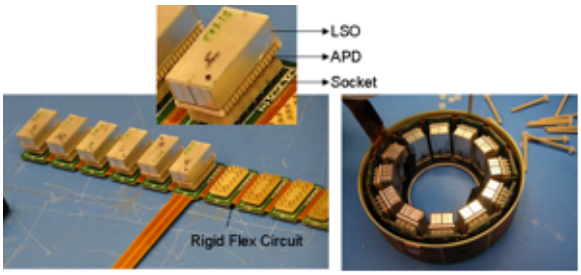

Figure 3.7: Left: A rigid flex circuit partially populated with LSO-APD detector modules. Right: A rolled up rigid flex circuit showing the PET architecture.

The PET system (Figure 3.8) is housed in a Delrin (polyoxymethylene) plastic case, along with a custom designed RF coil that can operate in a quadrature mode positioned inside it. The PET assembly with the RF coil has a transaxial FOV of 31 mm.

Newer detector technologies such as Position Sensitive Avalanche Photodiodes (PSAPD) and Silicon Photomultipliers (SiPM) have made it easier to combine PET and MRI imaging modalities. PSAPDs are basically a layer of detector material with output terminals positioned such that the relative intensity of the avalanche signal at these contacts serves to determine the exact location of the photon interaction, a principle similar to that underlying Anger logic positioning. PSAPDs, therefore, have less contact terminals than traditional pixellated APDs while approaching the same performance level. Hence, use of PSAPDs can reduce cost and complexity of a system, which is especially important in the

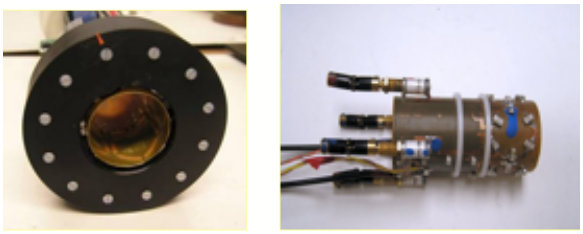

Figure 3.8: Left: PET ring housed inside Delrin can with RF coil placed inside it. Right: The custom MR coil used inside the PET ring.

MRI environment where space restrictions can be critical. Several groups are working with PSAPDs [100] [101] [102] [103] and also using them for the development of simultaneous PET-MRI scanners [100]. The PET-MRI scanner developed by Catana and colleagues uses a detector module wherein an 8 x 8 array of LSO crystal (1.43 x 1.43 x 6 mm^3) is coupled via optical fibers (more than 10 cm long) to a 14 x 14 mm^2 PSAPD. The PET ring consists of 16 such detector modules, and is placed between the RF and gradient coil of the MRI. PSAPD output is fed to a charge sensitive preamplifier (CSP), which is surrounded by concentric copper cylinders for minimizing electromagnetic interference between PET and MRI. The signals from the CSP are transmitted to signal processing electronics placed away from the magnet using non magnetic coaxial cables. PSAPDs are also useful for depth of interaction or DOI encoding [104, 105]. With their fewer electrical contacts and low gamma attenuation properties, DOI measurements are feasible by placing PSAPDs on two opposite faces of the scintillator crystal. Hence high resolution imaging is possible with such a configuration.
SiPM is another novel technology fit for the MRI environment as it combines the high gain, low noise properties of a photomultiplier tube with the magnetic insensitivity of an APD. It also is less temperature dependent than APDs and has low operating voltages and production costs, along with picosecond timing resolution. SiPMs operate above the breakdown point or in the Geiger mode, and hence have high internal gains [106]. They can have a few hundred to a few thousand microcell or micropixel APDs on a common substrate of 1 x 1 mm^2. Studies of SiPMs with scintillator crystals, such as LSO for PET have demonstrated good energy and timing resolution [107]. However, a potential drawback of SiPMs is their low detection efficiency at LSO emission wavelengths.

Modified MRI scanner architectures

Most PET-MRI architectures involve a design wherein the PET scanner design is modified to fit inside the MRI. However, PET-MRI scanners have also been designed wherein the MRI scanner instrumentation was modified to accommodate PET detectors. Two such systems are the MicroPET-MR and the Field cycled MRI-PET system. In the MicroPET-MR system, the architecture of the MicroPET (Focus 120) small animal scanner is combined with an MRI [108]. The design of the system is called the "split magnet" design as the

superconducting magnet of the MRI is split into two halves separated by 80 mm wherein the PET detector modules are positioned. The detector modules consist of a 12 x 12 LSO crystal array coupled to a PMT that is positioned radially outside the bore at a field strength of about of 30 mT. The detector are arranged in a ring structure. The LSO crystals are connected to the PMTs via optical fibers, and the PMTs are further shielded using soft alloy or permalloy material.
The field cycled PET-MRI system consists of two magnets - the polarizing magnet and the readout magnet. The polarizing magnet is a high strength magnet that polarizes the object in the field of view while the readout magnet is a low strength magnet that causes the polarized volume to precess at the Larmor frequency of the readout magnet. The principle behind the operation of this system is that the MRI field is cycled to zero or turned off periodically during the pulse sequence during which PET images can be acquired. Hence, a PET system that employes PMTs can be placed inside the MRI and operated during the MR off periods [109]. Such a design was proposed by Gilbert and colleagues [110]

3.6.2 Human PET/MRI Systems

Siemens Prototype Brain PET/MRI Research Scanner

The PET system consists of detector modules made of a 12 x 12 matrix of LSO crystals of size 2.5 x 2.5 x 20 mm coupled to a 3 x 3 array APDs. Six of these detector modules are arranged axially to form a cassette, and 32 of these cassettes arranged in a ring forms the PET cylinder. The system has a transaxial field of view of 35.5 cm and an axial field of view of 19.2 cm. The scanner has an energy resolution and timing resolution of 22 % FWHM and 5.6 ns FWHM respectively.
Image reconstruction for the system is carried out using Poisson ordered subset expectation maximization three-dimensional algorithm. The system has a resolution of 2.5 mm FWHM at the center and 4.5 mm FWHM at 10 cm off center measured using a line source. It has a sensitivity of 6 % to a point source in the center. Phantom tests show no qualitative difference in the image quality and performance obtained between standalone and simultaneous operations.

Philips Whole Body Sequential PET/MRI Scanner

Philips introduced a hybrid PET-MR whole body system called the Philips Ingenuity TF PET-MRI. This system is not a simultaneous PET/MRI scanner, but allows sequential acquisition of images through a tandem arrangement of the PET and MRI machines as shown in Figure 3.9.

The PET system is based on the Gemini TF PET-CT scanner with modifications made for MRI compatibility. The PET ring has a diameter of 90.3 cm and an axial FOV of 18 cm. Detector modules consists of LYSO crystal array of size 4 x 4 x 22 mm^3 with PMT readout.

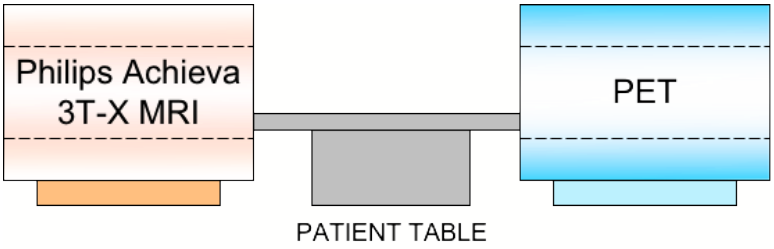

Figure 3.9: The tandem arrangement of PET and MRI machines in the Philips Ingenuity TF PET/MRI system

PMTs are incompatible with the magnetic field introduced by the MRI scanner hence a double layer shielding made of steel and mu-metal is used to deflect the magnetic field lines around the PMT. There are 28 detector modules in the system and each detector module has a 23 x 44 crystal array coupled to 15 PMT arrays. Anger logic is used for event positioning. The MR system used is the Philips Achieva 3T-X MRI . The distance between the PET and MR FOV centers in the tandem arrangement is 4.2 m. All the power and signal lines penetrating the room are filtered and the PET acquisition electronics is placed in a shielded cabinet to minimize electromagnetic interference. The average measured spatial resolution of the PET system at various locations was 4.9 mm FWHM. The scanner has a sensitivity of 7000 cps/MBq to a line source placed at the center. The energy and timing resolution of the PET system following PET recalibration after MRI ramp up was measured to be 11.6 $\pm$0.1 % and 523.3$\pm$11.6 ps respectively [111].

Chapter 4

System Design and Prototype Development

4.1 The RatCAP System

The Rat Conscious Animal PET (RatCAP) system is a small animal PET scanner, that was designed with the purpose of studying brain chemistry of a conscious rat [112]. Hence, a PET scanner that was small in size and compact in its electronics, was built such that it could be mounted on the rat's head and could capture data while the rat moved around in its enclosure and was exposed to various behavioral stimuli. The electronics developed for the RatCAP system form the building blocks of several other PET systems that were subsequently developed including the prototype simultaneous PET-MRI breast scanner. An overview of the architecture of the RatCAP system is summarized below.

4.1.1 The RatCAP scanner

The RatCAP PET ring is a rigid flex circuit, as shown in Figure 4.1a. This rigid flex architecture allows the ring to be formed into a circular shape, and housed in an aluminum can as shown in Figure 4.1b. The weight of the PET electronics and associated components inside the can is 250 g, which, when mounted on the rats head, is offset by a counterbalance weight.

The inner diameter of the PET ring is 38 mm, and the axial length is 18 mm. The main components of the flex circuit are the LSO-APD detector module, sockets that hold the detector modules and an application specific integrated circuit (ASIC) [113] that was developed specifically for RatCAP. Figure 4.2 gives an overview of the architecture of the system. When a gamma interaction occurs in the scintillator crystal, the resulting APD signals are digitized and serialized by the ASIC, and transmitted to the Time Stamp and

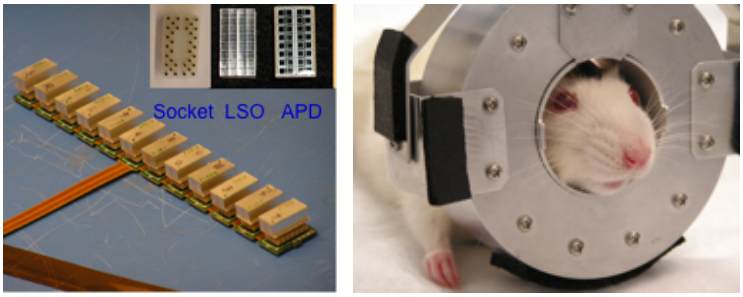

(a) RatCAP rigid flex (b) RatCAP PET scanner

Figure 4.1: The RatCAP system

Signal Processing Module (TSPM) [114], wherein each event is time stamped and formed into a 64-bit word that gets written to a computer hard drive by means of a single fiber optic cable and a custom PCI card. Data is written in the list mode format.

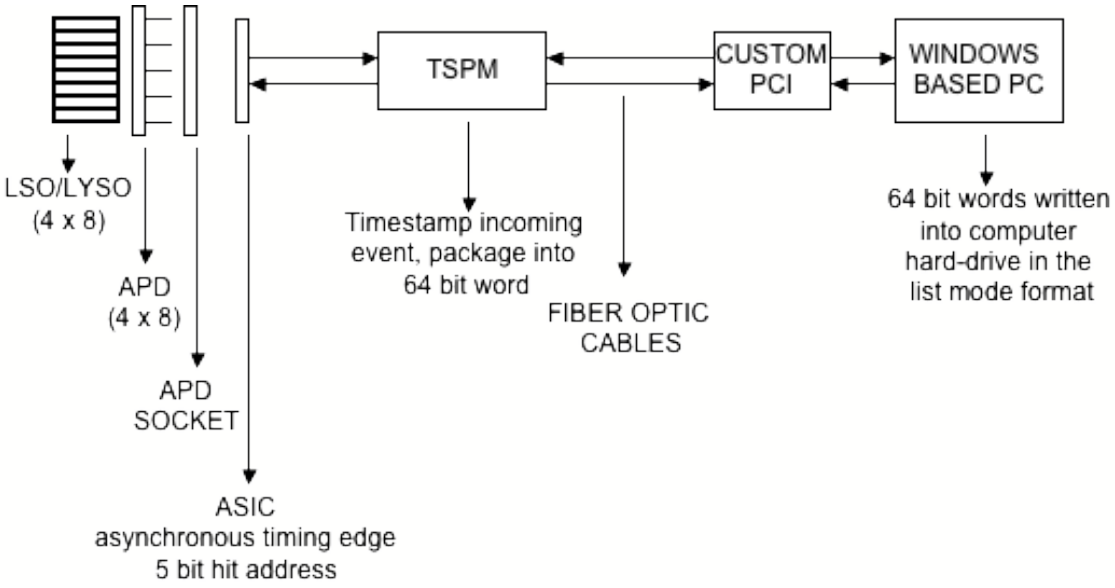

Figure 4.2: Architecture of the RatCAP PET system

Animal studies using RatCAP

The RatCAP has been used successfully in imaging conscious rats and studying neurochemistry such as receptor occupancy and more importantly in correlating neurochemistry and behavior [3], a feat made possible only by virtue of the unique RatCAP design that allows

the animal to remain awake and mobile. Some representative images of the receptor occupancy studies (in this case, the dopamine D2 receptor) are shown in Figure 4.3.

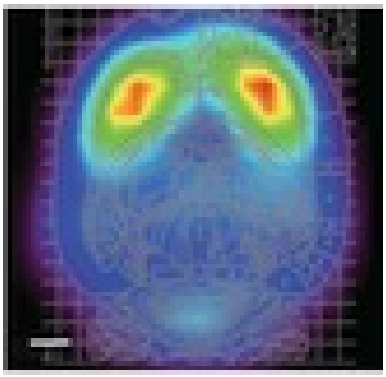

Figure 4.3: RatCAP awake animal rat brain image, from [3]

The constraints posed by the "awake and mobile animal" requirement of the RatCAP system has resulted in a system design that is compact and robust, and lends itself to new PET architectures and applications. The RatCAP, modified by simply substituting its magnetic components, i.e. the APDs and sockets, by non-magnetic ones, has been used successfully in acquiring simultaneous PET-MRI images in the 9.4 T Bruker small animal MRI. With appropriate animal holding and monitoring mechanisms, simultaneous PET-MRI images of a mouse heart and a rat brain have been successfully acquired [115].
The RatCAP flex circuits and readout electronics form the core components of the breast imaging scanner as well. An overview of its two main components, the ASIC and the TSPM are described below.

4.1.2 The RatCAP Front End Electronics - ASIC

An Application Specific Integrated Circuit (ASIC) [113] was developed specifically for the RatCAP system. The mixed signal ASIC is physically located on the rigid flex circuit and there is one ASIC per detector block. Hence, a single flex has 12 ASICs, wherein each ASIC receives its input from its respective APD. The input stage of the ASIC consists of a charge sensitive preamplifier (CSP), followed by a pole zero network with programmable gains (32 steps, or a maximum gain factor of 2.7), a bipolar Gaussian shaper, a zero crossing discriminator, an energy threshold discriminator and finally a 32:5 priority encoder and serializer which minimizes the number of lines and interconnects in the RatCAP system. The ASIC employs Low Voltage Differential Signaling (LVDS) technology, which gives it good noise immunity. A 100 MHz system clock and the 1088 serial programming interface bits are daisy chained between the 12 ASICs using LVDS. The ASIC has a power dissipation

of 117 mW.
The output of the ASIC consists of an asynchronous leading edge, followed by a clock cycle, a stop bit, and a synchronous 5-bit channel address of the event location. The asynchronous leading edge provides the timing information. The 32 zero crossing discriminators' (ZCDs, one per channel) outputs, are connected to a 32 input wired NOR logic gate. Whenever, an event occurs, one of the 32 ZCDs gets triggered, which in turn activates the control signal generator (CSG) which sends a blocking signal to all the 32 channels until the current event is processed and transmitted. This causes a dead time of 70-80 ns in the system during which no new events are detected. In case two events are detected before the CSG can block the channels, the event with the higher channel address is given priority. The output of the bipolar Gaussian shaper is made available for probing on the tether-board for debugging and testing system health. In order to reject events that are Compton scattered, programmable energy discriminators are available. However, only one energy threshold can be applied to all the channels in the system. This can be problematic since there can be considerable spread in the location of the 511 keV photo-peak between channels due to the differences in the inherent gain of the APD channels, due to variations in the light collection efficiency of each APD pixel or due to variations in the properties of the scintillator crystals. The programmable gains help counter this problem, by allowing the user to align the photo-peak location by adjusting the gain levels and in turn the photopeak location of each channel with a precision of factor 2.7 / 32.

4.1.3 Time Stamp and Signal Processing Module (TSPM)

The output of the ASIC consisting of a leading edge signifying time of occurrence of an event, and followed by a 5 bit address of its location in the channel map is then processed by the time stamp and signal processing module (TSPM, Figure 4.4).

The TSPM is responsible for assigning timing information to each of the incoming events, and packaging it into a 64 bit word. Signal processing and time to digital conversion (TDC) is implemented in an FPGA module (Altera Stratix II). The TDC consists of a coarse component, wherein a counter running at the system clock (100 MHz) first assigns timing information with a resolution of 10 ns (1/100 MHz) to the incoming event. This is followed by a fine component, wherein the system clock is shifted to give different phases (within the 10 ns time period) and these phases are then used to latch the leading timing edge thereby giving a resolution finer than 10ns. The delayed phases are implemented by buffering the clock through logic gates. The 64-bit word is then written into a 2k x 64 bit FIFO, implemented in the FPGA, the output of which is serialized and transmitted to a custom PCI card over fiber optic cables via a giga-bit link and optical transmitters and the data gets written to the computer hard drive in the list mode format.

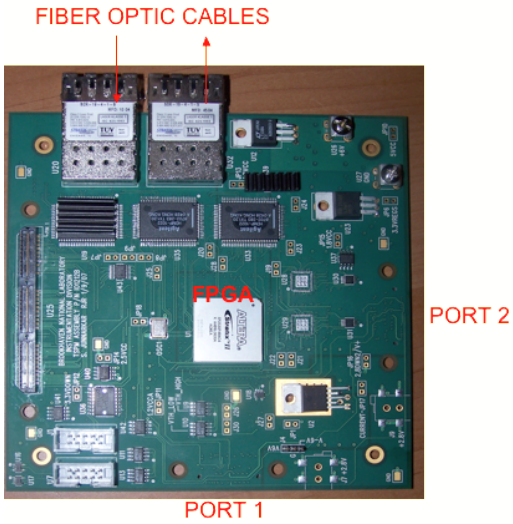

Figure 4.4: Time Stamp and Signal Processing Module - TSPM

4.2 The Aurora Dedicated Breast MRI

The Aurora dedicated breast MRI is a 1.5 T MRI scanner with the radio frequency (RF) coil built into the patient table as shown in Figure 4.5. The patient lies prone onto the RF coil. The scanner employs second order active shimming in the chest area and hence high field homogeneity can be achieved for breast imaging. It has the ability to perform magnetic resonance spectroscopy and has an integrated interventional guidance device for performing biopsies.

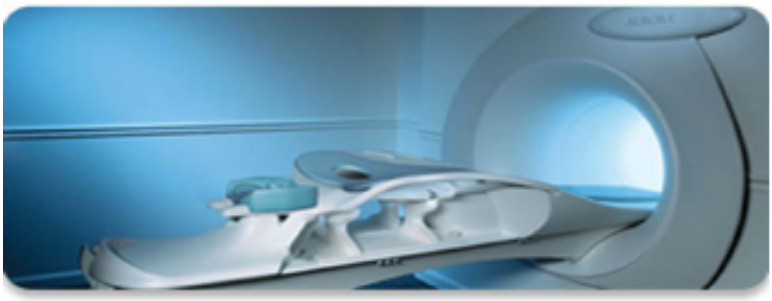

Figure 4.5: The Aurora 1.5T MRI

The Aurora scanner utilizes the RODEO pulse sequence [116], which is a steady state fat suppression sequence that selectively excites water signal. A sine-wave RF excitation pulse at the fat resonance frequency is applied, which is followed by another sine wave that is shifted by 180°. The application of the two out of phase sine wave pulses, causes the fat polarization to be aligned with the main magnetic field (B0), while the water protons are magnetized in

the transverse direction and relax back to the longitudinal field. Signal acquired during this period has signals only from water hence providing efficient fat suppression.

4.3 Simultaneous PET-MRI Breast Scanner

The schematic of the proposed simultaneous, multi-ring PET-MRI breast scanner is shown in Figure 4.8.

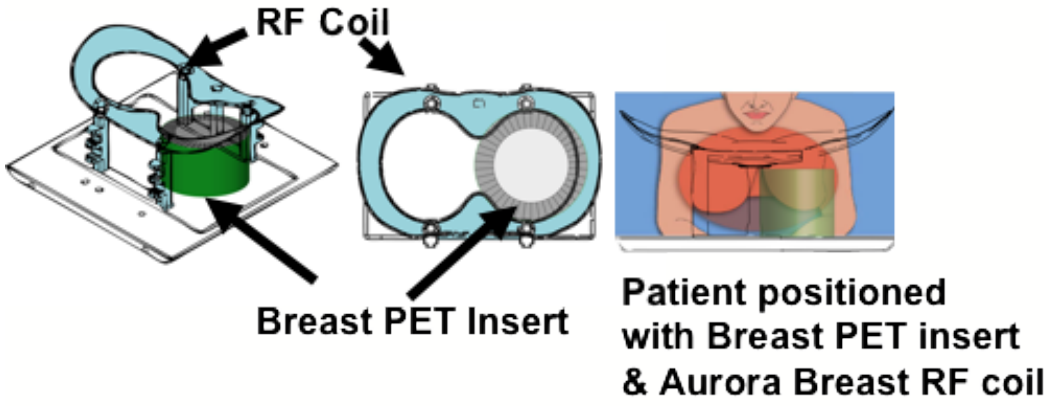

Figure 4.6: Schematic of the proposed simultaneous PET-MRI breast scanner

The proposed breast PET scanner will act as an insert and will be placed inside the RF coil as illustrated in Figure 4.8. The patient lies prone and the breast is surrounded by the PET insert and RF coil, thereby enabling simultaneous PET MRI imaging of the breast. By extrapolating from the available space defined by the geometry of the existing Aurora RF coil, and the components of the PET system developed using RatCAP technology, the ideal scanner configuration is as follows: The proposed breast scanner will be cylindrical in shape with an inner diameter of 145 mm and length of 96 mm. The scanner will consist of 210 detector modules, where each detector module will consist of a 4 x 8 array of 2.2 x 2.2 x 20 mm^3 LSO/LYSO crystals, coupled directly to non-magnetic S8550 APD arrays (Hamamatsu Photonics, Japan), an arrangement similar to the RatCAP. Each module will be read using an ASIC. The proposed system will be made of 42 modular units of detector arrays and each unit will be populated with 5 detectors, giving a total of 210 detectors as shown in Figure 4.7.

Due to the modular nature of the scanner, movement of the individual units with appropriate mechanics will make the scanners FOV variable, hence giving the flexibility of imaging larger breasts. Signals from each module will be sent to the TSPM equivalent where events from 6720 individual crystal pixels are time stamped and written to a computer hard drive.

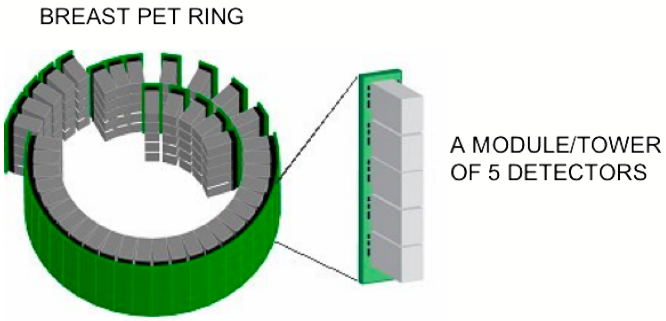

Figure 4.7: Modular components of the proposed breast scanner

4.3.1 Monte-Carlo Simulations Using GATE

Geant 4 Application for Emission Tomography or GATE is a Monte Carlo simulation package that allows accurate geometrical modeling of PET system components as well as physics [117]. Hence, it allows evaluation of novel geometries, and simulations of realistic scan conditions through the use of digital phantoms, for example, the NURBS NCAT phantoms [118] which mimics the human body. The user can also specify their own phantom geometries, assign attenuation coefficients, and activity levels. Hence, GATE is a flexible toolkit that can allow the evaluation of a system under realistic test conditions. Using GATE, some of the performance parameters of the conceptual breast system were first evaluated.

Simulation Parameters - Physics

Several physics parameters can be defined that can determine scanner performance and response. Table 4.1 sums up the parameters set for simulation of the conceptual system. Factors such as the energy resolution, timing resolution, singles dead time, and coincidence dead time were selected based on measurements using the RatCAP system and ASIC characterization studies.

The following performance characteristics of the breast scanner were evaluated and compared with the ECAT EXACT HR+ whole body PET scanner.

- Sensitivity to point source in air.
- Sensitivity to point source in breast - Effect of attenuation using the NCAT torso phantom.
- Estimation of randoms and scatter fraction using NCAT torso phantom with realistic uptake values.

Definition of Geometry: a) The breast scanner geometry as defined in GATE is as shown in Figure 4.8. The scanner has a transaxial FOV of 145.3 mm and an axial FOV of 96.46 mm.

GATE Parameters	**Breast Scanner**	**ECAT EXACT HR+**
	Acquisition and Read-out Parameters	
Energy Resolution	18% @ 511KeV	20% to 30% @ 511 KeV
Timing Resolution	8.5 ns	0 ns
Coincidence Timing Window (2tau)	20 ns	12 ns
Singles Deadtime	80 ns	5000 ns
Coincidence Deadtime	0 ns	500 ns
Low Energy Threshold	350 KeV	350 KeV
High Energy Threshold	750 KeV	750 KeV
	Energy and Range Cuts	
Delta Ray	10 KeV	10KeV
X-Ray	10 KeV	10 KeV
Electron Range	2 mm	2 mm
	Physics Models	
Compton	Low Energy	Low Energy
Photoelectric	Low Energy	Low Energy
Rayleigh	Low Energy	Low Energy

Table 4.1: Table of GATE simulation parameters

In defining the axial spacing between the crystals, realistic constraints (eg- due to the size of the APD and socket) that would be posed by using a design similar to the existing RatCAP flex were accounted for. For estimating the randoms and scatter fraction, a 10 mm thick tungsten shield around the scanner was modeled as shown in Figure 4.8-right. b) The ECAT EXACT HR + scanner geometry has an inner diameter of 82.4 cm and an axial FOV of 15.5 cm. The scanner is comprised of 4 rings of 72 block detectors, where each block is an 8 x 8 array of 4.39 x 4.05 x 30 mm^3 BGO crystals separated by 0.46 mm slits. A tungsten shield was also modeled as shown in Figure 4.9:G6.

Performance Evaluation

- Point Source In Air: A 1 MBq point source (sphere, radius 0.1 mm) was placed in the center of both the scanners. Decays were simulated as back to back gammas and acquisition time was set to 5 seconds. The fraction of true unscattered coincidences originating from the same decay event to total decays was estimated and is shown in Figure 4.10.

- Effect of attenuation medium - point source positioned in the NCAT torso phantom: A NCAT torso phantom was generated using the NCAT software [118]. The torso phantom consists of 128 x 128 x 200 slices of 3.125 mm cubic voxels and includes the major organs. It was not possible to include the NCAT torso with the breast for our simulations because the breast scanner geometry and its positioning around the breast is such that there is bound to be some overlap between the phantom and scanner, which GATE could not handle at the time of simulation. Hence, in order to work around this problem, the NCAT phantom was resliced to a matrix of 128 x 89 x 200 slices and a analytical cylindrical phantom of height 9.646 cm and radius 6.5 cm was positioned to simulate the breast as shown in Figure 4.9: G5. The two scanners were then positioned around this phantom as shown in Figure 4.9: G5, G6. Attenuation properties were set for each organ using the gate materials database. A point source was placed in the cylinder simulating the breast and data was acquired for a simulation period of 5 seconds. Estimated sensitivity of the scanners in the presence of an attenuating medium in its FOV is as shown in Figure 4.11:.

- Estimation of randoms and scatter fraction using NCAT torso phantom: A NCAT torso phantom was simulated as shown in Figure 4.9,G5, G6. Realistic activity concentrations were assigned (Table 4.2) to major organs in order to estimate the contribution of randoms and scatter from background activity in the coincidence data. Randoms were estimated as the ratio of total coincidences not originating from same decay to the total detected coincidences and the scatter fraction was estimated as the ratio of true unscattered coincidences to the total detected coincidences and is shown in Figure 4.12.

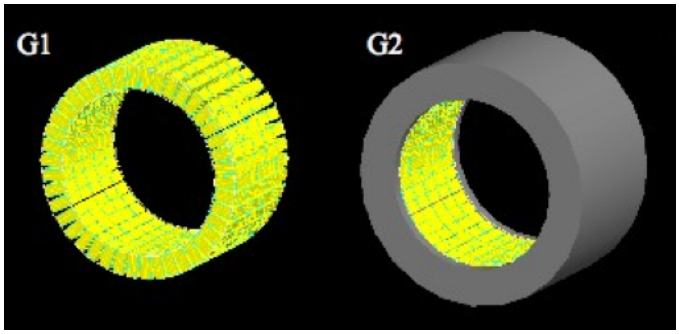

Figure 4.8: Breast scanner geometry in GATE (left), with tungsten shielding(right)

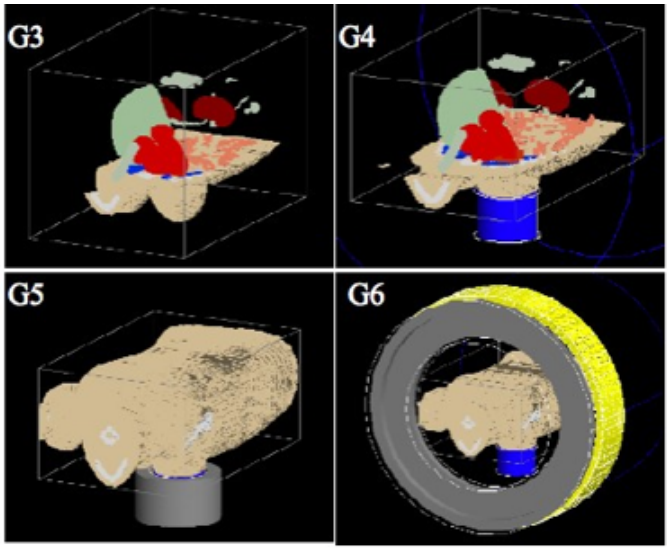

Figure 4.9: NCAT torso phantom simulated in GATE

Organs	Activity (uCi/cc)
Lesion	0.18
Heart	0.13
Liver	0.11
Breast	0.05
Thoracic Cavity/Body	0.05

Table 4.2: Organs and their corresponding activities set for GATE simulation

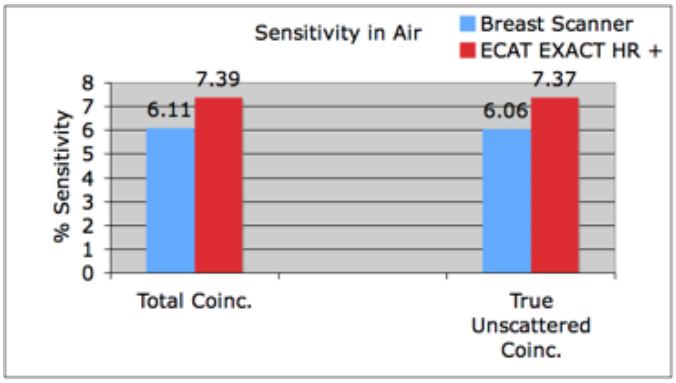

Figure 4.10: Percent Sensitivity of breast scanner and ECAT EXACT HR + scanner to a 1MBq point source in air at the center of scanner FOV

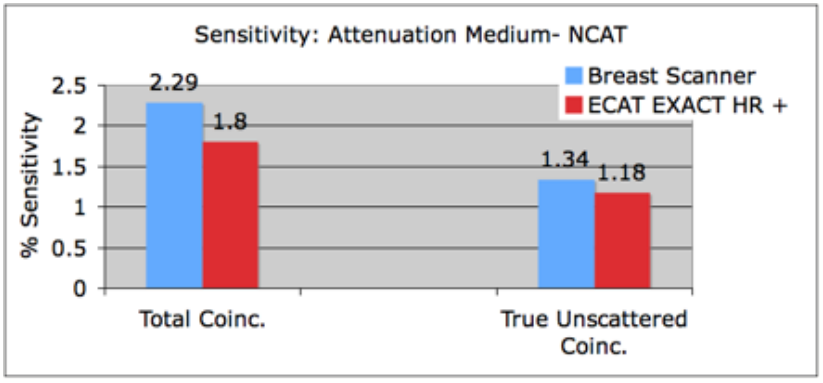

Figure 4.11: Sensitivity to a point source in breast effect of attenuation -NCAT

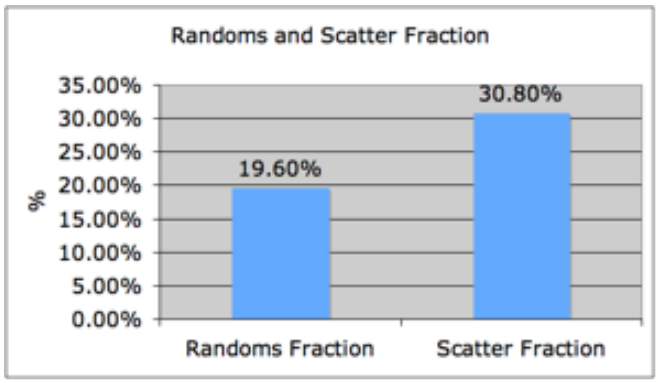

Figure 4.12: Scatter and randoms fraction estimate for breast scanner in the presence of background activity from torso (NCAT)

4.4 Prototype Breast PET System

In order to adapt the RatCAP technology for a breast scanner, the PET system needed an imaging field of view large enough for human studies, or phantoms mimicking realistically sized human breast. In order to realize such a system, two RatCAP flex circuits are connected end to end to give a larger ID, while they are read out by the same TSPM module. Table 4.3 summarizes the various parameters associated with the geometry of the system.

	RatCAP	2 RatCAP Prototype	Full Breast Scaner
Maximum ID	37 mm	116.7 mm	145.3 mm
Axial FOV	18.32 mm	18.32 mm	96.47 mm
Total Crystals	12	24	210
Total LORs	19601	181520	1328360

Table 4.3: Summary of Prototype Breast PET Systems

4.4.1 Prototype-I PET

Prototype-I PET was assembled by connecting two RatCAP rigid flex circuits end to end as shown in Figure 4.13. This strategy allowed usage of as much of the existing electronics as possible.

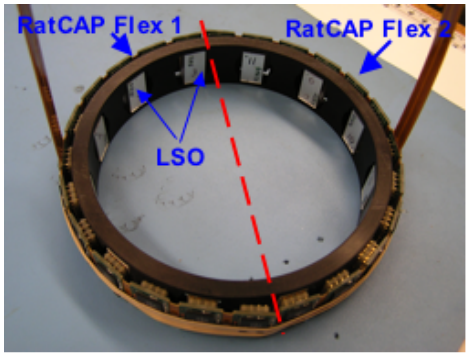

Figure 4.13: 12 detector Prototype I system

The TSPM module was inherently designed to read out signals from two RatCAP flex circuits.The PET ring in this design would have 24 detector modules (12 per flex). The first assembly was done using 12 modules of 4 x 8 array of LSO crystals, where each element has a size of 2.2 x 2.2 x 5 mm^3. The LSO crystals are further coupled to a non magnetic APD arrays (Hamamatsu S8550). The LSO crystals and APD arrays are coupled using optical

glue, and there is one to one coupling between each element, which is advantageous in terms of relative insensitivity to temperature fluctuations in comparison with detector modules that use position sensitive or light sharing approaches. The prototype PET system, when mounted on a stand that supports the tether and tetherboard, does not form a very compact system due to the limited bending radius limitation of the tether (which can result in broken traces). This was addressed in future versions of the flex circuit wherein the tether was eliminated from the design. The assembled system has an inner diameter of 119 mm and an axial height limited by the height of the crystal and APD detector module of 18 mm.

PET evaluation

The first test of the prototype-I system involved acquisition of coincidence events between the two flexes. A "striata" phantom, which consists of two cylinders that are 7 mm apart (center to center), in a larger cylinder of diameter 15 mm as shown in Figure 4.14 was used for this purpose.

Figure 4.14: Striata Phantom

The two cylinders were filled with approximately 0.5 mCi of [^{18}F]-FDG and imaged using the prototype system. The sinogram map in Figure 4.15 shows the activity due to the hot cylinders and the gaps due to the missing 12 alternating blocks. The reconstructed image obtained is shown in Figure 4.16. Image reconstruction was carried out using the MLEM algorithm. The system matrix was estimated using the Monte Carlo simulation package SIMSET [119] for the central field of view of the scanner.

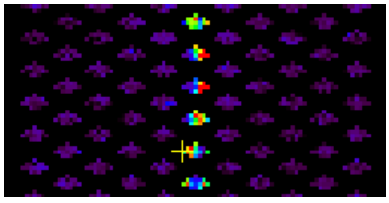

Figure 4.15: Gaps in sinogram due to missing detector blocks

After the acquisition of the PET images, prototype-I was tested inside the Aurora 1.5 T for evaluating the MRI performance with and without PET in its field of view.

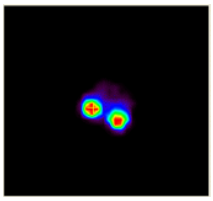

Figure 4.16: Reconstructed image of striata phantom

MRI tests

For evaluation of the MRI performance, the Prototype-I system was transported to the Aurora factory site at North Andover, MA. The system was positioned in the RF coil of the Aurora MRI as shown in Figure 4.17.

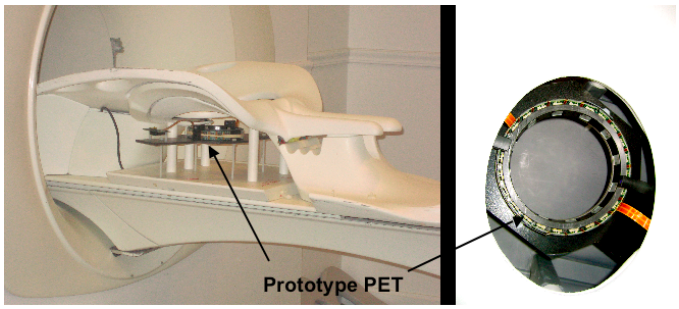

Figure 4.17: Prototype-I PET in the Aurora MRI

For the purposes of image quality evaluation, a mini-deluxe(Data Spectrum Corp., NC, USA) or resolution phantom (shown in Figure 4.18) was used along with a uniform cylindrical phantom. The resolution phantom consists of 5 sections of rods with diameters 4.8 mm, 4.0 mm, 3.2 mm, 2.4 mm, 1.6 mm and 0.8 mm. This phantom was filled with a 1 mM copper sulfate solution. The phantom was first imaged at the 4T Varian MRI at BNL (Figure 4.19), to evaluate its feasibility for MRI tests.

The following MRI parameters were evaluated with and without PET in its FOV-

- Fat suppression - The primary Aurora MRI pulse sequence is the RODEO fat suppression sequence. The breast tissue is mainly composed of fat, which on an MRI image, can obstruct the identification of small lesions, as fat produces a very strong signal. Fat suppression in MRI is realized by suppression of the specific frequency associated with the fat signal. Hence, fat suppression can be compromised due to addition of materials that can disturb field homogeneity. The PET system could potentially cause this due to both the metallic components on it as well as the fact that it has a 100 MHz clock running on it. Hence, in order to evaluate the effect of PET on fat suppression, vegetable shortening, that would mimic fat was used to fill one row of rods in the

Figure 4.18: Mini Deluxe Phantom (Data Spectrum Corporation, [4])

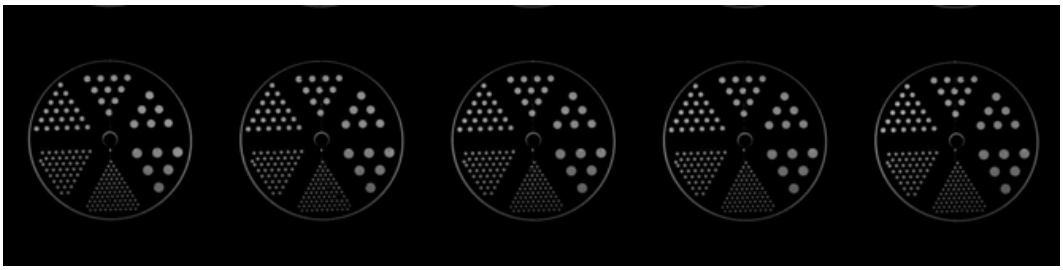

Figure 4.19: Resolution phantom imaged on the 4T Varian MRI

resolution phantom, and this is shown in Figure 4.20. The rods under the white tape were filled with melted vegetable fat and allowed to solidify and sealed off with the tape. The rest of the phantom and rods contain the copper sulfate solution.

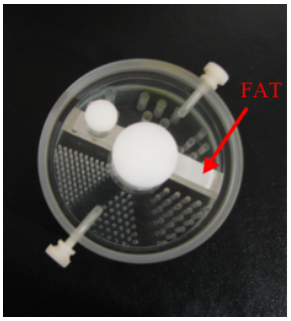

Figure 4.20: Resolution phantom with vegetable shortening to mimic fat

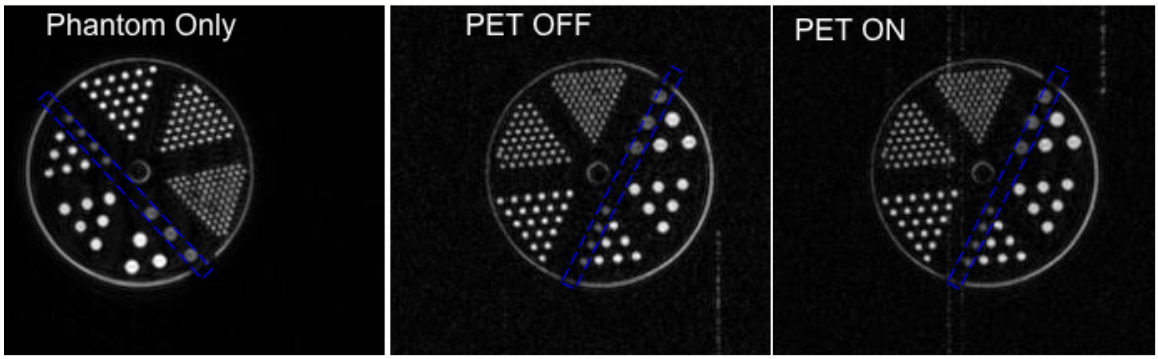

Figure 4.21: Gradient Echo images of resolution phantom with and without PET

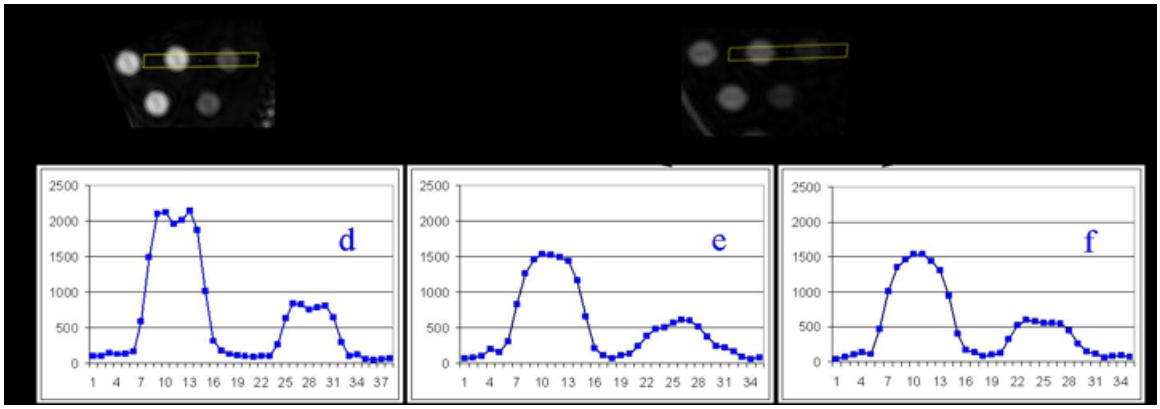

Figure 4.22: Profile plots through rods (CuSO4 and fat) imaged using GE sequence

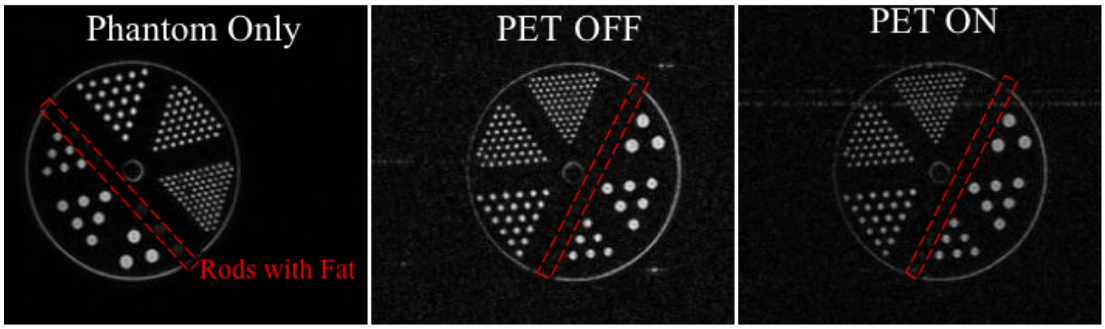

Figure 4.23: RODEO images of resolution phantom with and without PET

The resolution phantom filled with fat and copper sulfate solution was imaged using both the RODEO and gradient echo (GE) pulse sequences. The acquired images with and without PET is shown in Figure 4.21 and 4.23. Profile plots were drawn over a rod filled with copper sulfate and a rod filled with fat and the signal intensity was

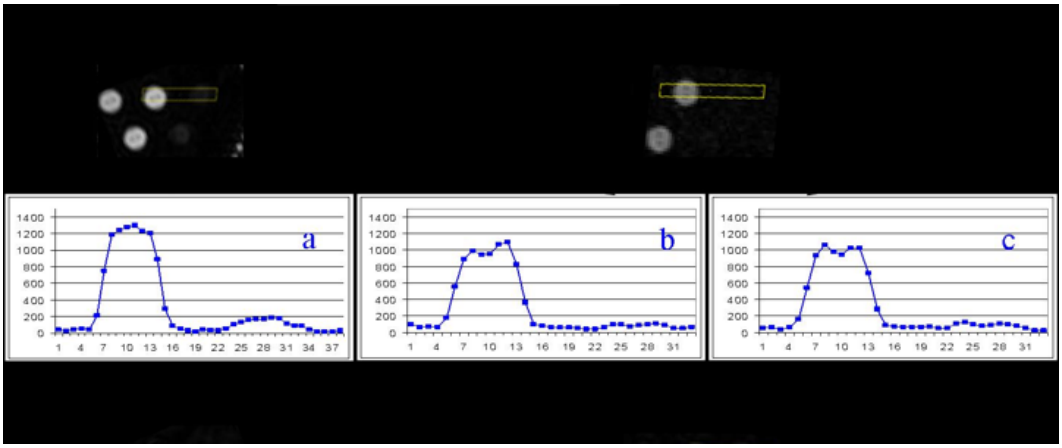

Figure 4.24: Profile plots through rods (CuSO4 and fat) imaged using RODEO showing fat suppression

compared (Figures 4.22 and 4.24. It is observed that there is a slight drop in the signal level with the introduction of the PET system in the MRI field of view, however, the fat signal is still well suppressed in the presence of the PET system.

- Signal to Noise Ratio - SNR was evaluated using a uniform phantom and tested with and without the PET system in its field of view. A ROI was drawn using the ImageJ software [120] in the phantom signal area and one in the background. Mean signal and background ROI values were used to compute the SNR, which was measured to be 198 without PET in the MRI field of view and 114 with PET in the field of view, while acquiring data (low voltage ON, high voltage ON, data acquisition ON). The uniform phantom images are shown in Figure 4.25

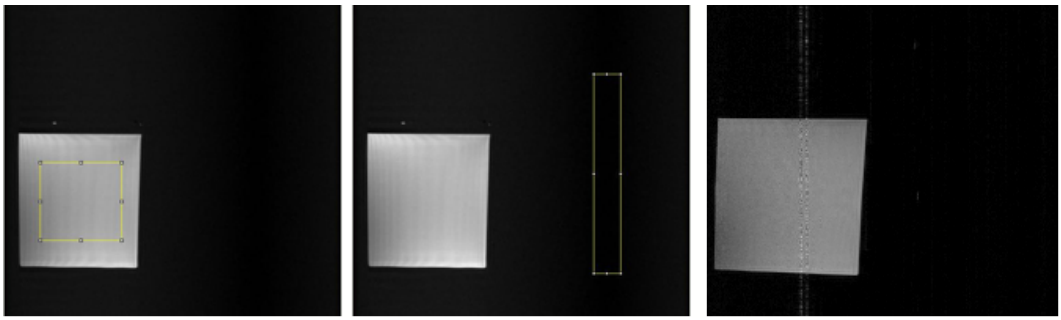

Figure 4.25: Uniform phantom MRI images without (left, center) and with PET (right). ROIs drawn for SNR estimation (signal and background) are also shown in yellow

- Evaluation of MR artifacts: Introduction of artifacts in the MR images due to the PET system being in the MR field of view and operating was evaluated. Two kinds

of artifacts were observed. Once was a slight distortion at the edge of the uniform phantom, and this was attributed to components on the RatCAP flex and possibly due to the presence of magnetic sockets on the flex used for these tests. This is shown in Figure 4.26. Also observed is the RF interference artifact in the form of streaks across the images. This was due to the fact that the RF shield of the MRI room was not maintained for the PET-MR tests since the PET power cables entered the MR room without any filtering, hence bringing in extraneous noise, and the door of the MRI room was left slightly open to allow the cooling hose for the TSPM to enter the room. Hence, there were at least two sources of RF noise during the experimental setup.

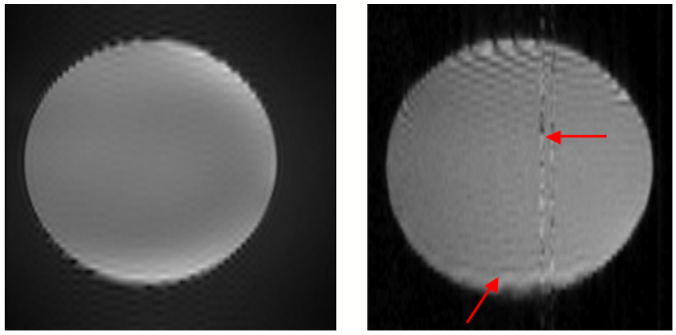

Figure 4.26: Artifacts in the Uniform Phantom due to PET insert

Conclusion

Tests with prototype-I PET showed that coincidence events were achievable using two RatCAP flex circuits. Simultaneous PET-MR tests were conducted using this system to evaluate the artifacts seen in the MRI images. It is observed that there is some distortion in the image due to the magnetic sockets present on the flex circuit used for these tests, as well as RF interference artifacts. Fat suppression worked well in spite of the presence of the PET system. A prototype II system was built following these tests which consists of all non-magnetic sockets. Details of this system are presented next.

4.4.2 Prototype-II PET

Prototype-II PET was populated with 24 detector modules of LYSO and APD arrays as opposed to 12 alternating blocks in Prototype-I and is shown in Figure 4.27. The scanner has a maximum inner diameter (crystal face - face) of 100.8 mm. The axial extent of the system remains the same as Prototype-I at 18 mm.

Image reconstruction and data correction procedures are described next and are based on the procedures established for the RatCAP system [121].

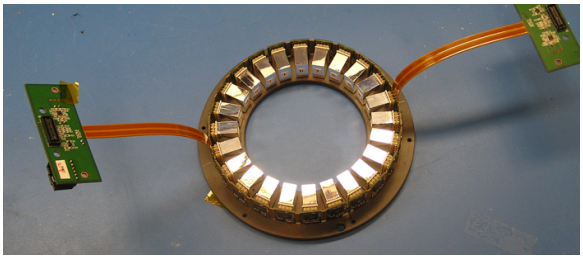

Figure 4.27: 24 detector Prototype - II PET

Energy Resolution

Energy resolution for all individual crystal-APD pairs are determined simultaneously by imaging rod sources (^{68}Ge) and stepping the low level energy discriminator (LLD). The LLD voltage is programmed via an automated LabView interface that steps the voltage from a user specified minimum voltage to a maximum voltage at predefined voltage steps ΔV.

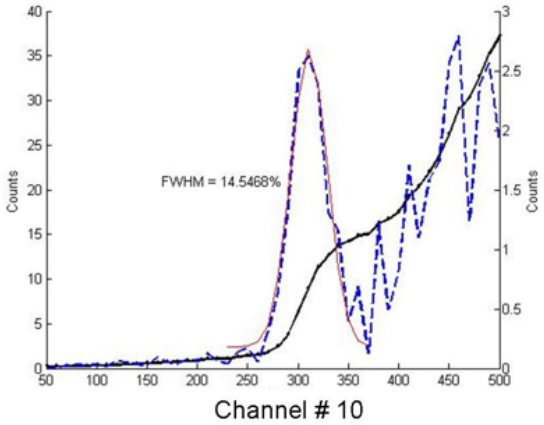

Figure 4.28: Energy resolution

Data is acquired in the list mode format from all the channels for each one of these voltage steps, and the count rate for each channel as a function of threshold voltage is determined. The count rate histogram is obtained for each channel is plotted and a differential spectra is further obtained from this by simply subtracting the count rate from the adjacent voltage step. This differential spectrum gives the energy spectrum of the channel, and an example spectrum is shown in Figure 4.28. The peak seen here is the 511 KeV photopeak along with the Compton scatter peak .

The average energy resolution over all the channels for the 24 detector system was measured to be 12.5 %.

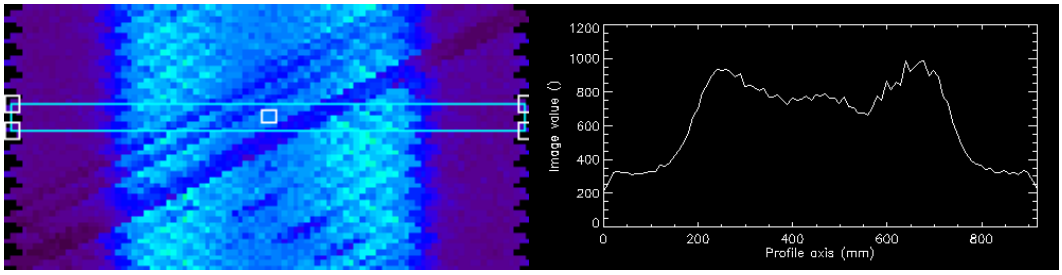

Figure 4.29: Sinogram and profile plot of a normalization scan

Uniformity/Normalization

A uniformity or normalization scan is used to correct differences in efficiencies between different LORs by virtue of either their geometry or due the electronics itself (eg- differences introduced by imperfect gain alignment, variations in intrinsic efficiencies in the crystal-APD pair). This correction is carried out by acquiring data using a uniform cylindrical phantom in the field of view of the PET scanner. The cylinder used for the 24 detector system had an inner diameter of approximately 88 mm and is filled with a uniform distribution of radioactivity. Data is acquired in the list mode format and sorted into sinograms. The sinograms (both prompts and delays) form part of the image reconstruction process using MLEM.
A sinogram of one such normalization scan acquired for the 24 detector prototype system using a uniform distribution of [^{18}F]-FDG is shown in Figure 4.29. One can visually evaluate differences between LOR count rates in response to the same activity concentration. A profile plot through the sinogram is also shown.

Image Reconstruction

Image reconstruction is carried out using the MLEM algorithm. The first step in the process involves the generation of a probability matrix also known as the system matrix. Estimation of the system matrix is done using Monte Carlo simulations using the SIMSET software package. In this simulation, the geometry of the scanner is modeled as accurately as possible. The SIMSET software, until very recently, did not allow modeling of individual detector blocks arranged in a ring form, which is the geometry of the breast scanner. It allowed the modeling of a continuous annulus of scintillating material. Hence, to counter this problem, modifications were made to the software code to discretize this continuous cylinder into pixel arrays of the size and geometry of the LSO crystal array used in the development of the RatCAP and the breast imaging system. This modification had been implemented in the early stages of RatCAP development and was applied without further changes to the breast imaging system. However, even with such discretization, the annulus still forms a continuous layer of attenuating material, although hits are recorded only in the pixellized areas. Once

the scanner geometry is accurately modeled, the FOV of the PET scanner, was divided into a matrix of 103 x 103 voxels transaxially resulting in voxels of size 0.97 x 0.97 x 1.19 mm^3. Axially, there are 19 planes that are 1.19 mm thick. Within each of these voxels, a uniform distribution of ^{11}C source is simulated and the system response to the decays within each voxel is captured in a separate sinogram file. The number of decays within each voxel was set to 20 million. The energy window for the detected photons was in the range of 350 KeV to 700 KeV.

Once the sinogram file from each voxel is obtained, it is zero compressed and concatenated into a single system matrix file. The sinogram data file and the simulated system matrix file then form the input to the MLEM algorithm.

Spatial Resolution

Spatial resolution of the scanner was measured by stepping a ^{22}Na point source (active source diameter 0.25 mm) through the FOV. Images were reconstructed using 100 MLEM iterations, and a profile was drawn through the reconstructed point source. The FWHM was estimated using a Gaussian fit to the profile. This was carried out using the ASIPro software (VM-Concorde Microsystems, Knoxville, TN, USA). The measured spatial resolution plot is shown in figure 4.30. A resolution phantom was also scanned using the prototype system using ^{11}C isotope. It can be observed that 3.2 mm rods are readily distinguishable, whereas simulation studies with enough statistics show that 2.4 mm rods can be distinguished (Figure 4.31).

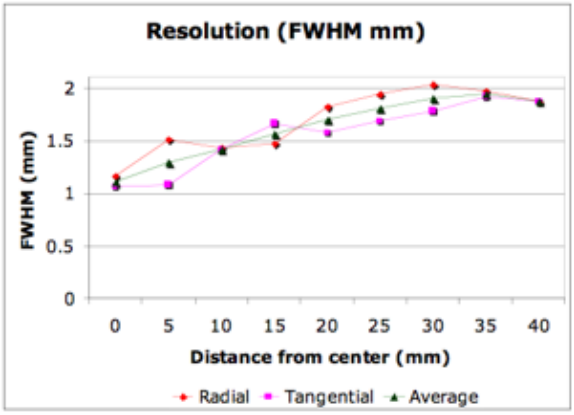

Figure 4.30: Spatial resolution of prototype-II PET

Timing Resolution

Timing resolution was measured using a uniform phantom that fills the scanner field of view. This basically follows the same experimental technique as the normalization scan, and the same dataset can be used for estimating the timing properties of the system. The uniform

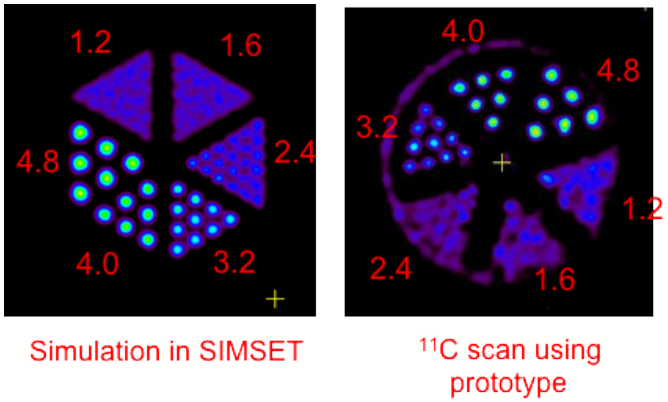

Figure 4.31: Simulated and measured images of the resolution phantom with prototype-II PET

phantom data is sorted into coincidences and a histogram of the distribution of number of events for a range of timing differences is plotted. The timing resolution for the 24 detector system is shown in Figure 4.32. This plot is a histogram of the coincidence timing distribution over a timing window ranging from +50 ns to -50 ns over all the 768 channels of the system. A guassian fit profile is also shown. The FWHM of the spectrum is 32.2 ns.

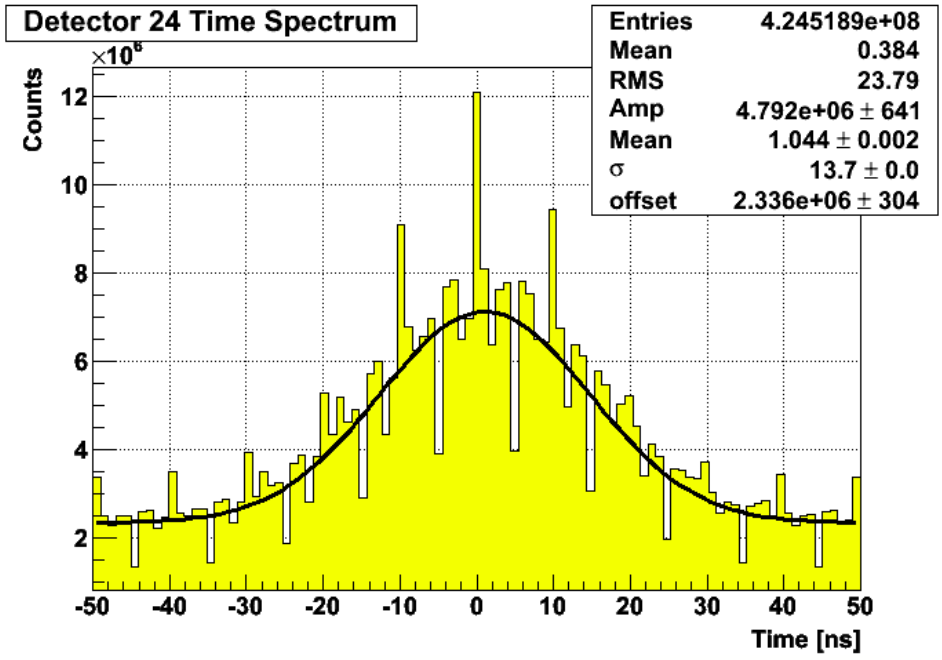

Figure 4.32: Timing resolution of 24 detector PET system

PET-MRI Studies

Prototype-II system was tested in the Aurora 1.5 T scanner for PET-MRI compatibility. The PET ring was positioned in the RF coil with the TSPM board positioned on the table and enclosed in an aluminum box as shown in Figure 4.33. In order to correct some of the

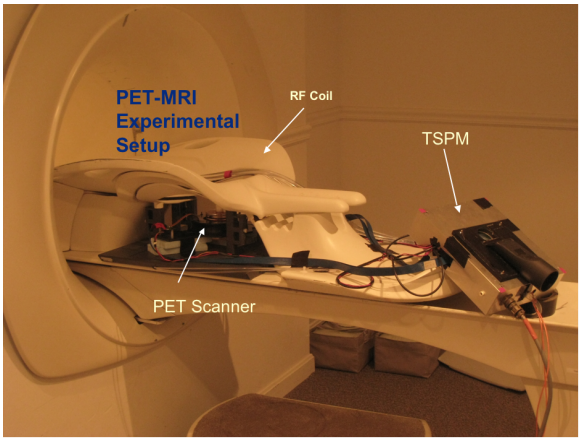

Figure 4.33: PET-MRI experimental setup with prototype-II

problems observed during the testing of the Prototype-I system - namely the noise in the MRI image due to a cooling fan hose and also due to the unfiltered power supplying the PET scanner, two changes were implemented in the design of the PET system. Firstly, cooling was switched from air cooling to liquid cooling. A copper plate with channels for flowing coolant over the area of the plate was built and coupled to the TSPM board through thermal coupling foams (Figure 4.34a). These foams allow for efficient conduction of heat from the TSPM component to the copper plate and also compensates for the difference in heights between the different components. The coolant in this case is the water cooling solution used for the MRI gradients. Water is tapped from the tubes cooling the MRI gradients using a T junction and is routed to the copper plate. This provides efficient cooling for the TSPM board while keeping all cooling equipment contained within the RF shield of the room.

Secondly, the PET power supply lines were filtered using a low pass filter with 80 dB attenuation in the frequency range of 1 Mhz-10 GHz. All the PET power lines i.e. the two high voltage, low voltage and the return line pass through this filter that is mounted next to the penetration panel of the MRI room as shown in Figure 4.34b With the above changes in place, PET-MRI studies were conducted using the 24 detector prototype system and the following PET parameters were evaluated.

- The effect of PET on MRI image quality: A uniform phantom, filled with copper sulfate solution was positioned inside the MRI and imaged with and without the PET ring in its FOV. The signal to noise ratio was estimated by drawing a signal ROI and

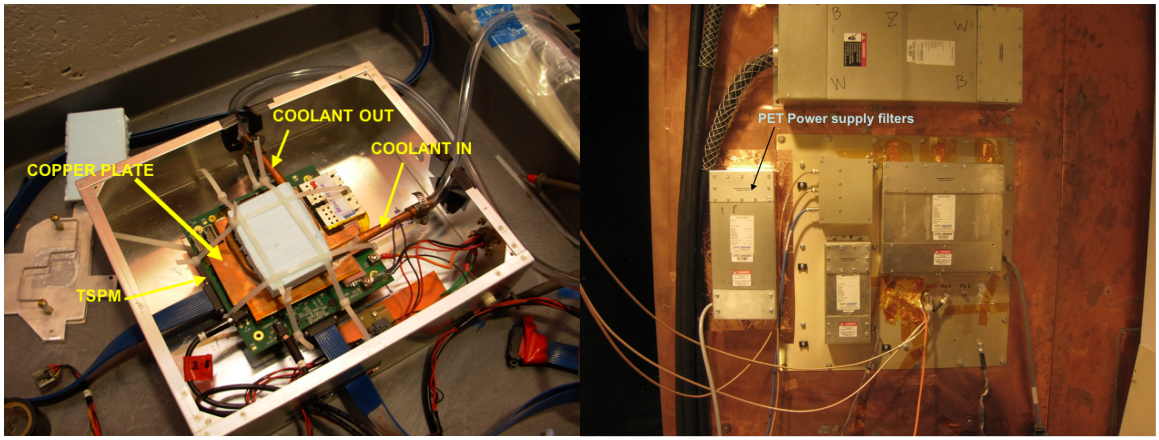

(a) Liquid cooling for the PET TSPM (b) Filter for PET power supply

a noise ROI under the "no PET" condition, and compared with the value under "PET ON" condition. SNR without PET was 453 while with PET ON was 431 as shown in Figure 4.34

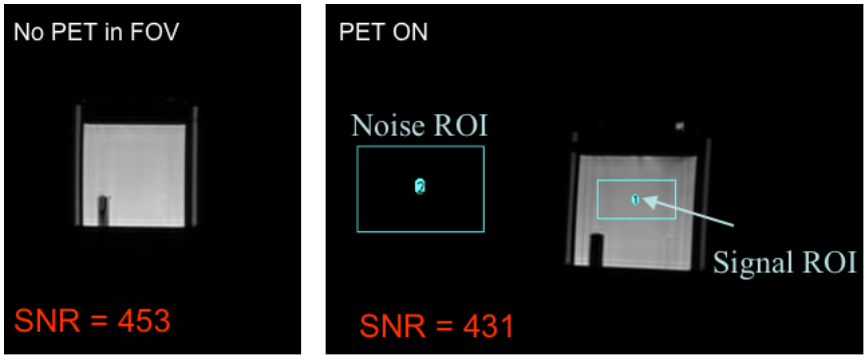

Figure 4.34: MRI SNR with and without PET

- The effect of MRI on PET data: The effect of MRI on PET data was evaluated by plotting the PET count rate as a function of time during MRI RF pulsing. This histogram is shown in Figure 4.35 and shows an increase in the PET count rate following approximately the period of the RF pulsing period of the MR pulse sequence. This observation is consistent with some of the experimental results seen with the small animal MRI compatible RatCAP system.

- Simultaneous PET-MRI Measurements: Simultaneous PET-MRI imaging test was limited to imaging point sources. This was due to the limited license at the Aurora factory site for handling radioactivity, and was restricted to using certified sealed sources.

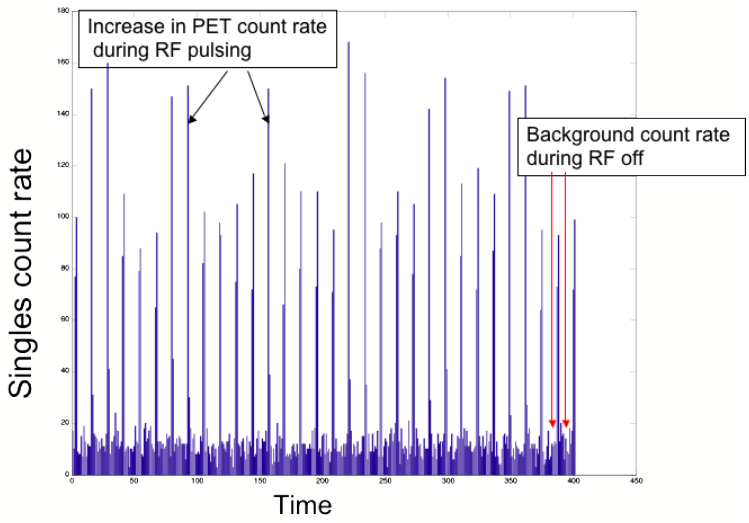

Figure 4.35: Increase in PET count rates during RF pulsing

Hence, two plastic point sources were used for this purpose. One of the source has a disk shape casing with dimensions 1 x 0.25 inches (D x H) while the other point source has a rod shaped casing of size 3 x 3 x 8 mm as shown in Figure 4.36.

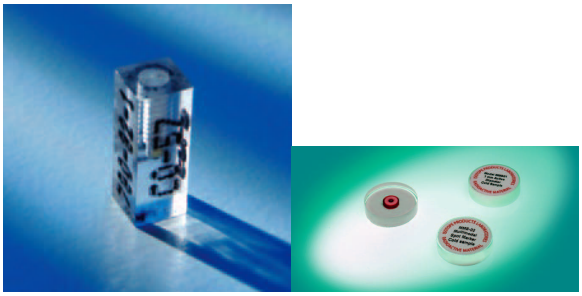

Figure 4.36: Sealed sources used for simultaneous PET-MRI measurements, from [5]

These two point sources were positioned in a cylindrical phantom using a mechanism shown in Figure 4.37 which then is immersed in copper sulfate solution. The mechanical support for holding the two point sources next to each other was made of plastic, and hence in the MRI image, this section would give no signal. The simultaneous PET-MRI images acquired using this phantom is shown in Figure 4.38, which shows the plastic source holder as dark and copper sulfate as bright in the MRI image.

In conclusion, studies with the 24 detector PET system showed that simultaneous PET-MRI imaging is feasible.

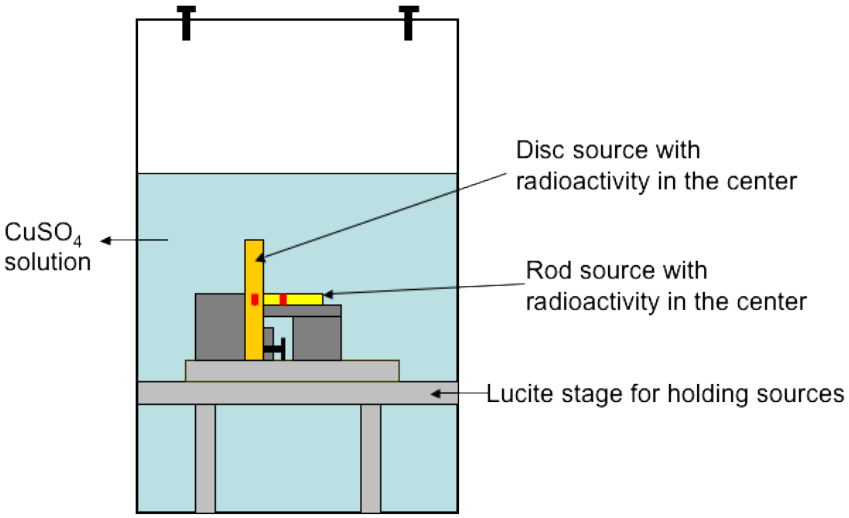

Figure 4.37: Schematic of simultaneous PET-MRI point source phantom

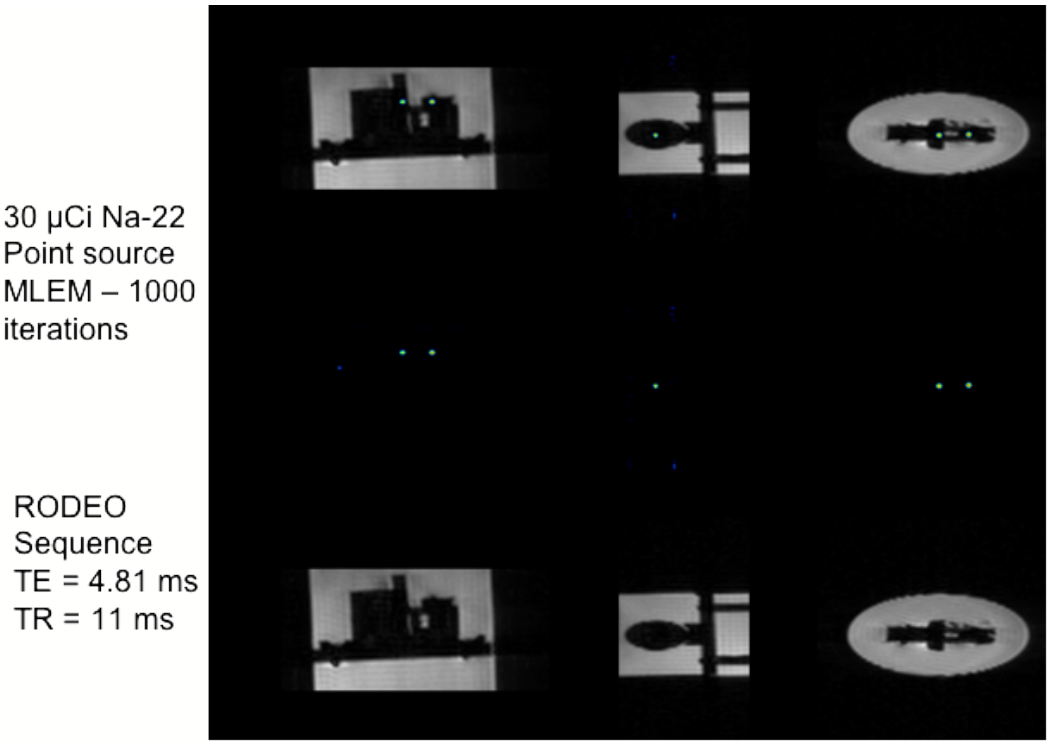

Figure 4.38: Simultaneous PET-MRI images of point sources

4.4.3 Other studies using Prototype-II PET - Wrist Imaging for Estimation of Arterial Input Function

Introduction

The 24 detector prototype PET scanner was also used for continuing studies of determining arterial input function non-invasively. The motivation behind the development of such a device arises from some of the drawbacks of arterial blood sampling which is the current "gold standard" for obtaining such information. The invasive nature of arterial blood sampling poses health risks for both the patient and hospital personnel due to factors such as bloodborne pathogens and radioactive contamination The wrist scanner presented here is an upgrade over a four detector planar system that was developed earlier in the laboratory [122] . The four detectors, each consisting of a 4 x 8 array of $2.2 \times 2.2 \times 15\,mm^3$ LSO crystals coupled to a 4 x 8 APD array (Hamamatsu S8550) are mounted on a flex circuit and positioned around the wrist as shown in Fig. 4.39.

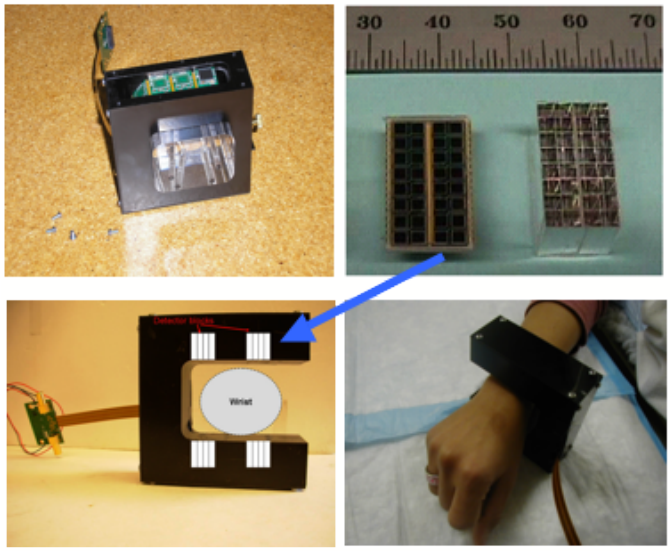

Figure 4.39: 4 detector planar wrist scanner

Studies conducted with this scanner established the proof of principle for obtaining an arterial input function by imaging the wrist. The next step towards this development was a higher sensitivity 3D tomographic scanner, and the design and geometry of the 24 detector PET ring fulfilled this criteria.

As a first step, phantom tests were conducted using the 24 detector PET ring to test if one could reliably observe the change in activity over time in an object that is approximately the size of the human artery. For this purpose, a wrist phantom that was developed earlier was used. The phantom is made of Lucite and has four holes drilled in it that simulates the radial and ulnar artery and vein. An experimental setup where a plastic tube was run

through the holes of this block, and used along with a pump to flow alternating volumes of radioactivity and water through it, was used to test the system. A photograph of this setup is shown in Figure 4.40

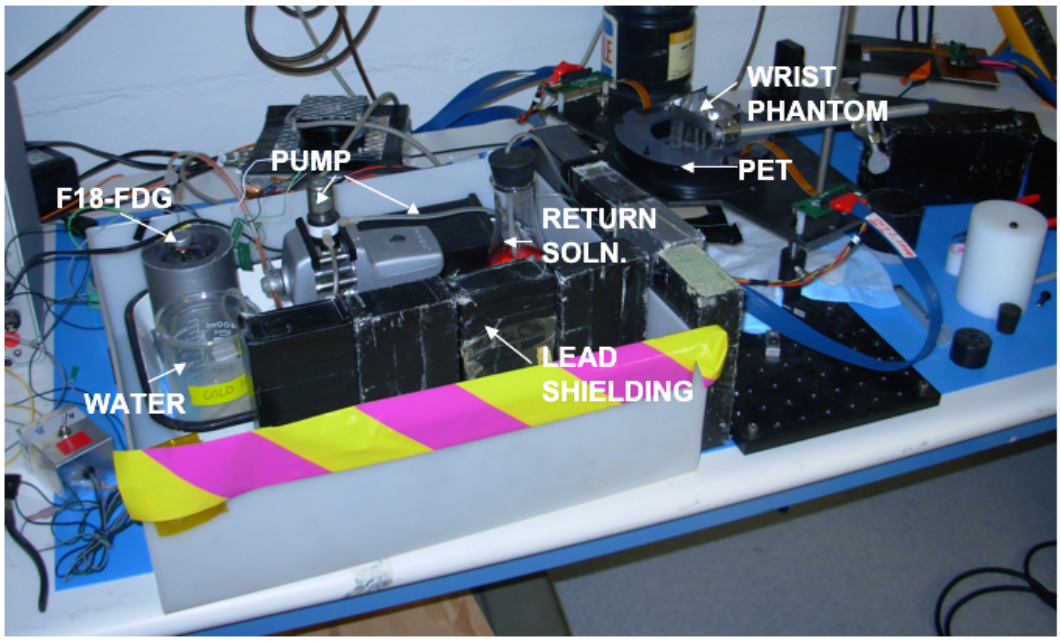

Figure 4.40: Wrist scanner pump experimental setup

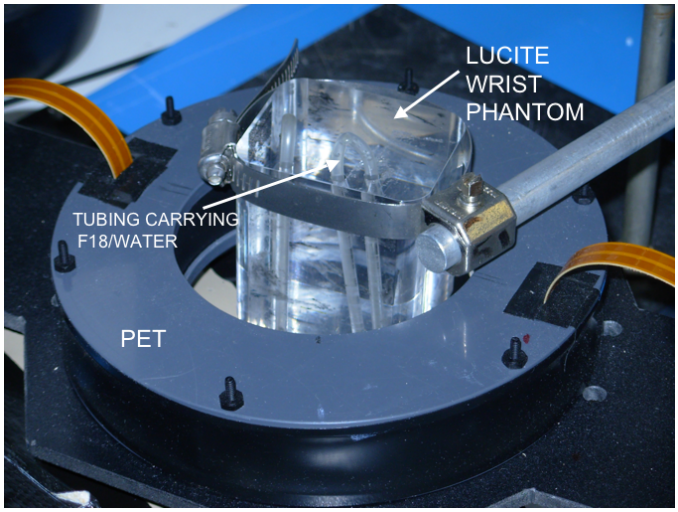

Figure 4.41: Close up view of the wrist phantom inside the wrist scanner

Figure 4.41 shows a close up view of the Lucite phantom and tubes inside the PET scanner. [^{18}F]-FDG and water was pumped through the tube in 10 and 5 minute alternating

segments. Acquired data was binned into sinograms over 30 second time frames and reconstructed using 20 iterations of MLEM. The resulting image is shown in Figure 4.42-left. This image is a sum of all the 30 second time frame images over a period of 35 mins. Regions of interest (ROI) were drawn on this image using ASIpro software and time activity curves were extracted from this, which is shown in Figure 4.42-right. The extracted time activity curve follows the pump switching activity between the [^{18}F]-FDG solution and water.

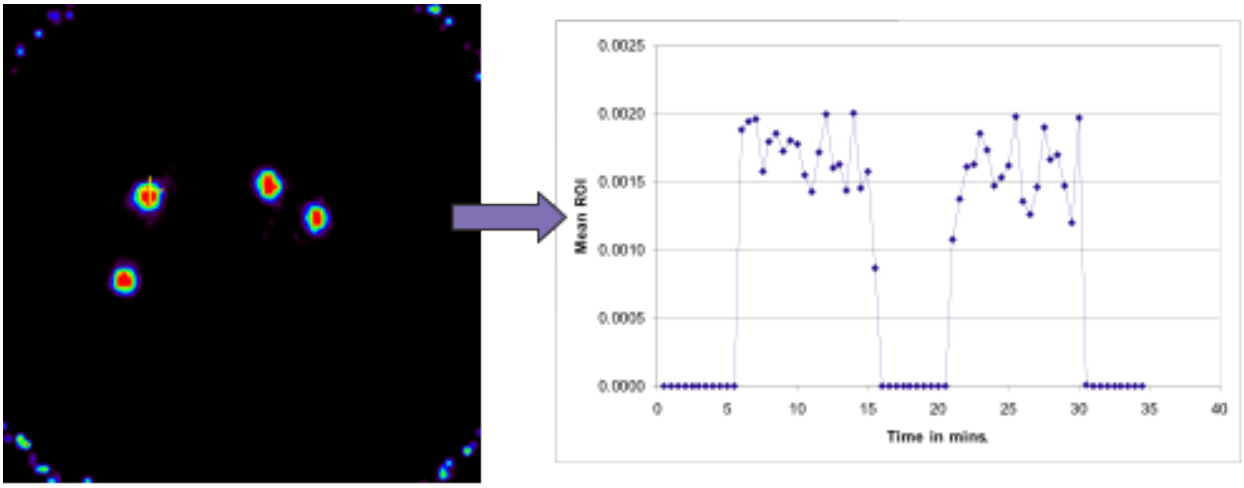

Figure 4.42: Image and time activity curve from wrist pump experiment

Following the phantom experiments, the PET system was set up for conducting human studies. The PET ring was used as a wrist scanner by mounting it vertically and positioning the wrist as shown in Fig. 4.43. The side of the ring facing the body of the subject was shielded from background counts by placing two (1/4)" thick lead sheet(s) as shown in Figure 4.43 .

The overall setup for the acquisition of input function using the wrist scanner for the data presented here is shown in Fig. 4.44. The subject is seated in a chair prior to the PET study and injected with radioactivity. The wrist is positioned in the wrist scanner prior to injection and background data is acquired. Arterialized vein injection is performed on the same arm as the wrist scanner. The other arm is positioned in a hand warmer, and arterial blood samples are acquired using an automated blood sampling device (Ole Dich Instruments, Hvidovre, Denmark), followed by manual extraction of blood by hand. These arterial blood samples serve as the gold standard for comparing wrist PET data.

Data was acquired in list mode format through the injection period upto 20 minutes post injection. Blood sample analysis data served as the gold standard for comparison.

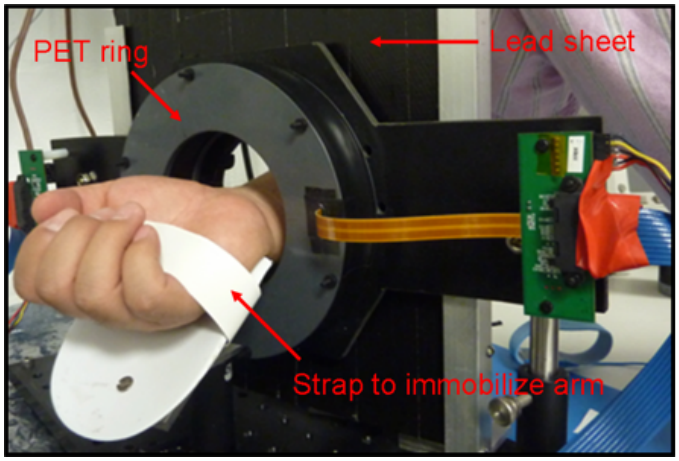

Figure 4.43: Positioning of the wrist in the PET field of view.

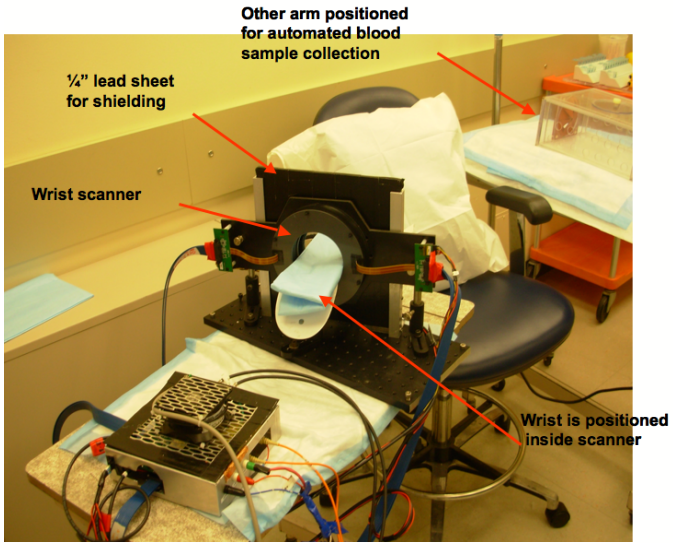

Figure 4.44: Wrist Scanner Setup for Human Studies

Human Subject Results

All subjects were scanned in accordance with the IRB protocol. Two representative studies are shown here.
Subject 1: Injected with 4.6 mCi of [^{18}F]-FDG . Data was binned into 30 second time frames and underwent 50 MLEM iterations.Transaxial and coronal views of the wrist obtained by summing all time frames is shown in Fig. 4.45.

For extracting time series, an ROI was drawn (ASIPro) on an artery as indicated in the figure. A time series of mean ROI value was extracted, decay corrected and plotted against the blood sample data as shown in Fig. 4.46. The PET TAC was scaled to the blood TAC

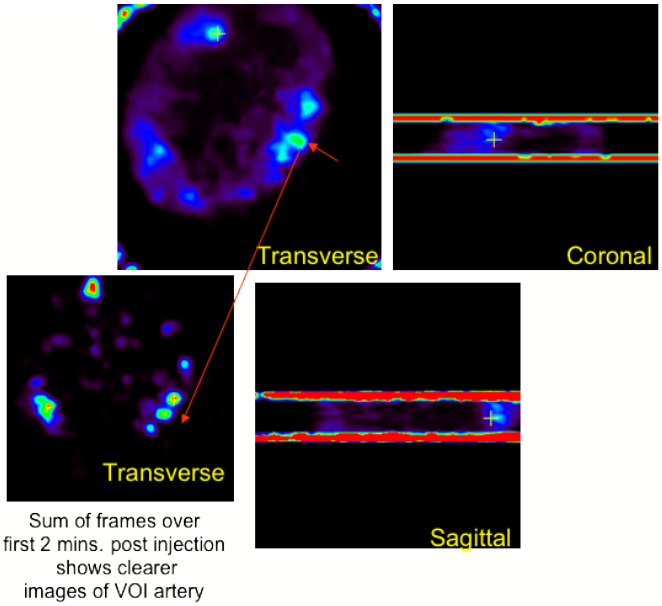

Figure 4.45: Wrist image-patient 1

at 5 minutes post injection. The wrist PET TAC follows the blood sample TAC with good agreement.

Subject 2: Data analysis was carried out following the same procedure described for patient 1. The associated wrist images and TACs are shown in Figures 4.47 and 4.48

In the case of patient 2, the PET TAC does not follow the blood TAC closely. From the studies done with this setup of the PET scanner, it was concluded that there was a need for a scanner with higher sensitivity and for better mechanics to immobilize the arm.

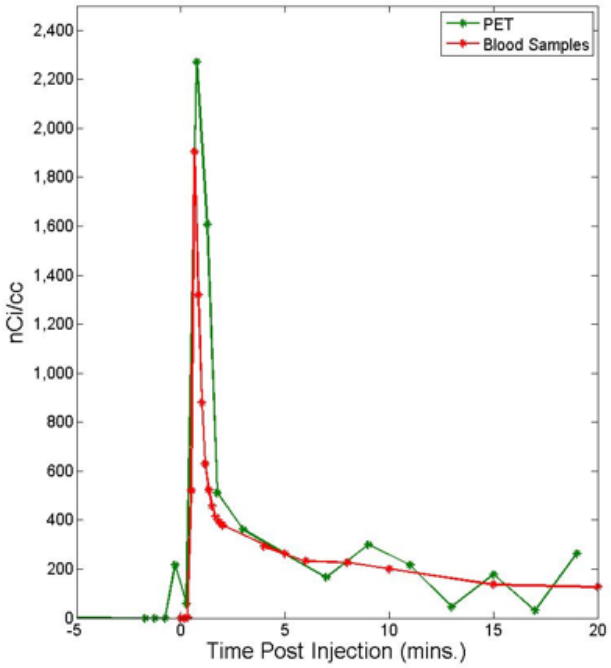

Figure 4.46: Time activity curve(TAC) extracted for patient 1

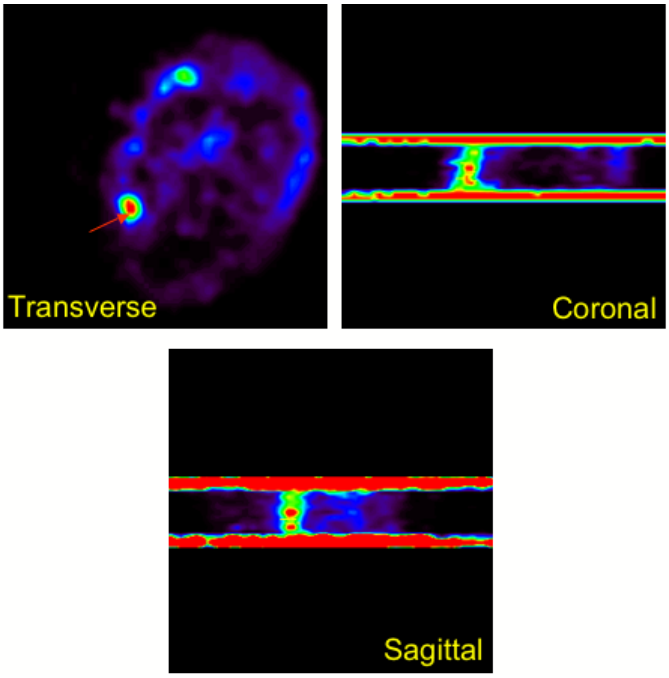

Figure 4.47: Wrist image-patient 2

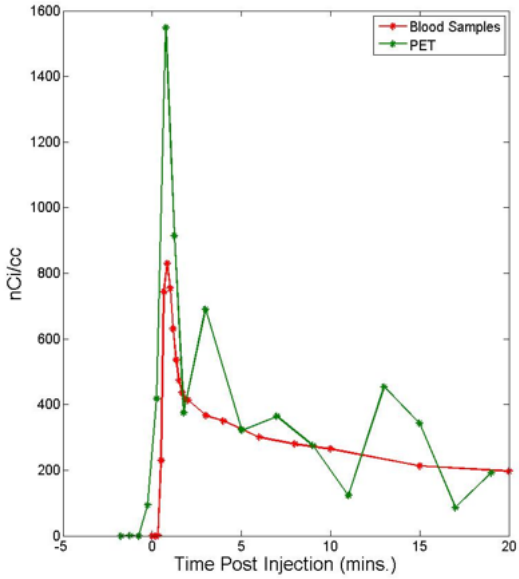

Figure 4.48: TAC extracted for patient 2

In order to address the sensitivity issue, the 15 mm long crystals were replaced with 20 mm long crystals. This system has a radius of 45.39 mm, whereas the axial height remains the same. A system matrix was estimated for this new system using SIMSET, the field of view was divided into a matrix of 91 x 91 voxels transaxially with a size of 0.99 x 0.99 x 1.19 mm^3. Ten million decays were simulated in each voxel. Image reconstruction was carried out using MLEM, as explained previously. Normalization scans were carried using a uniform phantom and energy window alignment done using methods described in previous sections

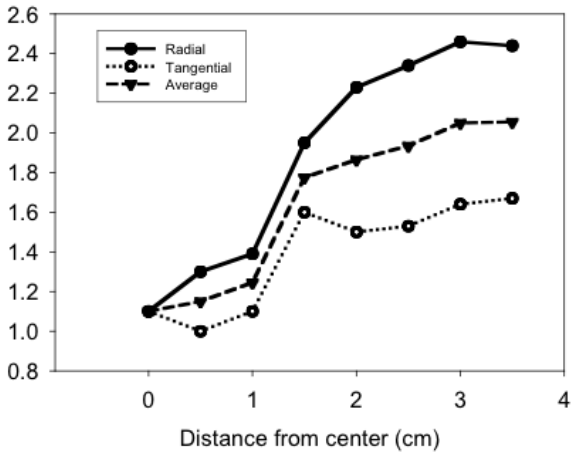

Figure 4.49: Spatial resolution of 20 mm long crystal wrist scanner

The spatial resolution for this system was measured using a ^{22}Na point source by stepping it through the field of view and the resultant FWHM of the reconstructed profile plot is shown in Figure 4.49. A preliminary study of the wrist scanner with a human subject was conducted using this system. For this study, the patient was positioned inside the whole body PET scanner during injection with ^{11}C-Raclopride. The positioning of the PET ring with the patient inside the whole body PET scanner is illustrated using a volunteer shown in Figure 4.50. The injection line was on the same as the wrist PET.

The participating subject was injected 6.3 mCi of ^{11}C-Raclopride. Data was acquired during the course of injection. Blood samples were collected simultaneously from the other arm and served as the gold standard for comparison. The subject was instructed to restrict the motion of their arm in the wrist scanner during this period. Data was binned into 30 second bins for the first 2 minutes post injection, and then into 2 and 5 minute bins over a period of 12 minutes post injection. Each frame was reconstructed using 100 iterations of MLEM, and summed for drawing ROIs. Images acquired is shown in Figure 4.51 and the associated TACs are shown in Figure 4.53. There still appears to be motion during the period of injection and data acquisition and is evident by the TACs shown in Figure 4.52. These TACs show that during the first 2 minutes post injection, there is an increase in

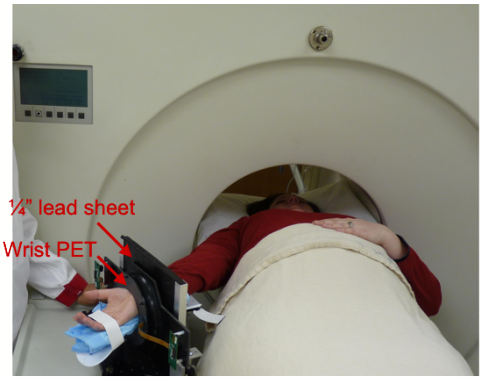

Figure 4.50: Positioning of wrist PET with whole body PET scanner

activity levels, which drops to background abruptly at 2 mins. After the 2 mins, a region close to the pre 2 minute mark, picks up signal levels from background, indicating that this is the same artery/vein and has moved around the 2 minute mark. When the two TACs are summed to each other, the resulting TAC is in good agreement with the blood sample data. The PET data was decay corrected and scaled to the blood TAC (peak).

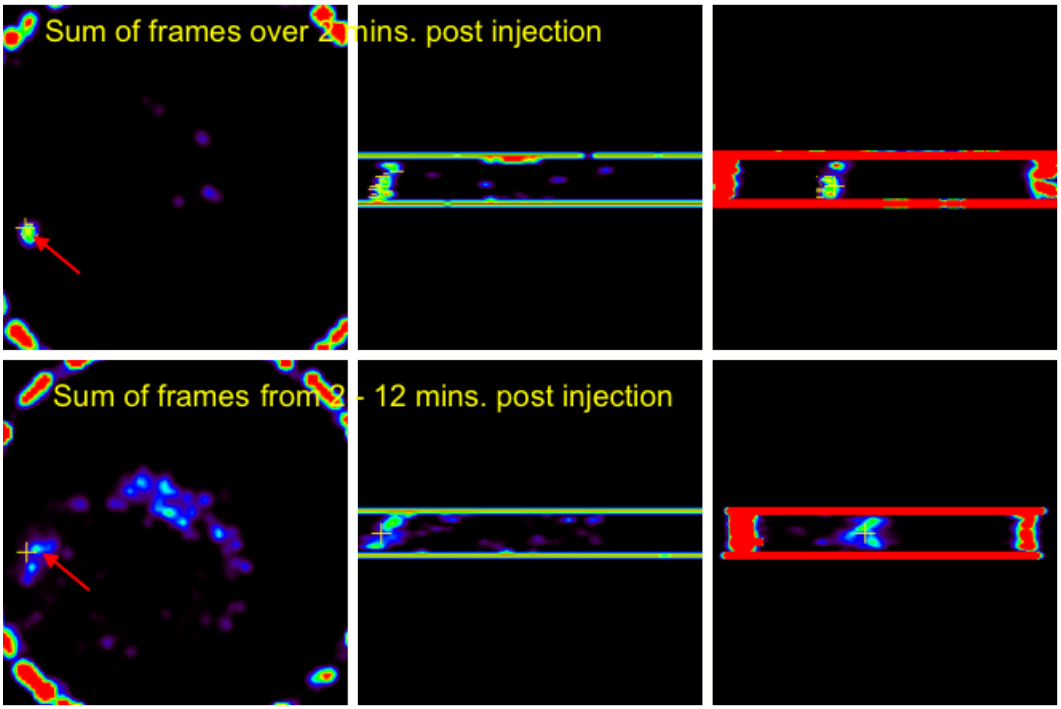

Figure 4.51: Wrist image using ^{11}C-Raclopride injection

Hence, the acquisition of time activity curve with the use of wrist PET scanner, is a

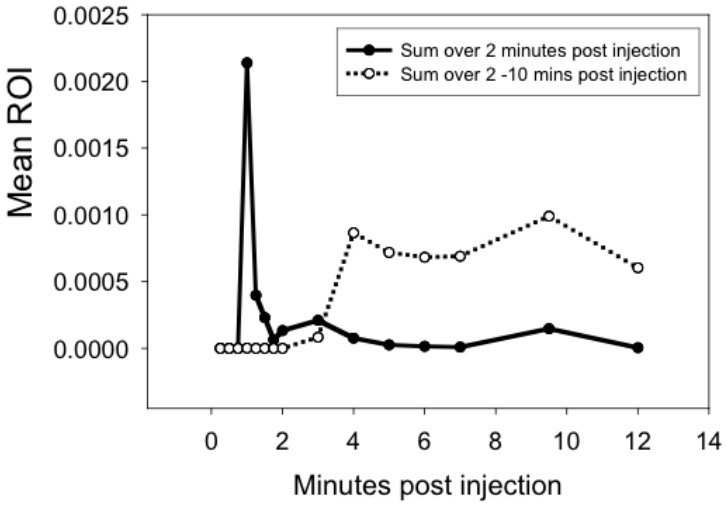

Figure 4.52: Motion during wrist scanner data acquisition-evidence in TAC

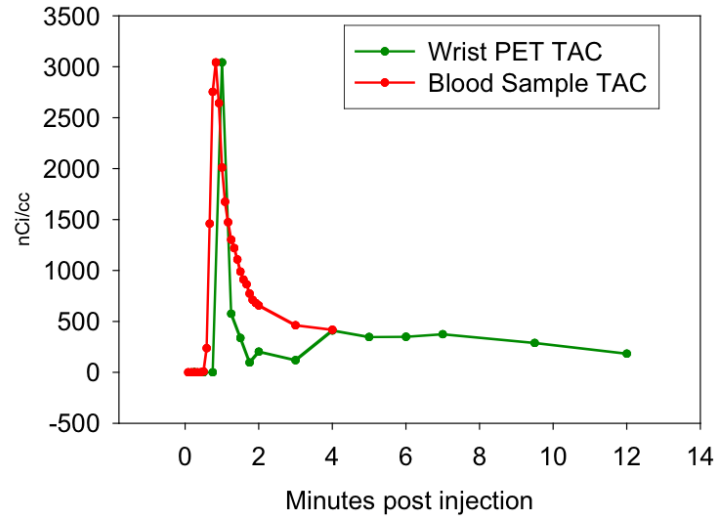

Figure 4.53: Wrist scanner TAC for ^{11}C-Raclopride injection

feasible idea. In terms of practicality, it is quick to position and is comfortable for the patient. However, more ideas for restricting the motion of the arm needs to be explored and implemented. Options using moldable wrist splints have been evaluated on the bench. The use of thermoplastic board such as the one shown in Figure 4.54a can be easily molded to the arm of the patient in a matter of minutes, and can provide very high degree of motion restriction while being comfortable. An example of the wrist splint is shown in Figure 4.54b.

The wrapping of the splint material over the palm also provides support to hold onto once the split itself is mounted on a baseplate.

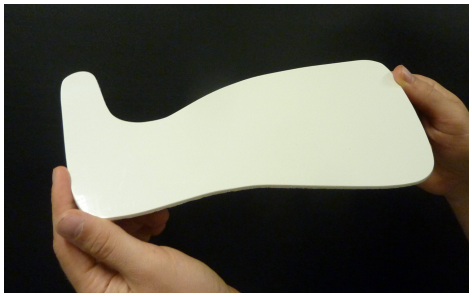

(a) Moldable thermoplastic wrist splint board

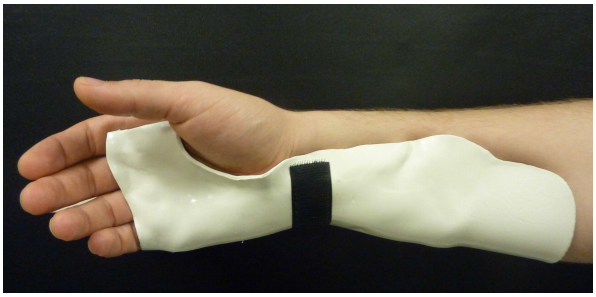

(b) Arm positioned in a molded splint

Figure 4.54: Thermoplastic moldable wrist splints for immobilization

4.4.4 Prototype-III PET

Prototype-III PET was characterized by a few major changes in its design. Firstly, two new flex circuits were used in this assembly. These updated flex circuits, did not have the tether and the tetherboard was connected directly to the rigid flex circuit (Figure 4.56) which had previously restricted the positioning capability of the PET ring in the MRI field of view, as shown in Figure 4.55.

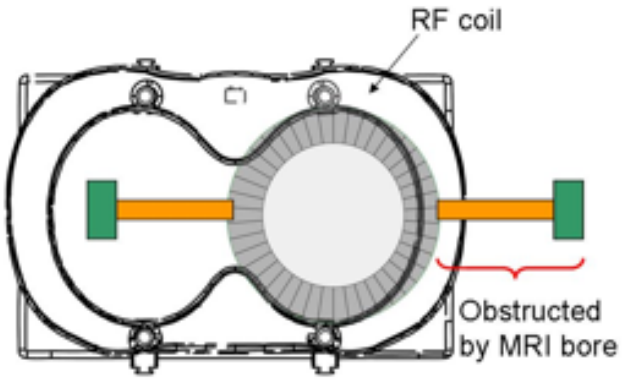

Figure 4.55: Limited positioning capability of PET system with tether

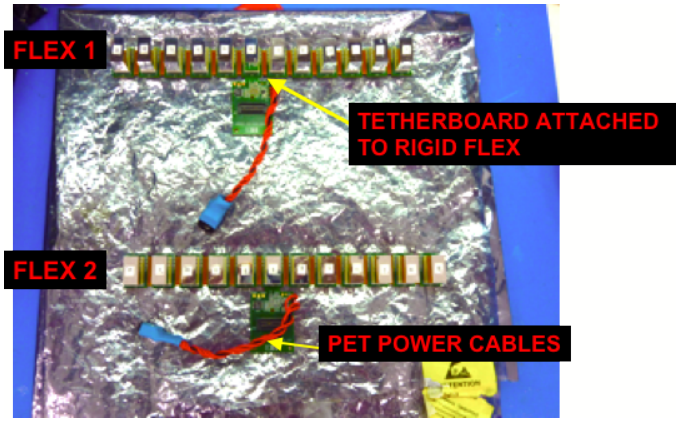

Figure 4.56: Tetherless Flex Circuits

This system was assembled in a ring shape such that it would have 3 missing blocks on each side as shown in Figure 4.57. This gave the ring a maximum inner diameter of 134 mm. This size of the ring was chosen to give a large inner diameter so that human subjects could potentially be imaged.

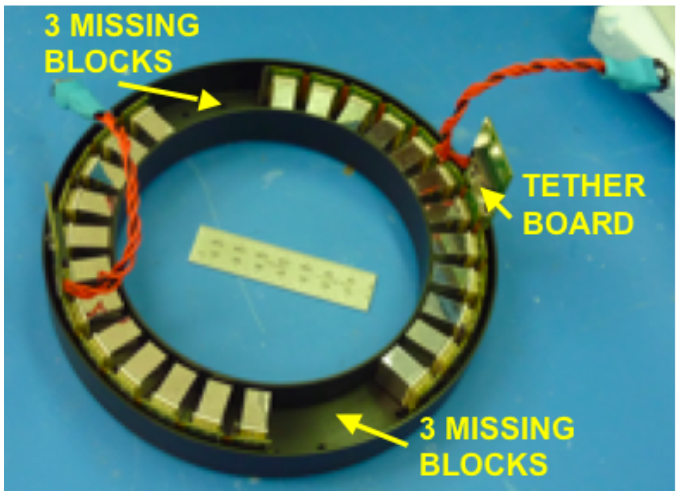

Figure 4.57: Prototype-III PET with 3 missing blocks on each side

A system matrix was estimated for this geometry by dividing the FOV into 137 x 137 voxels in the transaxial plane, with each voxel of size 0.99 x 0.99 x 1.19 mm^3. The system matrix was simulated for one quadrant of the circular FOV and image reconstruction was carried out by applying symmetries in the system. An example of the reconstructed image of a striata phantom is shown in Figure 4.58.

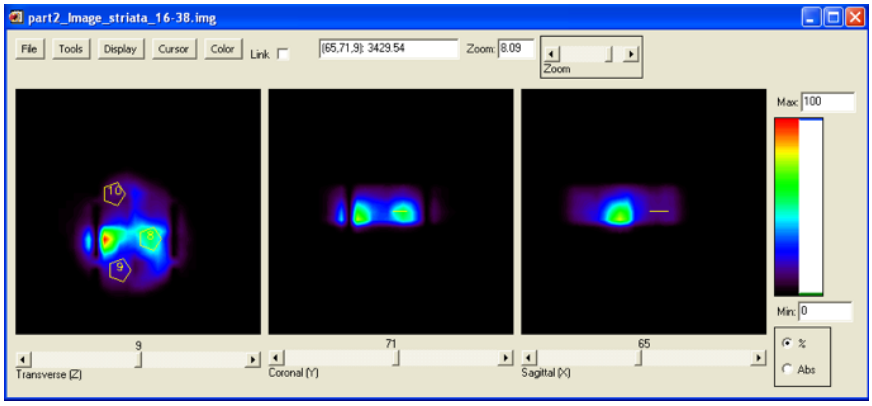

Figure 4.58: Striata phantom reconstruction using prototype-III PET

The missing voxels in the image are due to the failure to execute simulation in those voxels using SIMSET. Nevertheless, there is quite close agreement in the activity concentration ratios between the reconstructed image and the measured value.

A mechanical stand was designed and built for this PET ring such that it would allow translation in the axial direction. This stand consists of the four rods with clamps that lock onto the PET ring as shown in Figure 4.59.

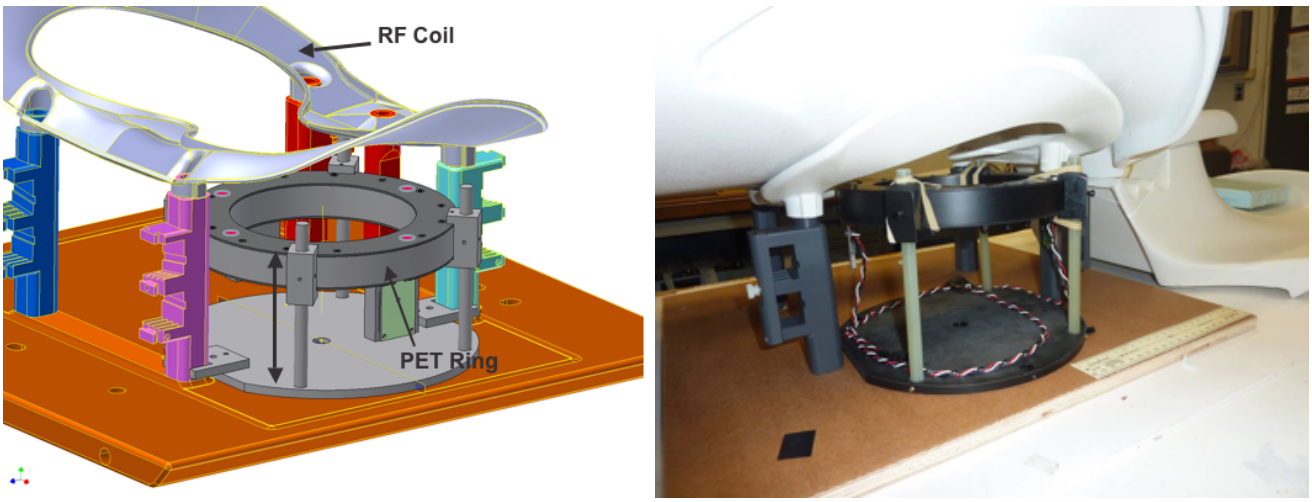

Figure 4.59: Mechanical stand for axial translation of prototype-III PET

The PET system was tested in the Aurora MRI for its effect on the MRI image quality and also the quality of the PET data. This time a more compact arrangement was possible due to the tetherless configuration. A new component was also added to the system to ease the routing of the PET data cables from the RF coil to the TSPM board on the table. Adapter boards were designed that would allow these cables to come out of the PET ring parallel to the patient table as shown in Figure 4.61a, 4.61b, instead of the original configuration shown in Figure 4.60 allowing greater flexibility in the translation and positioning of the system.

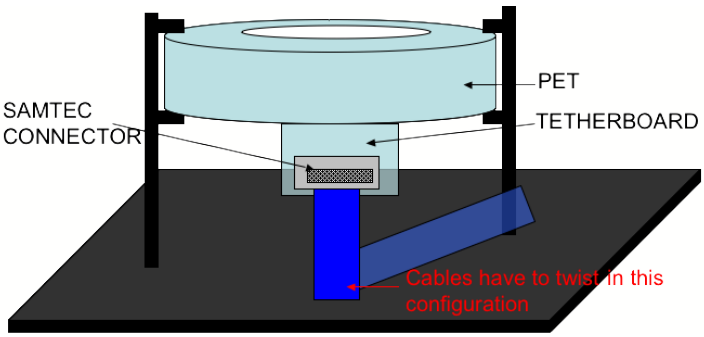

Figure 4.60: Configuration in which the data cable (blue) plugs into the PET tetherboard

It was observed that in this configuration, some of the channels were knocked off to acquiring no data during certain RF pulsing sequences. This seemed to be a function of the RF power that was injected into the system, as the gradients by themselves had no effect without RF power. The presence of the adapter boards and the tin coated power cables to the PET ring did cause artifacts in the MRI image. The adapter boards add two more data

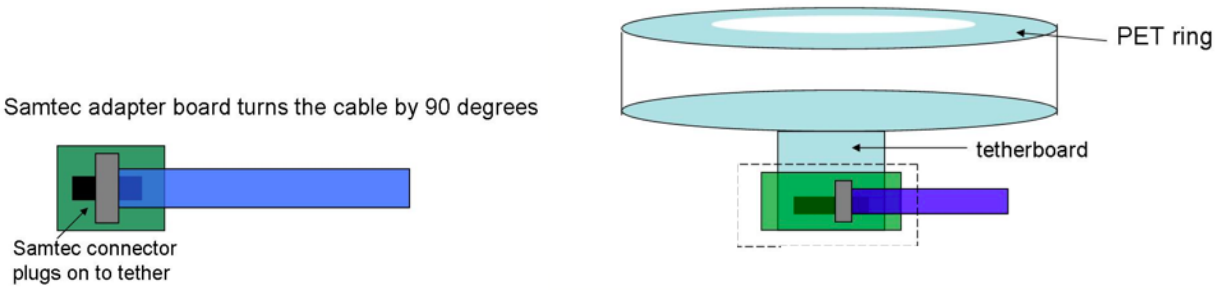

(a) Samtec adapter board

(b) Cable configuration with adapter board

Figure 4.61: Data cable configuration with adapter boards

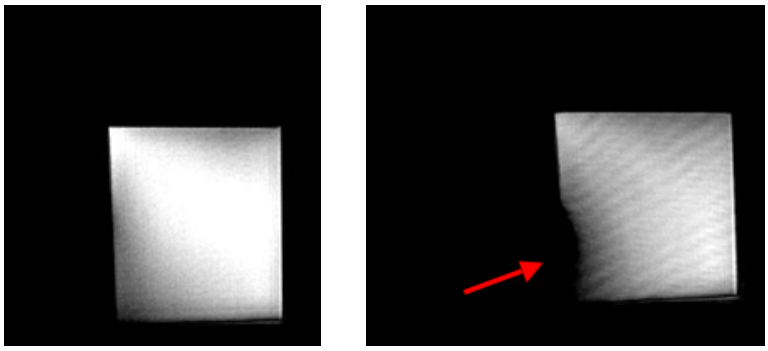

(a) Spiral RODEO MR image of uniform phantom without adapters on PET ring

(b) Spiral RODEO MR image with adapters on PET ring

Figure 4.62: MR signal loss due to adapter boards

cable connector pins to the PET ring, increasing the number of connectors from 2 to 4. The pins in the connectors are magnetic and hence cause signal loss as shown in Figure 4.62.

The tin coated copper cables were also replaced with bare copper cables to minimize any distortion that could be caused by the presence of tin. Loss in signal intensity and distortion due to the adapter boards are shown in Figure 4.62. The image on the left is with the phantom positioned in the PET ring and the adapter board plugged on the tetherboard, and the image on the right is an MRI scan of the phantom with the adapter board stuck to it. Hence, it can be clearly seen that the connectors on the adapter boards contain components that are magnetic in nature, and hence are a source of susceptibility artifacts. A fat phantom (schematic shown in Figure 4.63) was used for measuring fat suppression performance. It consists of two concentric cylinders with the outer cylinder filled with vegetable oil to mimic fat, and the inner cylinder is filled with doped water.

The signal to noise ratio of the MRI system was measured using the fat phantom shown

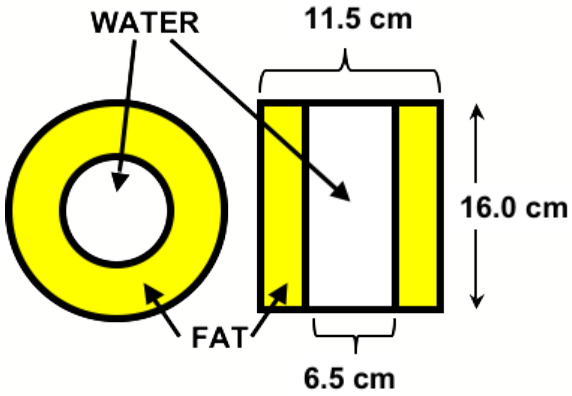

Figure 4.63: Schematic of fat suppression phantom

in Figure 4.64 without the adapter boards. The measurements again showed good signal to noise ratio with and without PET in the field of view. Fat suppression was also measured using the same phantom and the RODEO pulse sequence, and this is shown in Figure 4.65.

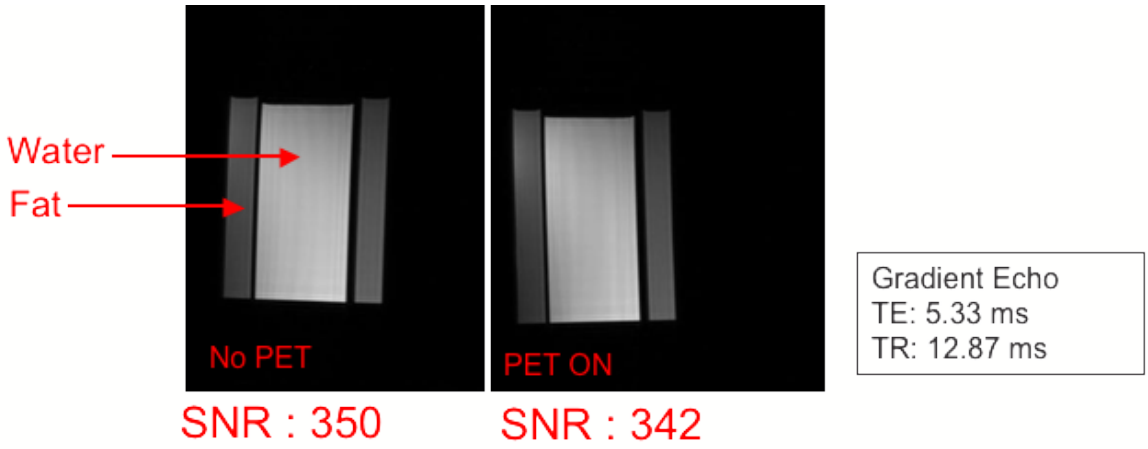

Figure 4.64: MRI SNR with prototype-III PET

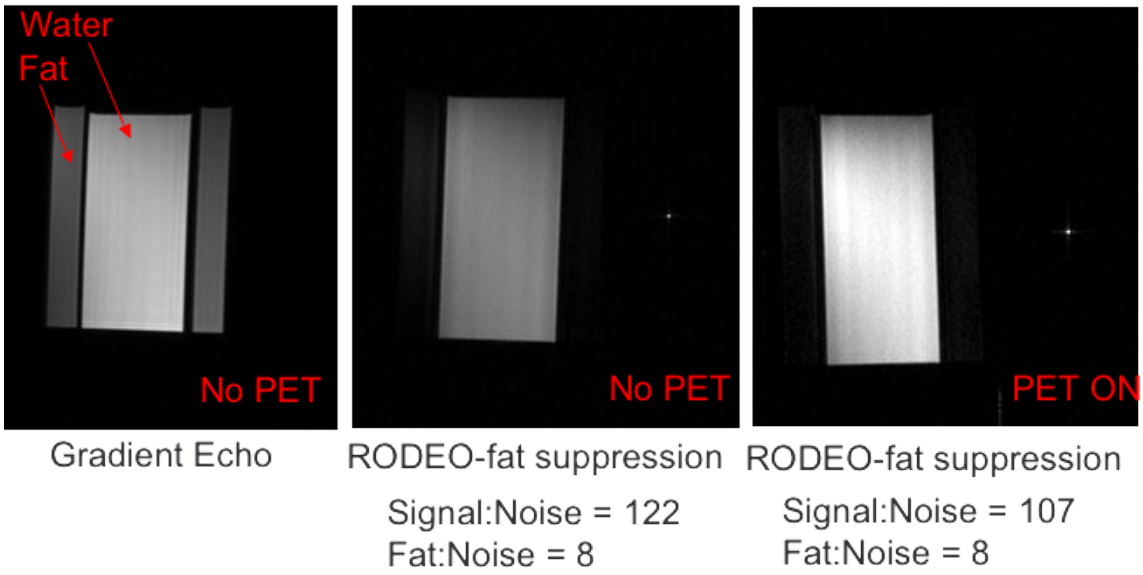

Figure 4.65: Fat suppression with prototype-III PET system

Chapter 5

Prototype PET-MRI Breast Scanner for Clinical Evaluation

5.1 Introduction and Design

The most crucial aspect of the design for the prototype breast PET scanner for the clinical trial was its transaxial field of view or diameter. The goal was to build a system of a diameter that would fit the breast of an average sized Asian woman without any or minimal compression. At the same time, it was also important to minimize this diameter from the PET point of view, as making the ring bigger will reduce scanner sensitivity, due to increased diameter (reduced solid angle coverage) and also the presence of "missing blocks"/gaps in the ring.

In order to identify the ideal diameter that was a good compromise between PET sensitivity and being able to image as many patients as possible, mock rings were constructed. These mock rings have inner diameters (ID) and outer diameters(OD) corresponding to 0-3 missing detector blocks in the PET ring shown in Table 5.1.

PET Geometry (missing blocks)	ID of PET Ring(mm)	OD of PET Ring(mm)
0	96.71	154.39
1	108.5	166.18
2	119.3	176.98
3	131.89	189.57

Table 5.1: Missing blocks in PET ring and corresponding inner and outer diameters

The calculations for the ID were made based on the size and the shape of the rigid flex circuits. These mock rings were shipped to the Aurora breast imaging center at the Taipei Medical University Hospital (TMUH), which was the site for the clinical study. These mock

rings were test fitted on incoming patients and it was determined that the ring with one missing block or with a maximum inner diameter (crystal face-face) of 112 mm, and an imaging ID of 108 mm would allow scanning of a good fraction of patients.

A system matrix was estimated for this geometry using SIMSET. The field of view was divided into 113 x 113 voxels transaxially, and 19 planes. The size of each voxel was 0.99 x 0.99 x 1.19 mm^3. 10 million decays per voxel were simulated.

Monte carlo simulations were carried out for this geometry of the scanner to evaluate its lesion detection capability as well as resolution. In order to test lesion detectability, a uniform cylinder phantom that covered the imaging field of view was simulated. Activity concentration of 0.065 uCi/cc was assigned to the background. Five lesions were simulated in this uniform phantom. Two lesions were of diameter 5 mm and three of diameters 8, 10 and 12 mm. Lesions were assigned an activity concentration 0.55 uCi/cc. The lesion to background ratio was 8.5:1. The sinograms were reconstructed using MLEM and the reconstructed image is shown in Figure 5.1.

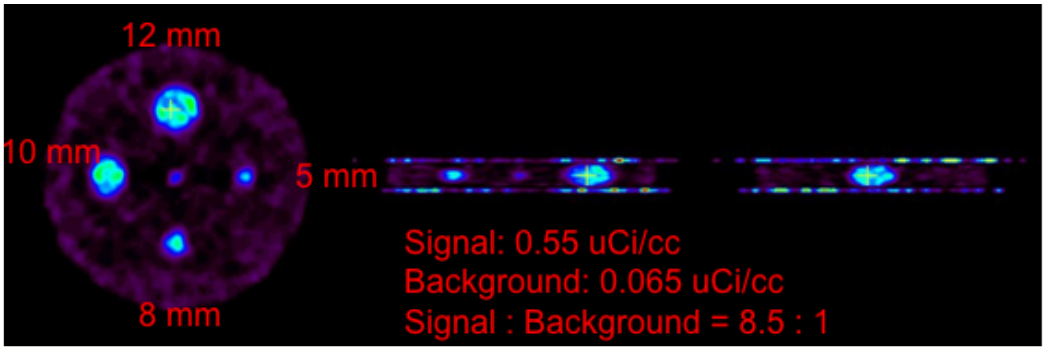

Figure 5.1: Simulated lesions in warm background using clinical prototype geometry and reconstruction

The simulations show good lesion detectability achievable by the scanner geometry and configuration. A mini deluxe or resolution phantom (Data Spectrum Corp., NC, USA) was also simulated for the clinical prototype. A reconstructed image is shown in Figure 5.2. A profile plot is drawn through the 2.4 mm rods, and shows that these rods can be distinguished.

Following the simulation studies, the clinical prototype PET ring was assembled. The rings were arranged such that there would be one missing block on each side as shown in Figure 5.3a. The flexes were housed in a enclosure made of plastic as shown in Figure 5.3b. Black colored plastic material was used to help keep the detectors light-tight.

A mechanical stand was designed and built for this geometry of the PET ring. The stand was built such that it was non metallic and would allow movement of the PET ring so that the ring can be positioned to cover the tumor under study. The PET ring had to be movable in the axial direction and also be positioned at an angle as shown in Figure 5.3. The angular positioning was necessary due to the natural shape of the RF coil/table of the

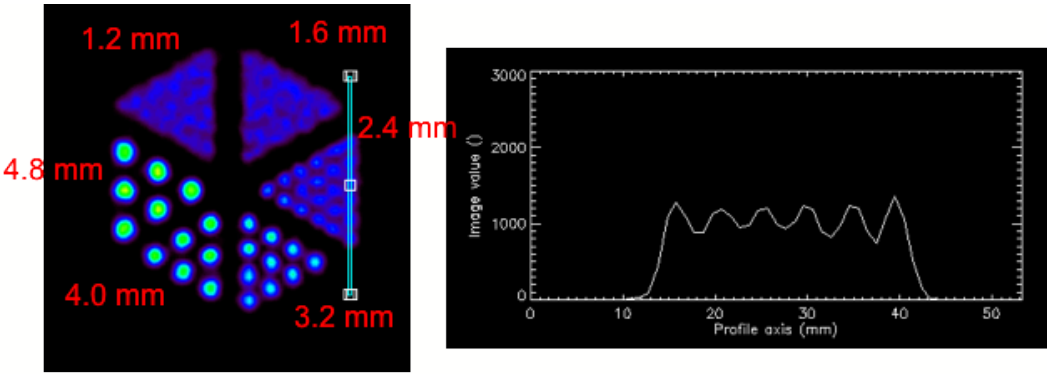

Figure 5.2: Simulated resolution phantom reconstruction using clinical prototype

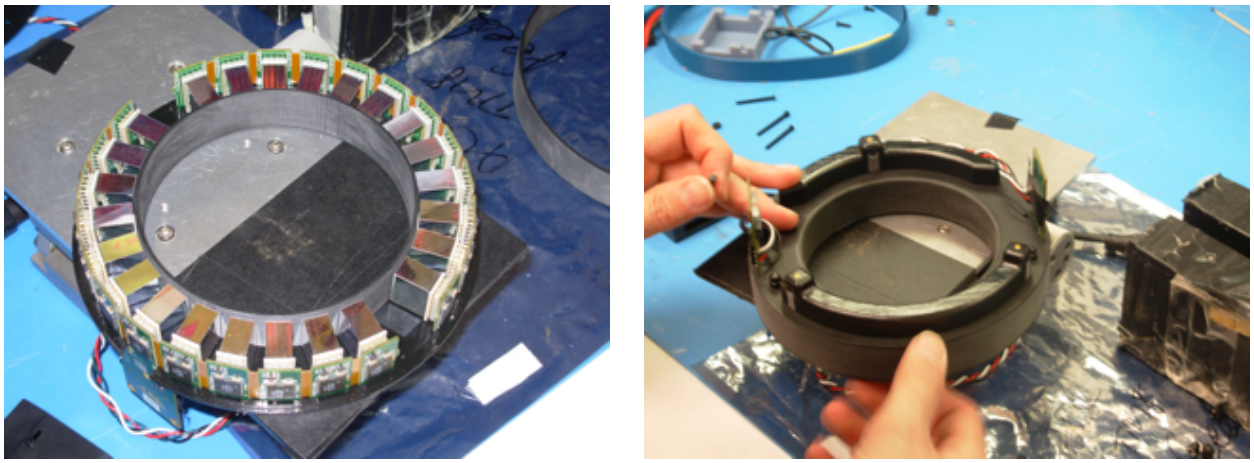

(a) Clinical prototype assembly

(b) Prototype in black plastic housing

Aurora scanner which has a curved shape as shown in Figure 5.4.

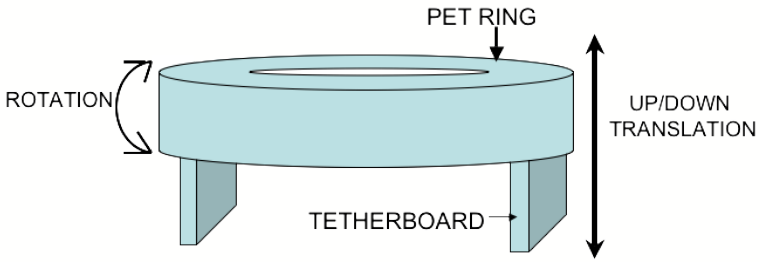

Figure 5.3: Rotation and translation requirements for prototype PET

A mechanical stand for mounting and positioning the PET ring was built and is shown in Figure 5.5. Blocks mounted on the three rods of the stand extend into the base of the

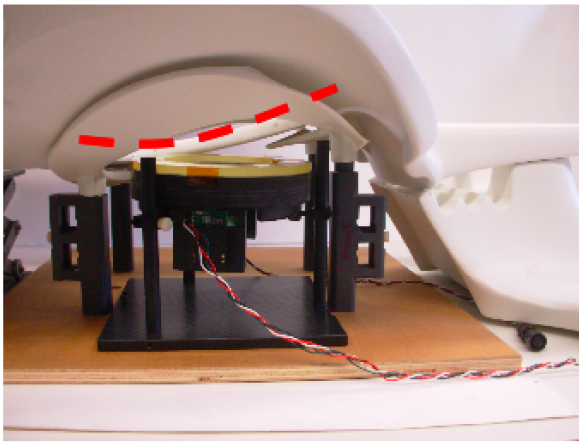

Figure 5.4: Aurora RF coil with curved surface (indicated in red)

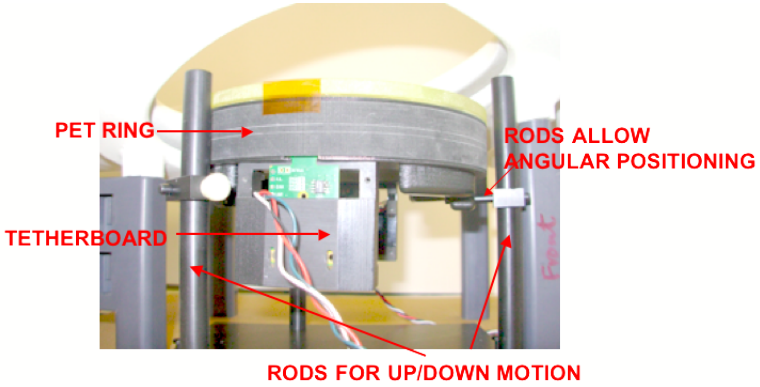

Figure 5.5: Stand for the PET ring

scanner via rods that are flexible. The PET scanner can be rotated on the stand, thereby allowing adjustability of the detector gap location in the ring with respect to the lesion being imaged.

5.2 PET System Setup and Measurements

5.2.1 Gamma Shielding

The positioning of the PET ring around the patient's breast puts it at very close proximity to the heart, especially in cases where the tumor is close to the chest wall. The heart is an organ of high FDG uptake, and hence a source of high background activity. Such high background activity, can cause high randoms rate in the PET data, thereby rendering the images noisy and uninterpretable.

A way to counter this problem is through the use of gamma shielding. However, in the MRI, gamma shielding is tricky. The use of a high density metal in the MRI field of view, can cause number of problems in the image quality. Signal loss and distortion can occur due to factors such as susceptibility artifacts, and formation of eddy currents during the RF and gradient pulsing of the MRI pulse sequence [123]. Hence, one has to carefully evaluate the tradeoff between the artifacts in the MRI image to PET image quality due to randoms rejection.

In our case, we evaluated two materials : lead(Pb) glass and tungsten(W) composite material. Both these material have advantages over traditional shielding materials, in that they are non conducting and hence do not form eddy currents. The lead glass material used for our purpose is shown in Figure 5.6. A lead glass sheet available in the laboratory was cut using water jets into a ring shape that matches the profile of the PET ring. The glass has a thickness of 6 mm and is positioned on the PET ring and in the RF coil as shown in Figure 5.6b(right) with the help of double sided and Kapton tapes.

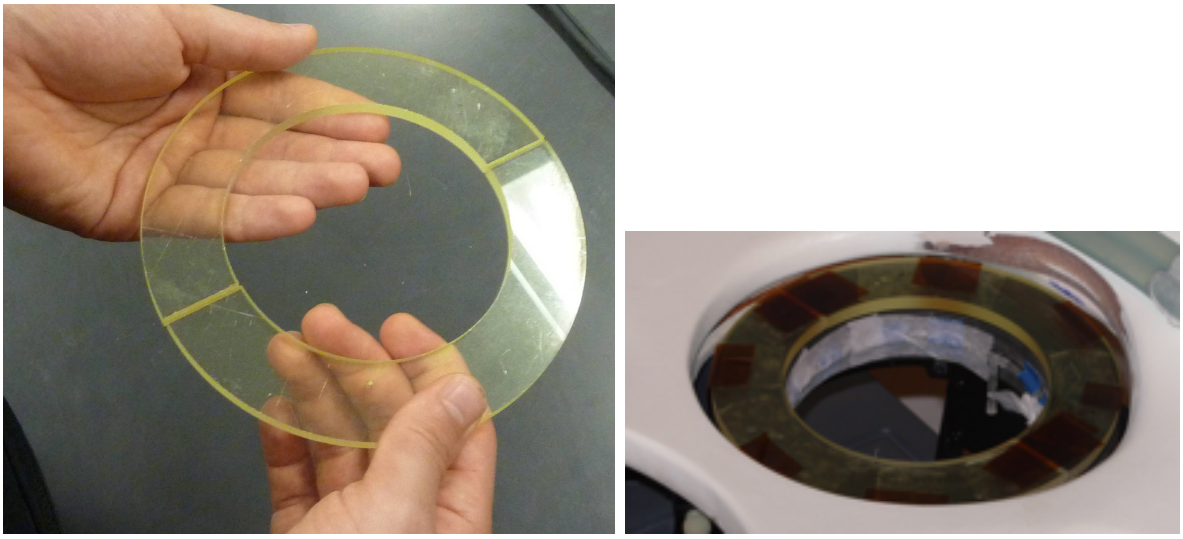

Figure 5.6: Lead glass shielding

The tungsten composite sheets were molded as 1 mm thick rings. These sheets could then be stacked together to give the desired attenuation. MRI tests were carried out to determine the compatibility of the shielding materials. From these tests, use of a single tungsten composite sheet and/or lead glass was acceptable with regard to the MRI image quality. For the clinical tests, the tungsten ring was covered with high voltage rubber tape and Kapton tape as shown in Figure 5.7.

The background suppression that can be achieved using all possible combinations of shielding material, i.e lead glass only, tungsten sheet only, and lead glass + tungsten sheet was evaluated. Two 4.0 liter plastic bottles filled with water and containing approximately 0.73 mCi and 0.7 mCi each of [^{18}F]-FDG at the start of the experiment were positioned

Figure 5.7: A 1mm thick W sheet for background shielding, covered with high voltage rubber tape and Kapton tape(right)

on the RF coil/patient table as shown in Figure 5.8. The PET ring was positioned under these phantoms; data was acquired sequentially under various shielding configurations and compared to the unshielded condition. Percentage suppression in the singles count rate from the unshielded PET is shown in Figure 5.9. The singles counts were corrected for decay.

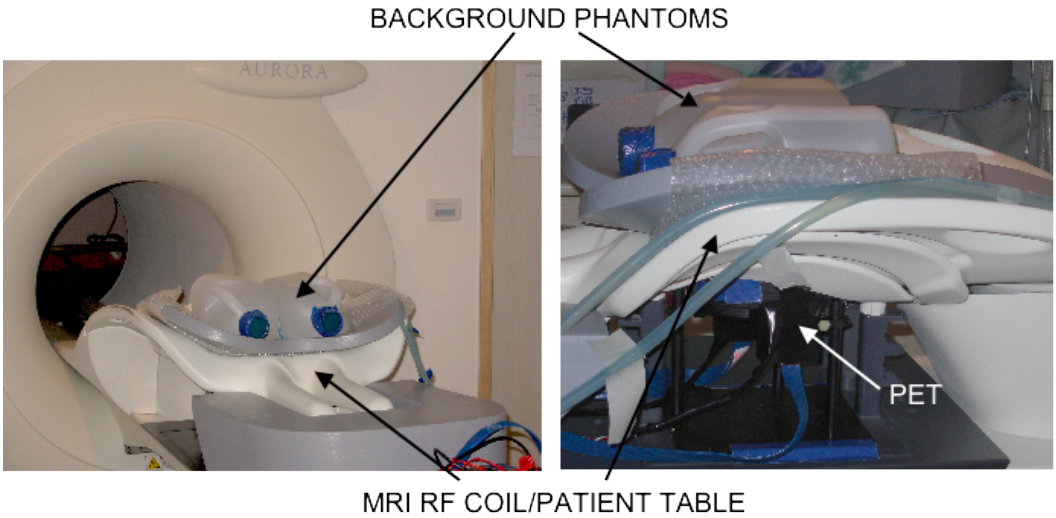

Figure 5.8: Phantoms for evaluating shielding effectiveness of Pb glass/ W sheet/ Pb + W from background activity

5.2.2 Temperature Measurement

The breast PET system is not actively cooled. Hence, temperature measurements were made inside the breast scanner using the Lakeshore 218 temperature monitor (Westerville, OH).

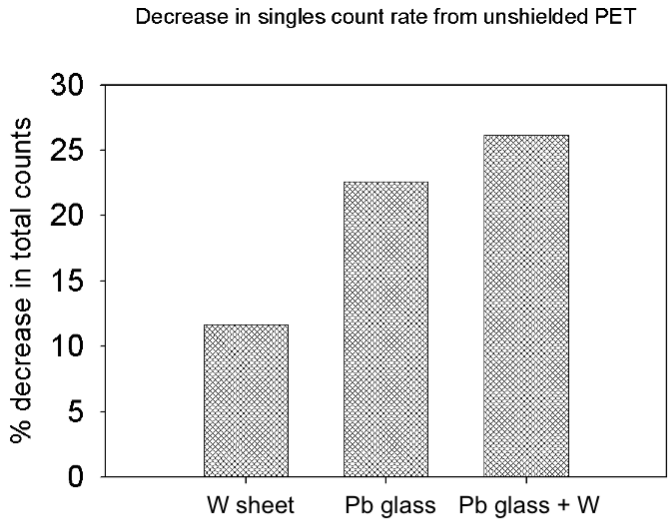

Figure 5.9: Percentage decrease in background from unshielded PET using various gamma shielding configurations

It is important to know the temperature profile in the scanner due to the fact that APD gains are highly temperature dependent (3 % per degree change in RatCAP) and can affect scanner performance. For the temperature measurements, one probe was positioned next to the chip to measure temperature inside the scanner as shown in Figure 5.10 . The second probe was placed on the scanner housing, while the third probe was used to measure the room temperature. A plot of temperature versus time with PET power on (red arrow), and power off (green arrow) is shown in Fgure 5.11. Temperature data was acquired every 5 minutes. According to the plots, it takes approximately 60 minutes for the temperature to start to stabilize (area indicated by blue arrow). The scanner housing temperature increased by approximately 3°C over the room temperature on PET power ON. Based on these measurements, efforts were made to keep the scanner powered on for at least 60 minutes before measurements were made using it.

5.2.3 Localization of the PET ring in the MRI

With the MRI field of view fixed due to the RF coil being embedded in the table, the PET ring could be positioned in multiple locations within the MRI field of view. The PET system does not produce any signal in the MRI image, and hence fiducial markers were placed on the PET ring so that its position within the MRI FOV and with respect to the lesion of the patient under study could be visualized. The axial length of the PET scanner is limited to 1.8 cm, hence one could potentially miss the tumor if the scanner is not aligned

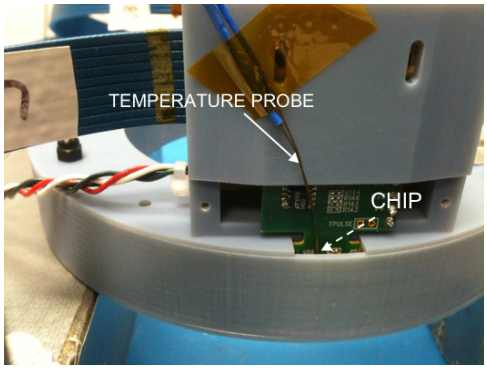

Figure 5.10: Temperature measurement setup

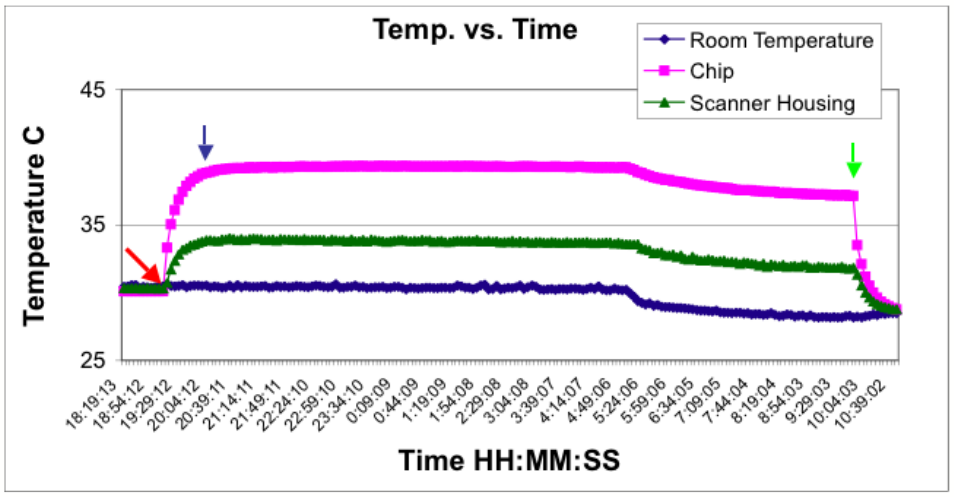

Figure 5.11: Plot of temperature vs. time for prototype scanner power up and power down

accurately with the height of the tumor. Positioning of the PET ring based on the calculated height of the tumor from the patient's pre-scan MRI needed to be confirmed at the time of PET-MRI scanning since positioning is not exactly reproducible and some patients had images acquired with a thick and compressible table padding. For the PET-MRI scan, it was decided to not use the thick padding and instead using a wool blanket so that the breast can be pushed further into the opening of the RF coil hence allowing the PET scanner more axial positioning flexibility. As a fiducial marker, a plastic tube of inner diameter 1.6 mm was filled with 1mM copper sulfate solution was used. A "T" junction was also part of this marker as shown in Figure 5.12a, 5.12b. The tube was lined along the center of the inner ring of the PET scanner. The use of such a ring that spanned most of the ID of the PET ring was beneficial as one could see the position of the PET ring in almost all the planes of the coronal MRI image (which is the Aurora MRI acquisition plane). An example of this is

shown in Figure 5.12b.

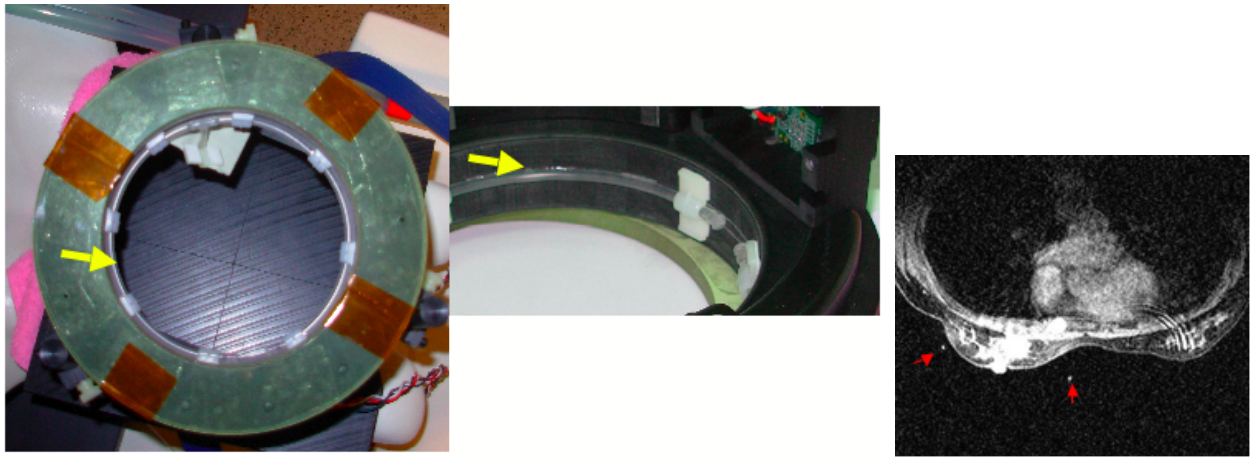

(a) MRI marker tube lining the ID of the PET ring

(b) MRI image of a patient with PET ring shows the PET plane/marker tube cross section - indicated by arrows

Figure 5.12: Fiducial markers for visualizing PET ring in the MRI image

5.3 Clinical Setup

The PET system and the associated electronics, were shipped to the Aurora breast imaging center at Taipei Medical University Hospital, Taiwan. The setup for the simultaneous PET-MRI measurements is illustrated in Figure 5.13. The corresponding photographs of the individual components of the setup is shown in Figure 5.14.

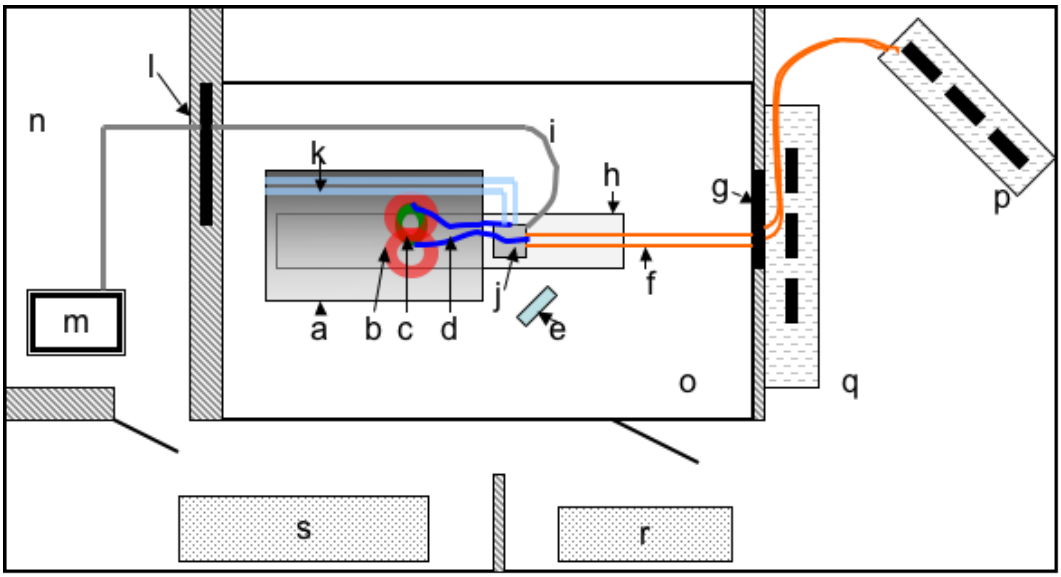

Figure 5.13: Simultaneous PET-MRI - room layout; a: MRI Bore, b: RF coil, c: PET ring, d: Data cables, e: Power injector, f: Fiber optic cables, g: penetration panel, h: MRI table, i: Filtered PET power cables, j: TSPM, k: Water cooling tubes, l: Penetration panel to electronics room, m: PET power supplies, n: MRI electronics room, o: MRI room, p: PET control station, q: MRI control station, r: Patient preparation area, s: Patient waiting area. The photographs of the actual setup are shown in Figure 5.14

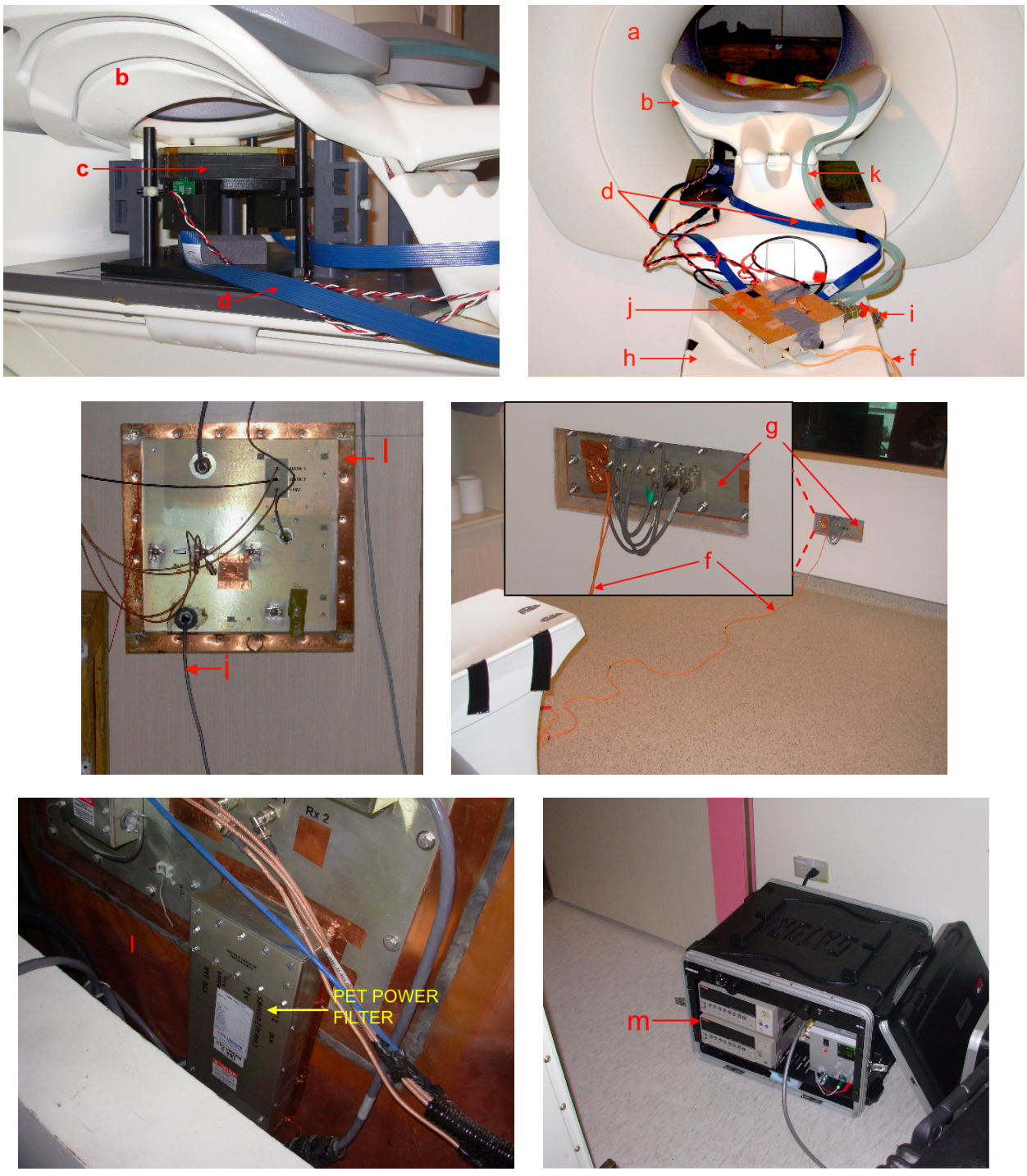

Figure 5.14: Photographs of the setup illustrated in Figure 5.13

5.4 Clinical Protocol

The goal of the clinical protocol was to evaluate the feasibility of simultaneous PET/MRI in the patient population and the clinical setting. The protocol was approved by Stony Brook and Taiwan institutional review board (IRB).

Inclusion Criteria: Patients (older than 18 years of age) who have been previously diagnosed with breast cancer or have a highly suspicious lesion(s) were recruited for the study.

Exclusion Criteria: Since the study involved MRI, standard exclusion criteria such as tattoos, metal implants in the body, pacemakers, defibrillators, aneurysm clips, certain heart valves, spinal nerve stimulators, artificial joints/limbs, shrapnel/bullets, metal fragments in their eyes, cochlear implants, hearing aids, dental implants and allergy to contrast agent were applied. Women who were pregnant, or breast feeding were excluded from the study.

Study Design: The study starts with a consultation between the physician and the patient. Once a patient who meets the inclusion criteria is identified, a MRI pre-scan is conducted. The MRI pre-scan is used to localize the lesion and determine if it can be covered by the PET scanner. Following the pre-scan, the patient returns on a different day for the simultaneous PET-MRI study. The subject is instructed to fast from the night before the study. On the day of the test, a blood glucose test is conducted after which the subject is injected with [^{18}F]-FDG . After approximately 40 minutes of uptake period, a supine whole body PET scan is conducted in the Siemens ECAT ACCEL scanner. The whole body PET scan goes on for 40 minutes. After the completion of the whole body scan, the patient is repositioned for a prone position chest scan on the same scanner. This scan's duration is 15 minutes. After the completion of the chest PET scan on the whole body PET scanner, the patient is escorted to the Aurora breast center for the simultaneous PET-MRI scan. During the time where the whole body PET scans are being conducted, the simultaneous PET-MRI breast scanner is set up. The prototype PET ring positioned at the estimated location of the lesion along with appropriate gamma shielding (Pb/W/Pb+W). The PET scanner is kept powered on for at least 60 minutes before the actual start of the patient scan in order to let the temperatures to stabilize. During this time, the system is programmed at the correct gain and threshold values, and tested for any problems in data acquisition.

Once the patient arrives at the breast MRI center for the simultaneous PET-MRI scan, she is prepped for contrast injection. For patient-1, contrast injection prep was done after the [^{18}F]-FDG injection, but for the following 3 patients, it was done before the radiotracer injection in order to minimize radiation exposure to the personnel(s). The patient is then positioned onto the PET - MRI scanner in the prone position and the breast is eased into the ring. The positioning of the patient is optimized for maximum comfort as well as coverage with the PET system. The location of the lesion and its overlap with the PET scanner is confirmed by communicating with the patient, and feeling the lesion, and readjustments to the height of the PET scanner is made if necessary. The patient is then positioned into the bore of the MRI scanner, and the simultaneous acquisition is ready to begin.

The PET-MRI scan starts off with a scout scan, which is followed by the pre contrast RODEO sequence (MR-1). The start of the PET scan and MR-1 is coordinated so that the PET scan starts approximately 5 seconds before the MRI scan. PET-1 data acquisition is stopped once the MR-1 gradients stop pulsing. At this point, the patient has to be injected with MRI contrast material. The second portion of the PET scan (PET-2) starts which continues for the two consecutive post contrast MRI scans. After the completion of simultaneous PET-MRI acquisition, PET data without any MRI pulsing is acquired with the patient in the same position, inside the MRI bore, for a period of 15 minutes. After the acquisition of PET only data, the patient is escorted back to the whole body PET center for a delay phase prone chest PET scan, after which the patient is free to go home.

At the breast center, once the patient is removed from the PET-MRI scanner, without disturbing the positioning of the PET ring , a mini deluxe phantom filled with [^{18}F]-FDG is inserted into it. This scan is conducted with the PET ring inside the MRI bore. An MRI scan of the phantom is also acquired in this position.

5.4.1 Participating Subjects

Four women with biopsy proven, or suspicious lesions were recruited in the study. The study was conducted in accordance with the IRB protocol. Table 5.2 gives an overview of demographics and study details of the participating subjects.

Patient	Age	Dose injected (mCi)	Lesion location	Diagnosis	Biopsy
1	45	8.38	Superior right breast	Invasive ductal carcinoma	Post
2	59	8.91	Left breast	Pending	Pending
3	40	8.67	Left breast	Invasive micropapillary carcinoma	Pre
4	40	8.69	Left breast	Tubular adenoma	Post

Table 5.2: Overview of participating patients

The MRI and PET image acquisition parameters are described in Tables 5.3, 5.4.

Results for the participating subjects are shown in the following section. Data presented for each subject includes the following-

1. Overview of study parameters for each subject - Here, the date of the PET-MRI study, the age of the patient, injected dose, time of injection, time of PET-MRI and whole body/prone PET scans, date of biopsy and the corresponding pathology report if available is listed.

MRI Imaging parameters	
RODEO pulse sequence	
TE	4.81 ms
TR	11 ms
RF duty factor	40.9% (RF period = 4.5 ms)
FOV	360 mm x 360 mm x 180 mm
Image matrix	512 x 512 x 128
Scan duration	306 s

Table 5.3: MRI imaging parameters used in the clinical study

PET Imaging parameters	
List mode data	
Voxel size	1 x 1 x 1.19 mm^3
Lower Level Discriminator	340 mV
Scan duration	duration of MR precontrast and post contrast imaging period - approx. (3 x 309) s

Table 5.4: PET parameters used in the clinical study

2. PET - Analysis results of the PET data acquisition. Here, the contribution of the true and randoms coincidences is plotted as a function of transverse sinogram planes 1- 8 (Figure 5.15).

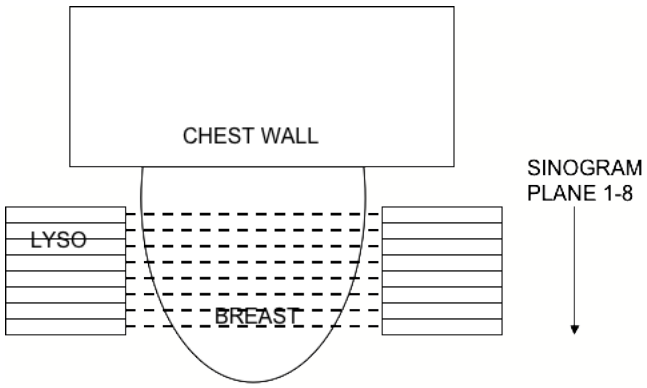

Figure 5.15: Sinogram planes 1-8 used for showing contribution of randoms and true coincidences for each patient

The sinogram plots for each subject are shown in Figures 5.16, 5.22, 5.28, 5.34. "P" denotes prompt or total coincidences, "D" denotes delays/random coincidences and "trues" were obtained by subtracting delays from prompts.

Sinograms obtained using a coincidence window of 30 ns, during PET only and simultaneous PET-MRI acquisition are shown for each subject. For the simultaneous PET-MRI images, RF pulsing of the MRI sequence induces noise in the PET data stream. This is illustrated for each subject in Figures 5.17, 5.23, 5.29 and 5.35. From the simultaneous PET-MRI sinograms, one can see that this noise results in high count rate elements in the coincidence data. One approach towards getting rid of this noise is by eliminating (or setting to zero) the LOR bins in the sinogram that have count rates higher than a certain threshold. This threshold was determined from the coincidence rate in the "PET only" sinograms, which is free of any MRI induced noise. A threshold cut-off of 20 counts/bin was applied to the PET-MRI sinograms of all the participating subjects. The sinograms are shown in Figures 5.18, 5.24, 5.30 and 5.36. The PET only sinograms and the thresholded simultaneous PET-MRI sinograms are reconstructed using MLEM. The images obtained after 20 iterations of MLEM reconstruction are shown in Figures 5.19, 5.25, 5.31 and 5.37.

3. MRI - The first post contrast MRI images for each subject are shown in Figures 5.20, 5.26, 5.32 and 5.38. The position of the PET ring is also shown as red dotted line.

4. Simultaneous PET-MRI - The reconstructed PET and MRI images are overlaid for each subject and shown in Figures 5.21, 5.27 and 5.33. PMOD software (PMOD technologies, Zurich, Switzerland) was used for reslicing and overlaying the images.

5.5 Results

5.5.1 Patient 1

Patient #1	
Date of PET-MRI	04/26/2011
Age	45 y
Injected dose	8.38 mCi
Time of radiotracer injection	12:40 pm
Whole body PET start time	13:20 pm
Prone PET start time	14:10 pm
PET-MRI contrast injection time	14:54 pm
MRI report	3.1 cm ill defined mass with DCE pattern indicative of malignancy
Biopsy date	04/29/2011
Pathology report	Invasive ductal carcinoma

Table 5.5: Overview of study parameters of patient 1

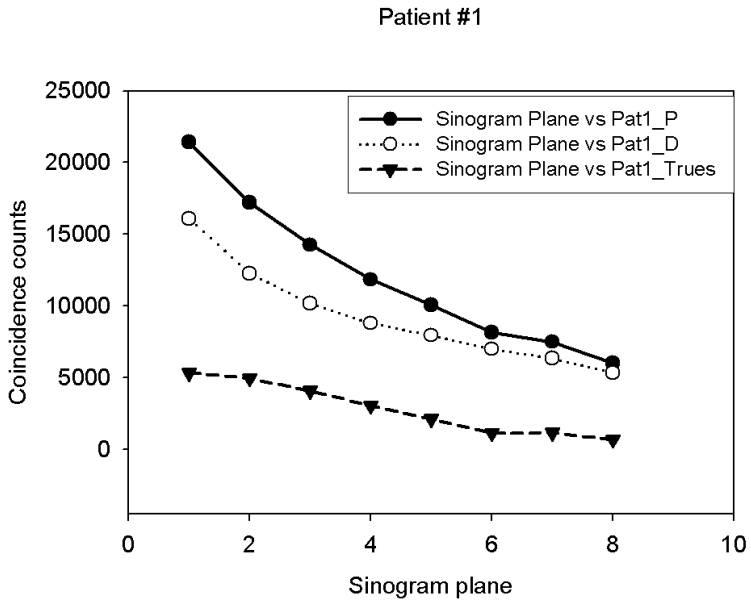

Figure 5.16: Random and true coincidences for "PET Only" condition as a function of sinogram plane - Patient 1

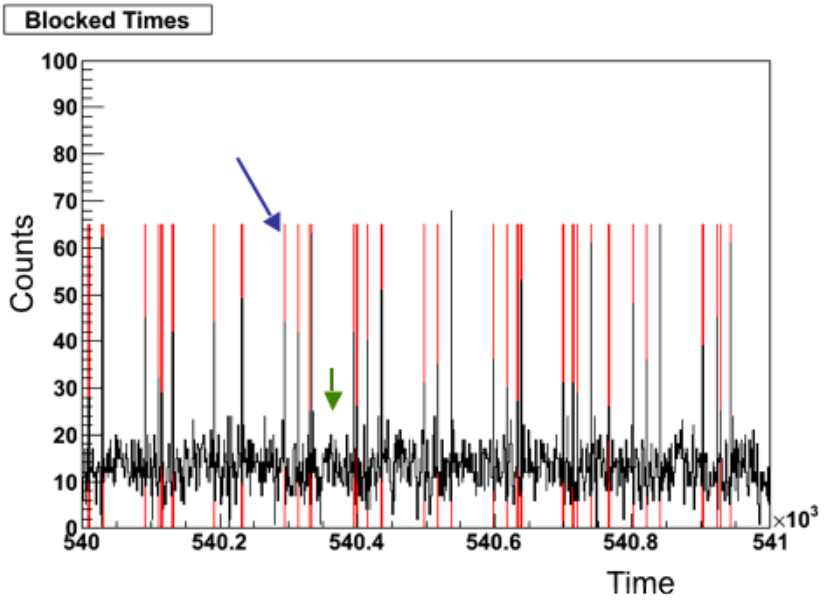

Figure 5.17: Spikes due to RF pulsing in PET data stream - patient 1, blue arrow - spikes, green arrow - RF off

Summary - Patient1

Patient 1 was scanned with tungsten sheet as a shielding material. Reconstructed PET and MRI images show good image quality and correlation upon overlay. The removal of high count elements from the sinogram effectively suppresses the noise due to RF pulsing in the PET image. The patient's cancer is close to the chest wall, hence the PET ring was not able to completely image the lesion. The fraction of random coincidences in the PET data is high due to the close proximity of the ring to the chest wall. However, counts due to the lesion can be clearly seen on the PET sinogram.

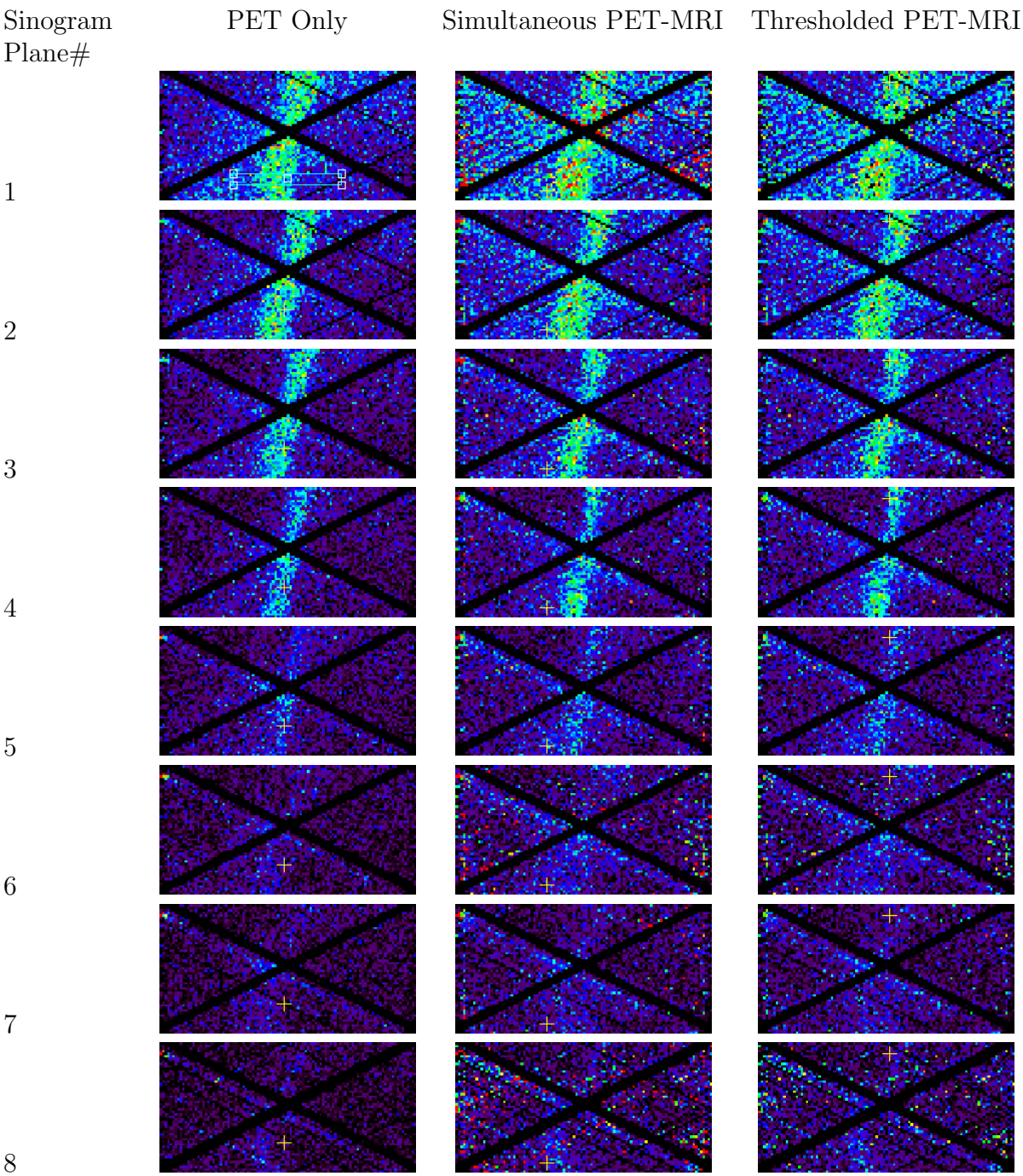

Figure 5.18: Sinograms for Patient 1

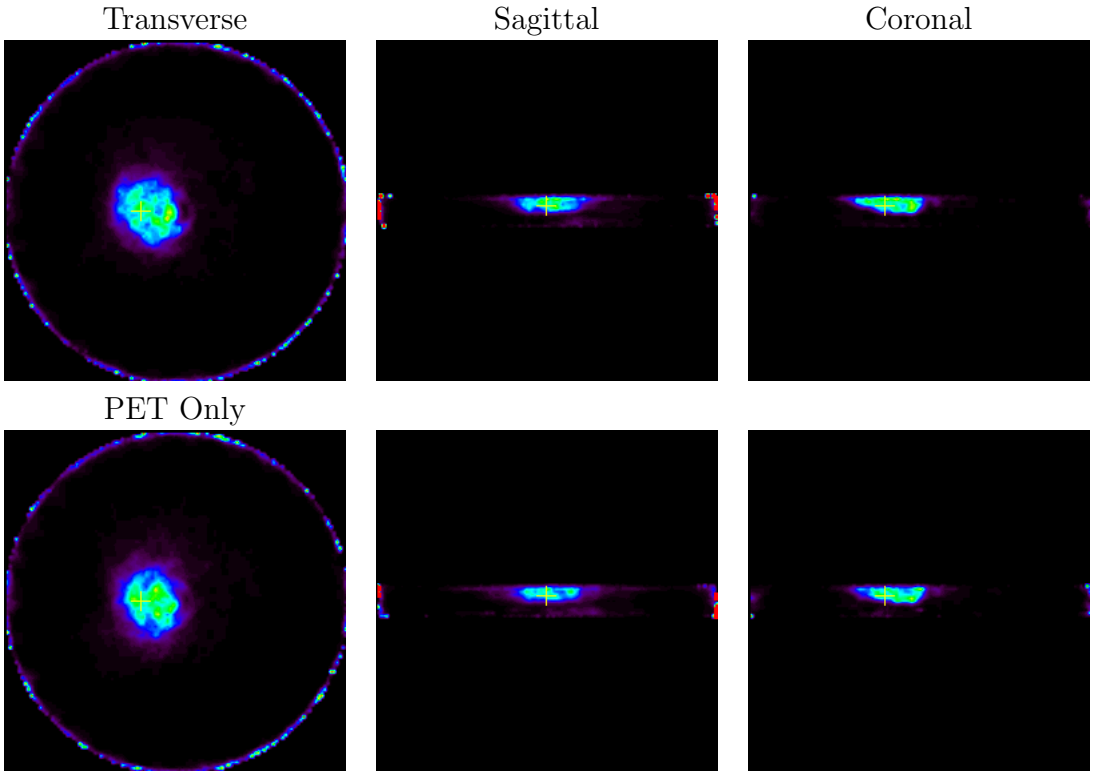

Figure 5.19: PET images - Patient 1

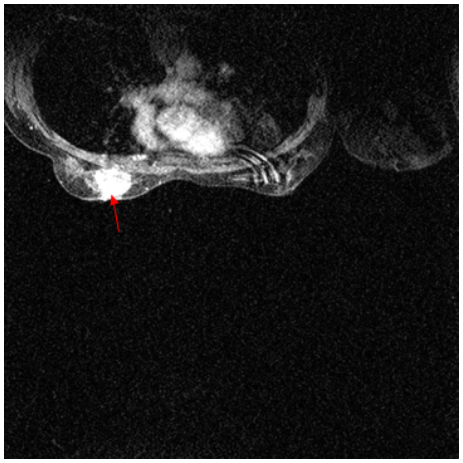

Slice 73

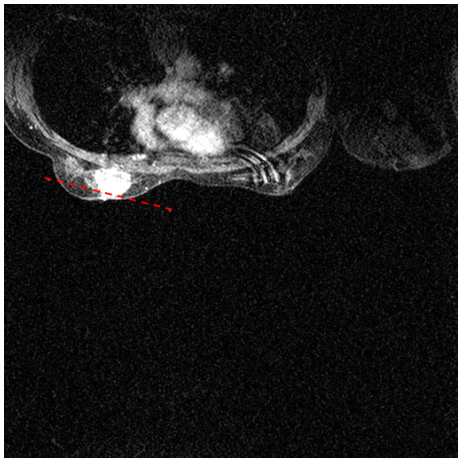

Slice 73 showing PET centerline

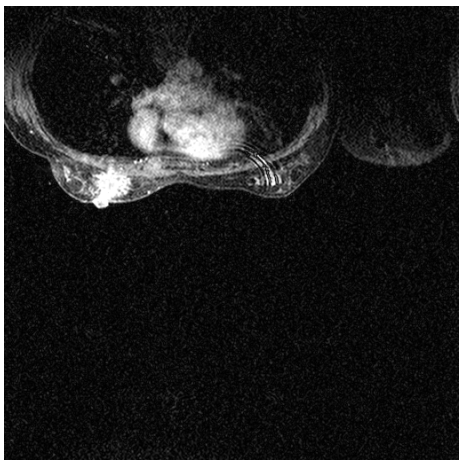

Slice 77

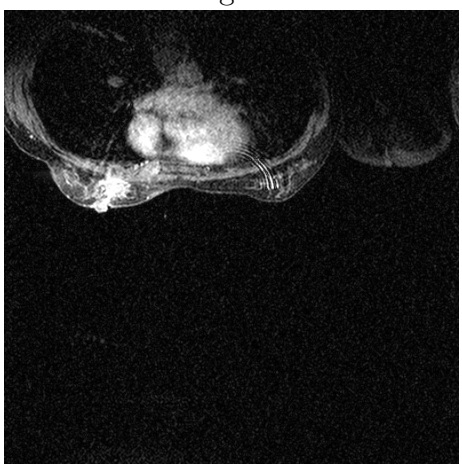

Slice 79

Figure 5.20: Patient 1, Post-contrast MRI

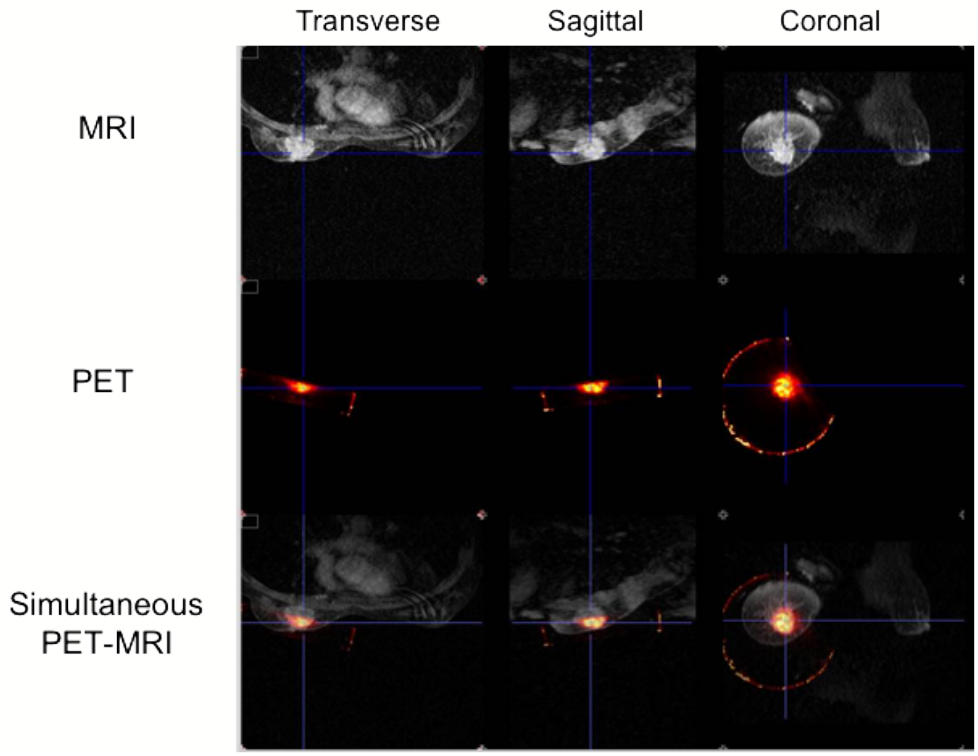

Figure 5.21: Simultaneous PET-MRI - Patient 1

5.5.2 Patient 2

Patient #2	
Date of PET-MRI	05/03/2011
Age	59 y
Injected dose	8.91 mCi
Time of radiotracer injection	13:34 pm
Whole body PET start time	14:14 pm
Prone PET start time	15:23 pm
PET-MRI contrast injection time	16:30 pm
MRI report	na
Biopsy date	na
Pathology report	na

Table 5.6: Overview of study parameters of patient 2

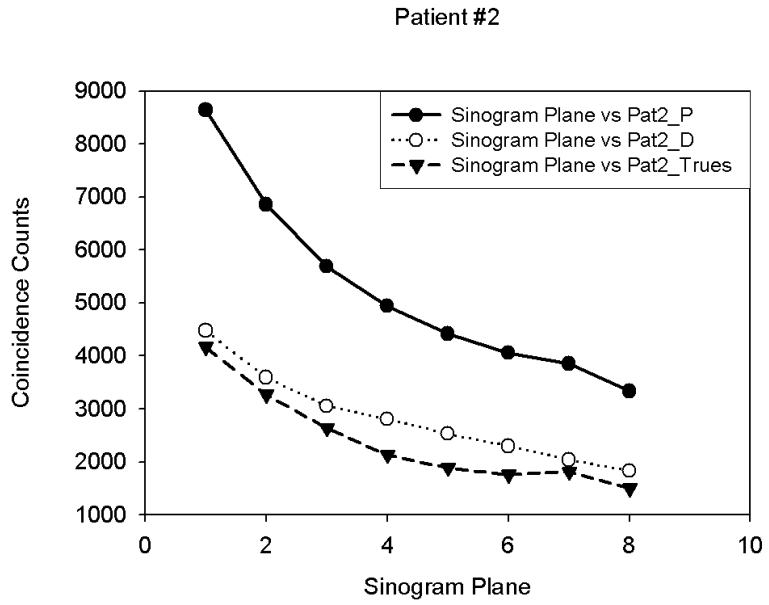

Figure 5.22: Random and true coincidences for "PET Only" condition as a function of sinogram plane - Patient 2

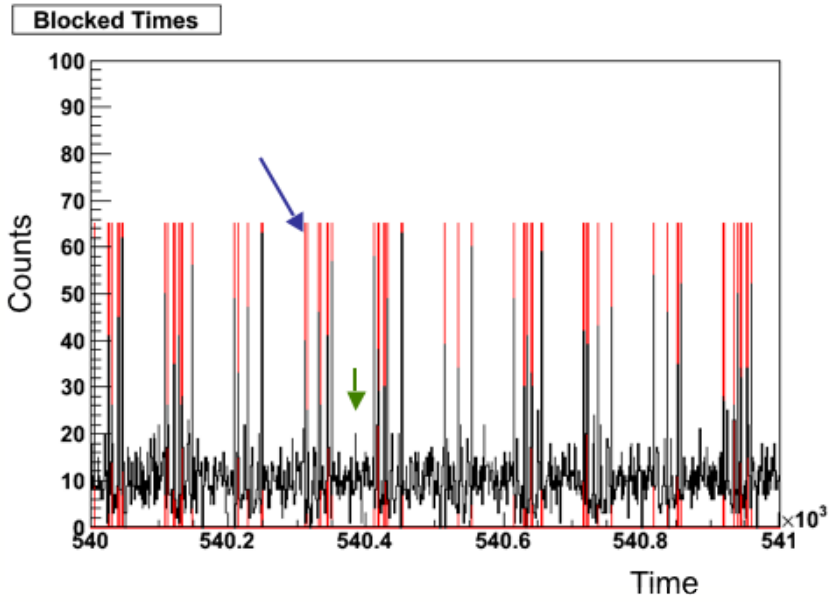

Figure 5.23: Spikes due to RF pulsing in PET data stream - patient 2, blue arrow - spikes, green arrow - RF off

Summary - Patient2

Patient 2 was scanned with lead glass as shielding material. Reconstructed PET and MRI images show good image quality. Only a small section of the lesion was imaged by the breast scanner due to the fact that the patient's breast was a little too large for the ring. The breast could have been eased into the PET ring, however, the patient reported pain at the lesion site hence this was avoided. Another problem faced during this study was the leakage of MRI contrast agent during injection, which prevented the entire contrast material to be administered into the patient. Hence, the MRI post contrast images do not show a strong uptake in the tumor. PET sinograms show the lesion clearly and MR noise is well suppressed by thresholding of the sinogram.

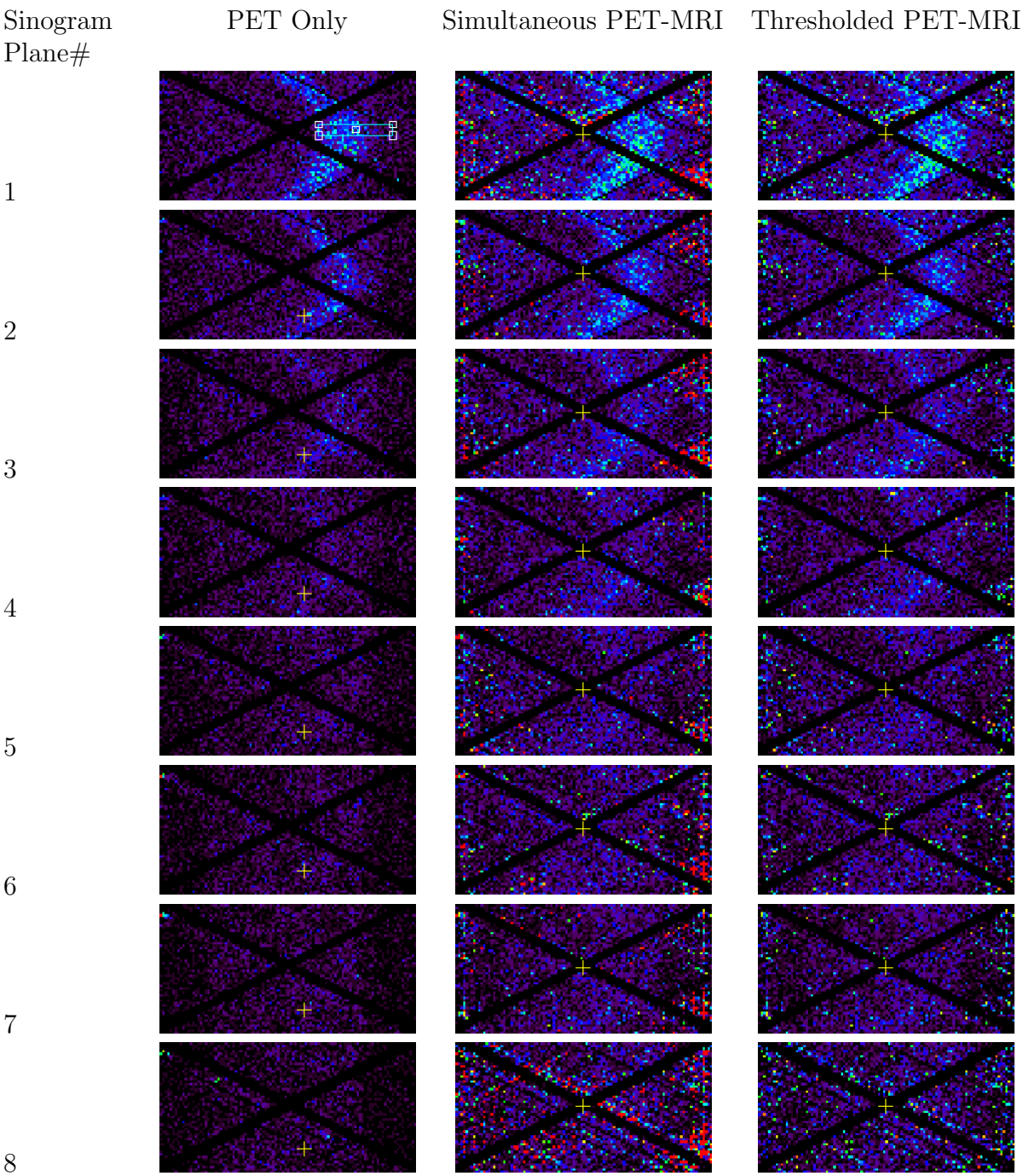

Figure 5.24: Sinograms for Patient 2

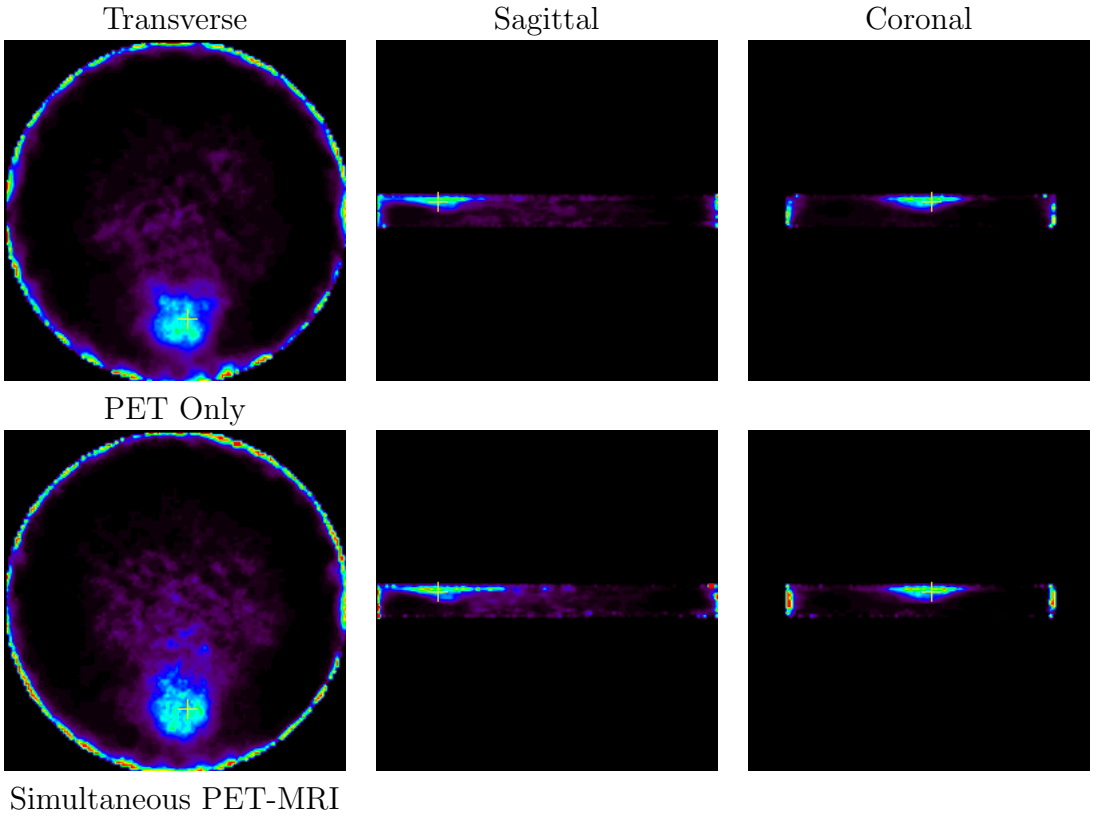

Figure 5.25: PET images - Patient 2

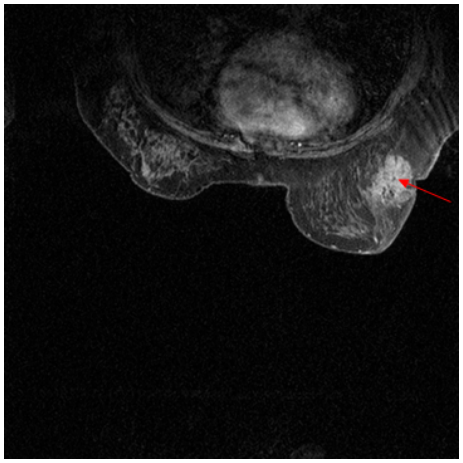

Slice 58

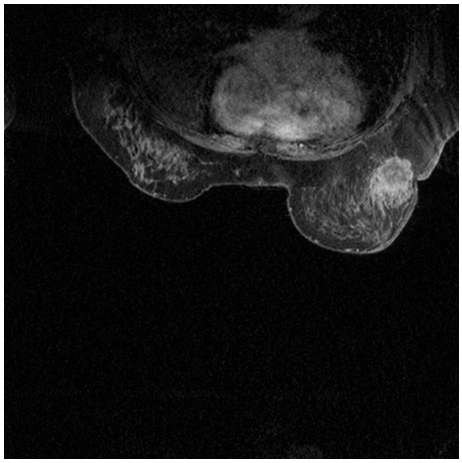

Slice 63

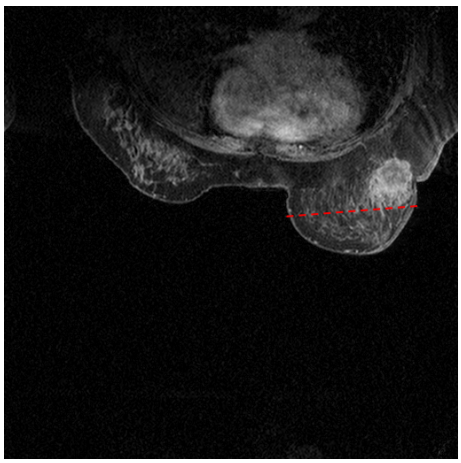

Slice 63 showing PET centerline

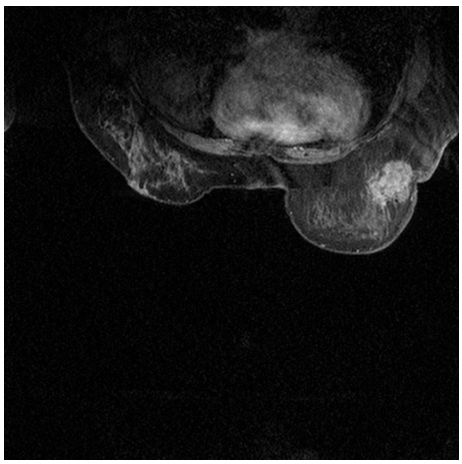

Slice 67

Figure 5.26: Patient 2, Post-contrast MRI

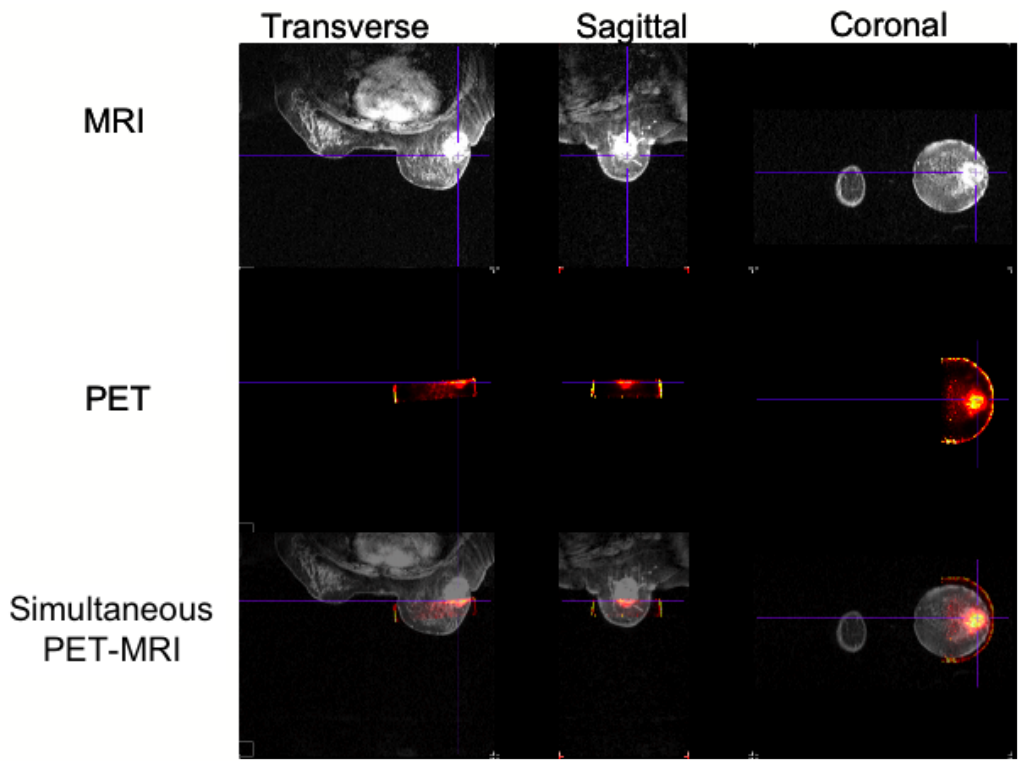

Figure 5.27: Simultaneous PET-MRI - Patient 2

5.5.3 Patient 3

Patient #3	
Date of PET-MRI	05/05/2011
Age	40 y
Injected dose	8.67 mCi
Time of radiotracer injection	13:33 pm
Whole body PET start time	14:25 pm
Prone PET start time	15:12 pm
PET-MRI contrast injection time	15:55 pm
MRI report	2.25 x 1.2 cm ill defined mass with irregular border
Biopsy date	04/19/2011
Pathology report	Invasive micropapillary carcinoma

Table 5.7: Overview of study parameters of patient 3

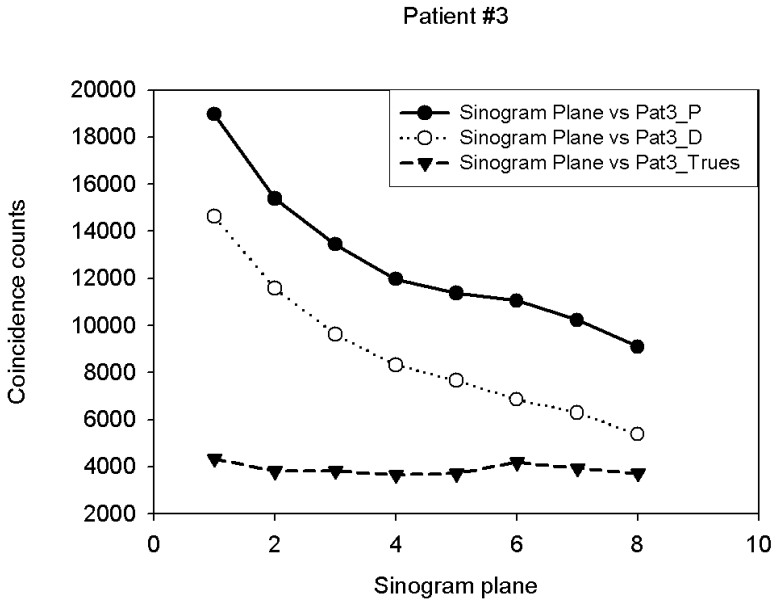

Figure 5.28: Random and true coincidences for "PET Only" condition as a function of sinogram plane - Patient 3

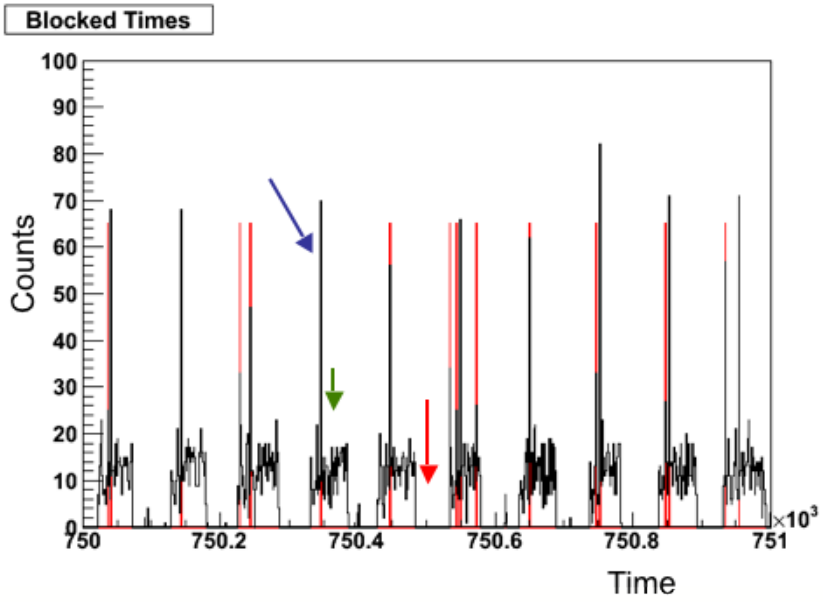

Figure 5.29: Spikes due to RF pulsing in PET data stream - patient 3, blue arrow - spikes, green arrow - RF off, red arrow - periodic dead time observed in this data stream

Summary - Patient3

Patient 3 was scanned using tungsten sheet shielding. This patient had silicone implants and this can be clearly seen in both the MRI and PET images. The primary lesion that was the target of imaging can be seen on slice 46 of Figure 5.32. However this lesion was too close to the chest wall for the PET coverage. Hence, other enhancing lesions in the breast were imaged. These lesions can be seen on the slices 51 and 53 of Figure 5.32. The PET data acquired during MRI pulsing show some periods of dead time along with the increased count rates as shown in Figure 5.29. The reason for this dead time is currently unclear. The reconstructed PET images (both PET only and simultaneous PET-MRI) in Figure 5.31 show presence of lesion(s) and lack of uptake defining the boundary of the implant. It can be seen clearly that the "PET only" image shows a very distinct region of uptake that correlates well with the MRI image as shown in Figure 5.33. However, the lesion is not as well defined in the simultaneous PET-MRI images. This could be due to the lower statistics due to data loss.

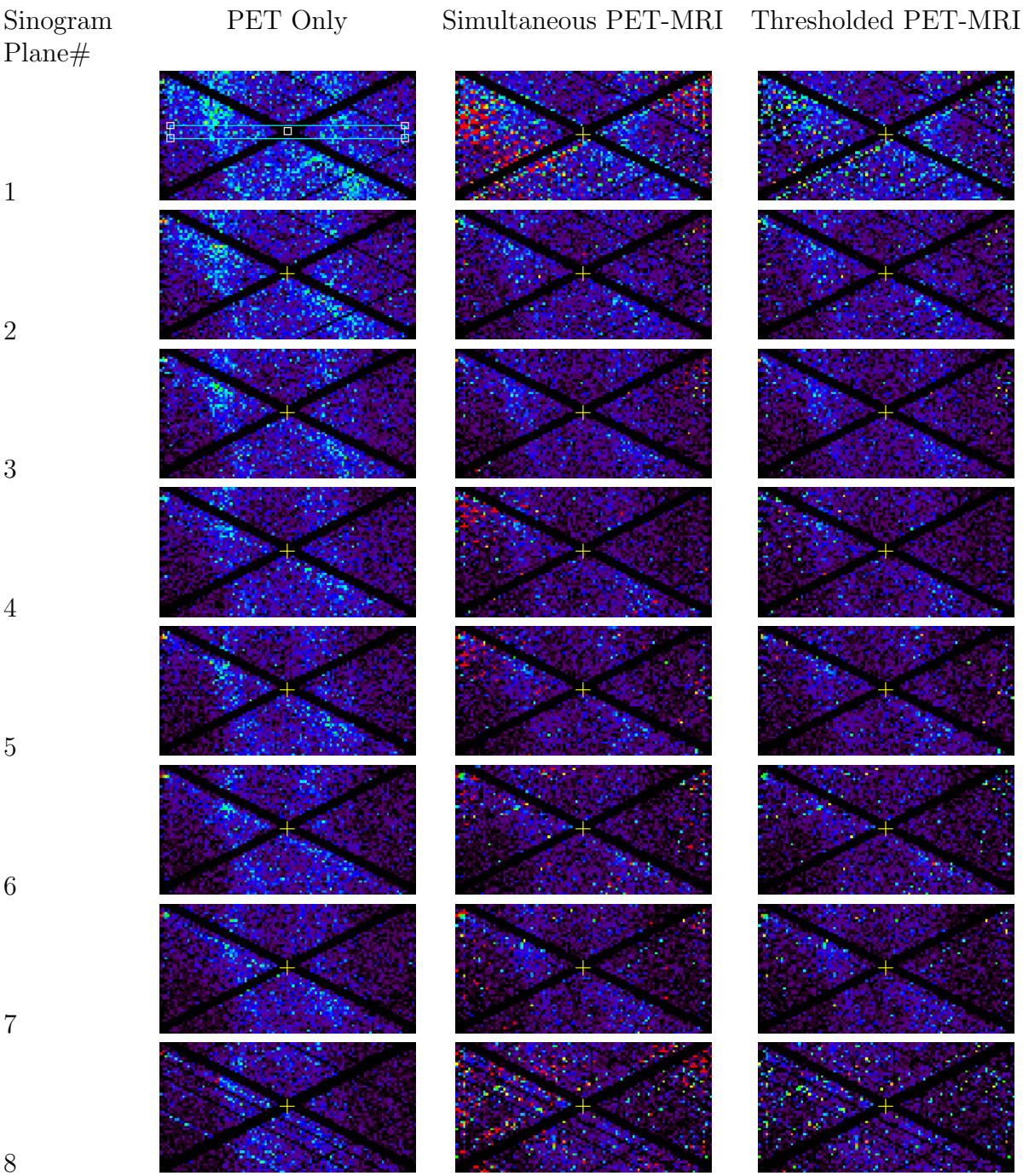

Figure 5.30: Sinograms for Patient 3

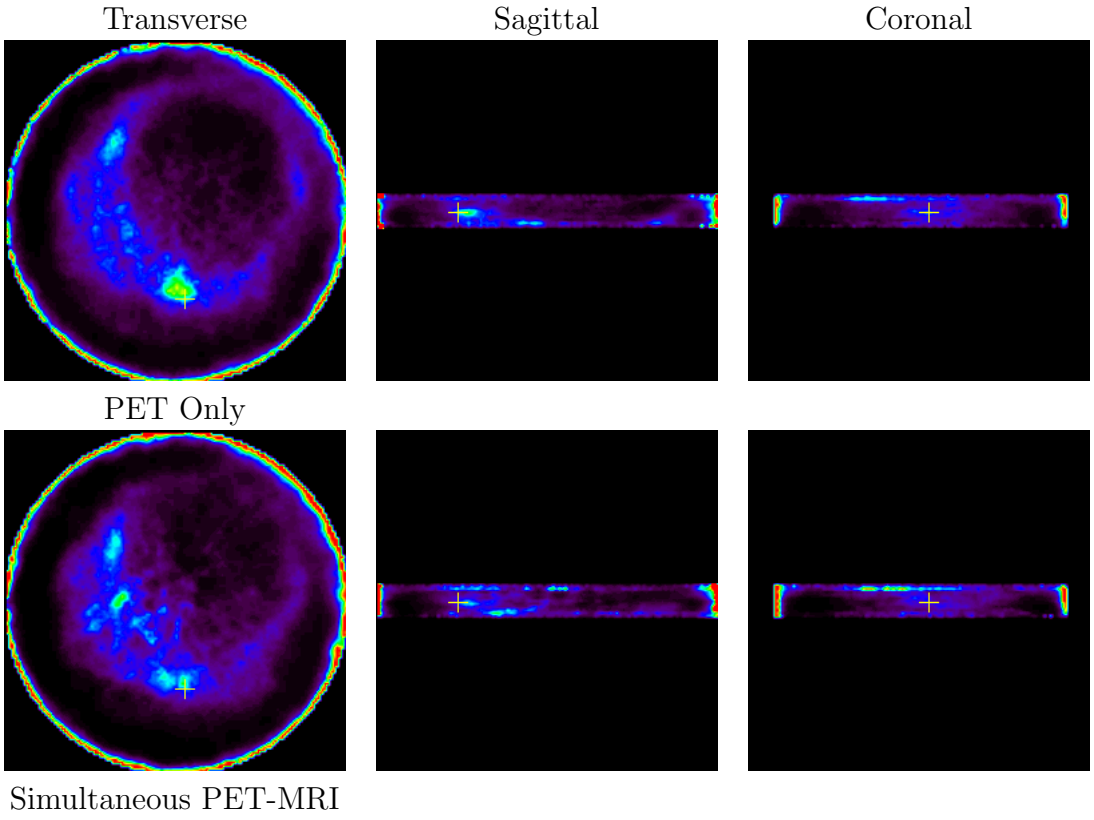

Figure 5.31: PET images - Patient 3

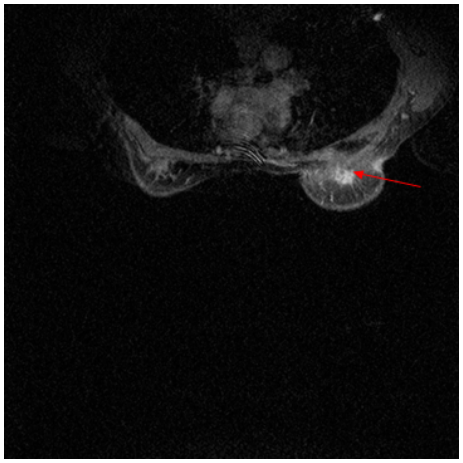

Slice 46 showing main lesion (red arrow)

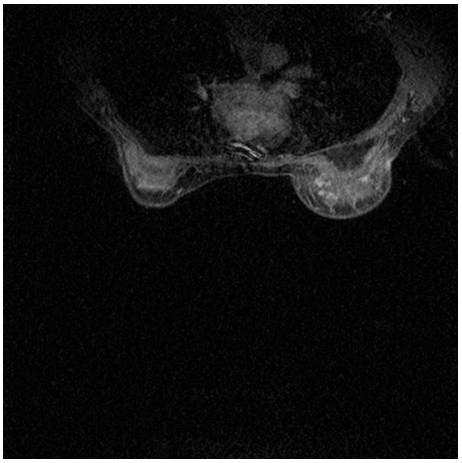

Slice 51

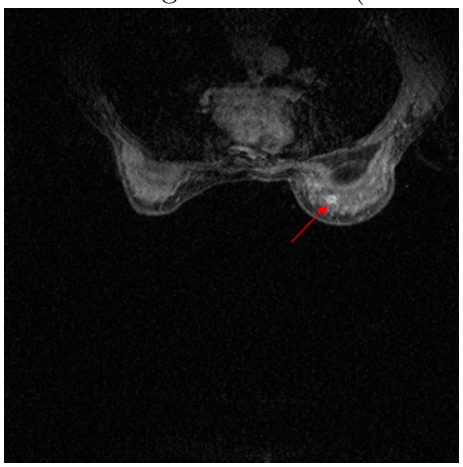

Slice 53

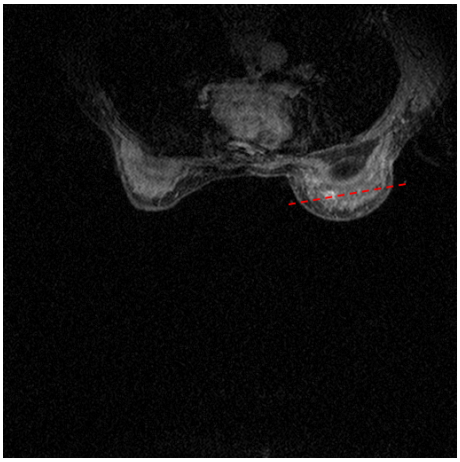

Slice 53 with PET centerline

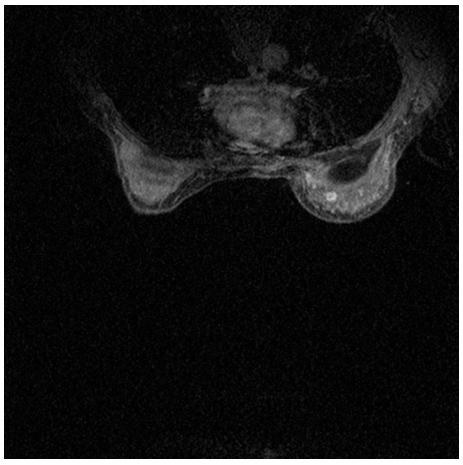

Slice 54

Figure 5.32: Patient 3, Post-contrast MRI

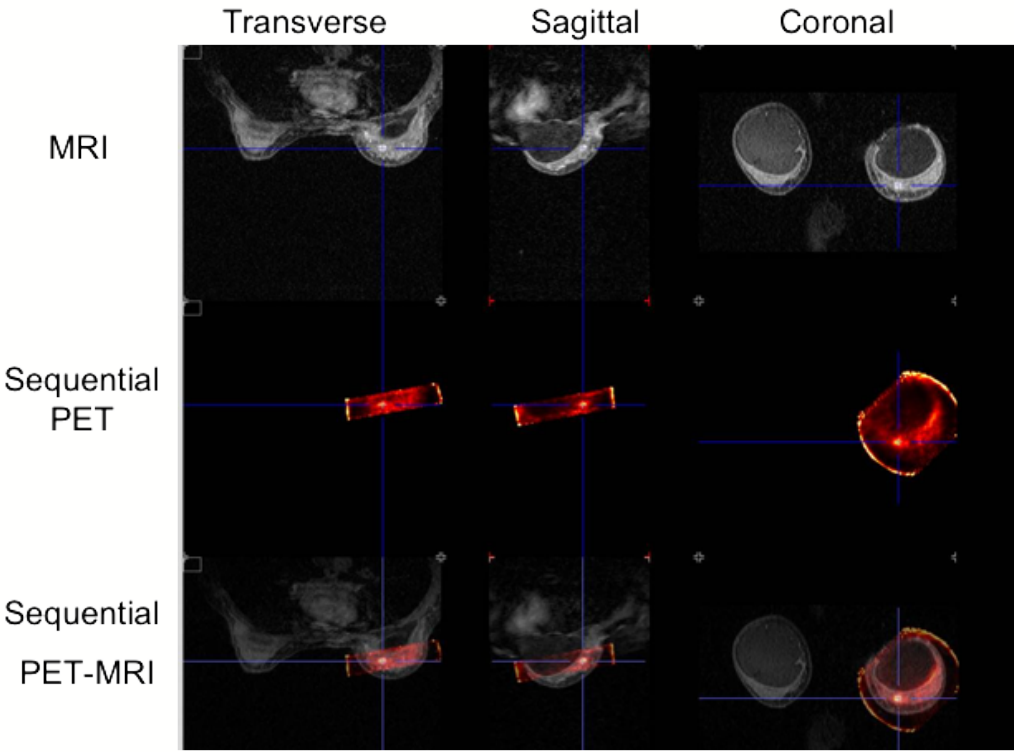

Figure 5.33: Sequential PET-MRI - Patient 3

5.5.4 Patient 4

Patient #4	
Date of PET-MRI	05/06/2011
Age	40 y
Injected dose	8.69 mCi
Time of radiotracer injection	13:47 pm
Whole body PET start time	14:50 pm
Prone PET start time	15:35 pm
PET-MRI contrast injection time	16:25 pm
MRI report	
Biopsy date	05/19/2011
Pathology report	Tubular adenoma (benign)

Table 5.8: Overview of study parameters of patient 4

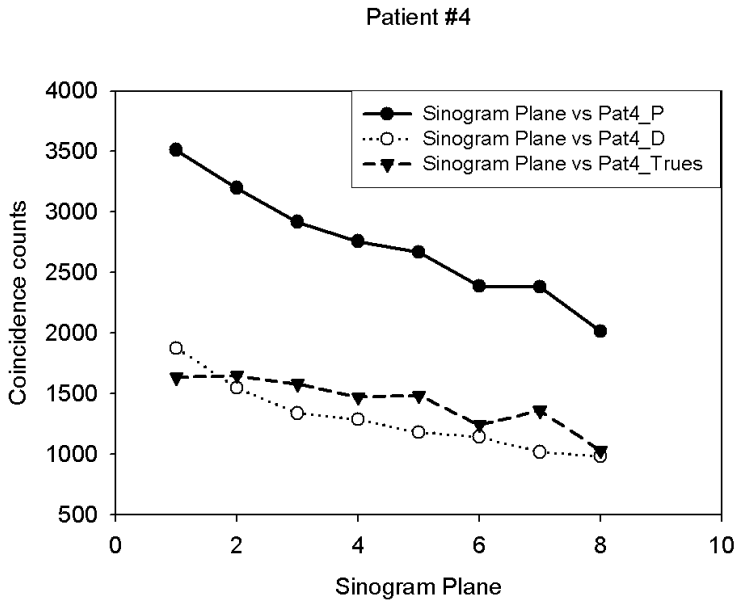

Figure 5.34: Random and true coincidences for "PET Only" condition as a function of sinogram plane - Patient 4

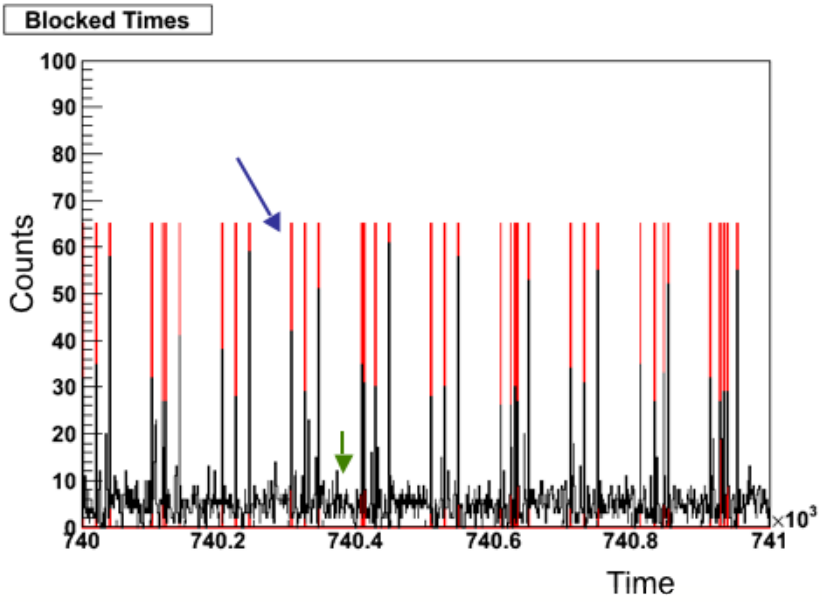

Figure 5.35: Spikes due to RF pulsing in PET data stream - patient 4, blue arrow - spikes, green arrow - RF off

Summary - Patient4

Patient 4 was scanned using a combination of both tungsten sheet shielding and lead glass. The suspected lesion or the tumor shows uptake that is seen as mild on prone whole body chest PET scan. The lesion is not discernible on the supine whole body PET scan. The prototype PET images show a region of distinct uptake as shown in Figure 5.37. A more well defined area is observed on the "PET only" image. Pathology report of the biopsied lesion shows the lesion to be benign and classified as tubular adenoma.

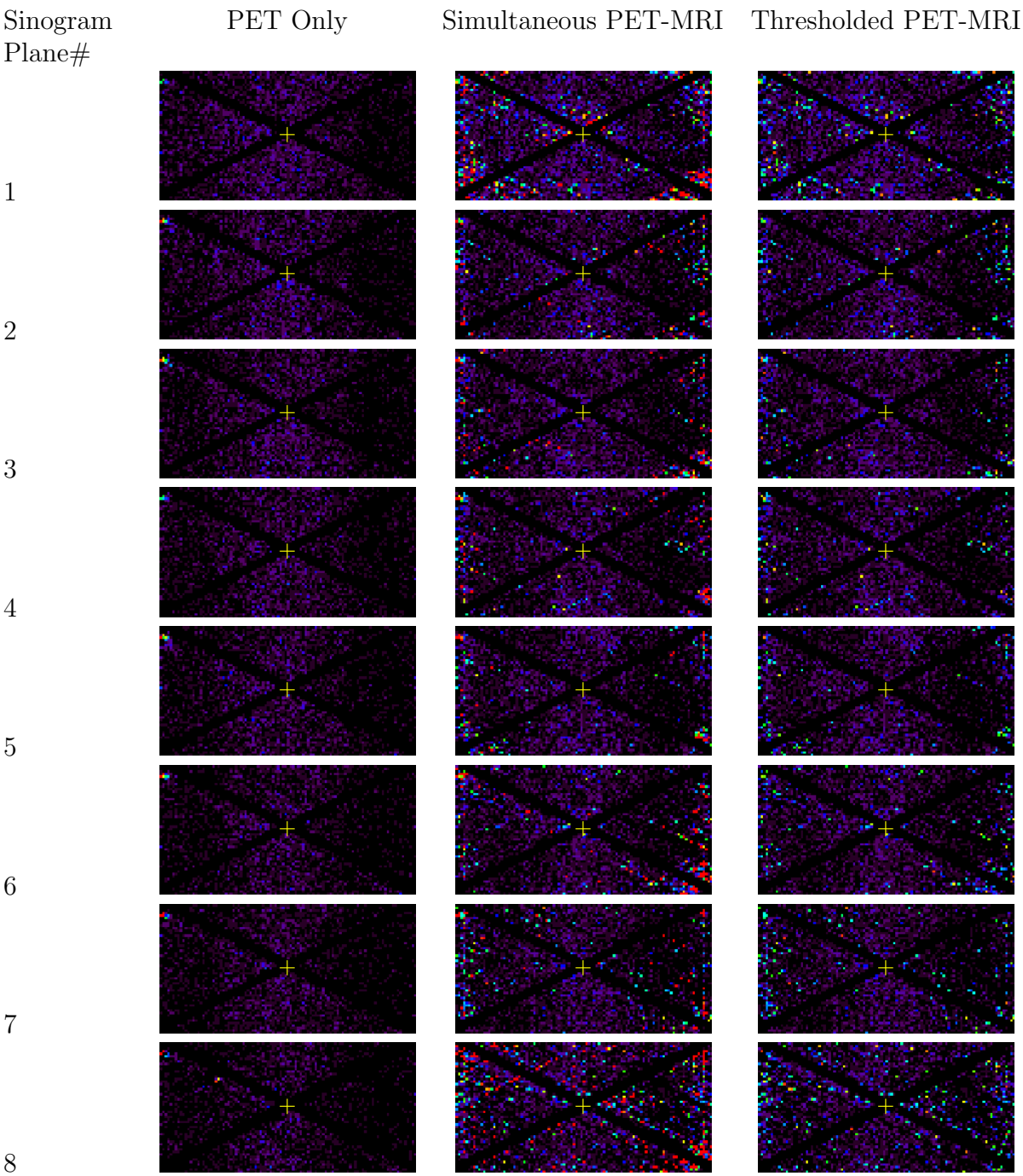

Figure 5.36: Sinograms for Patient 4

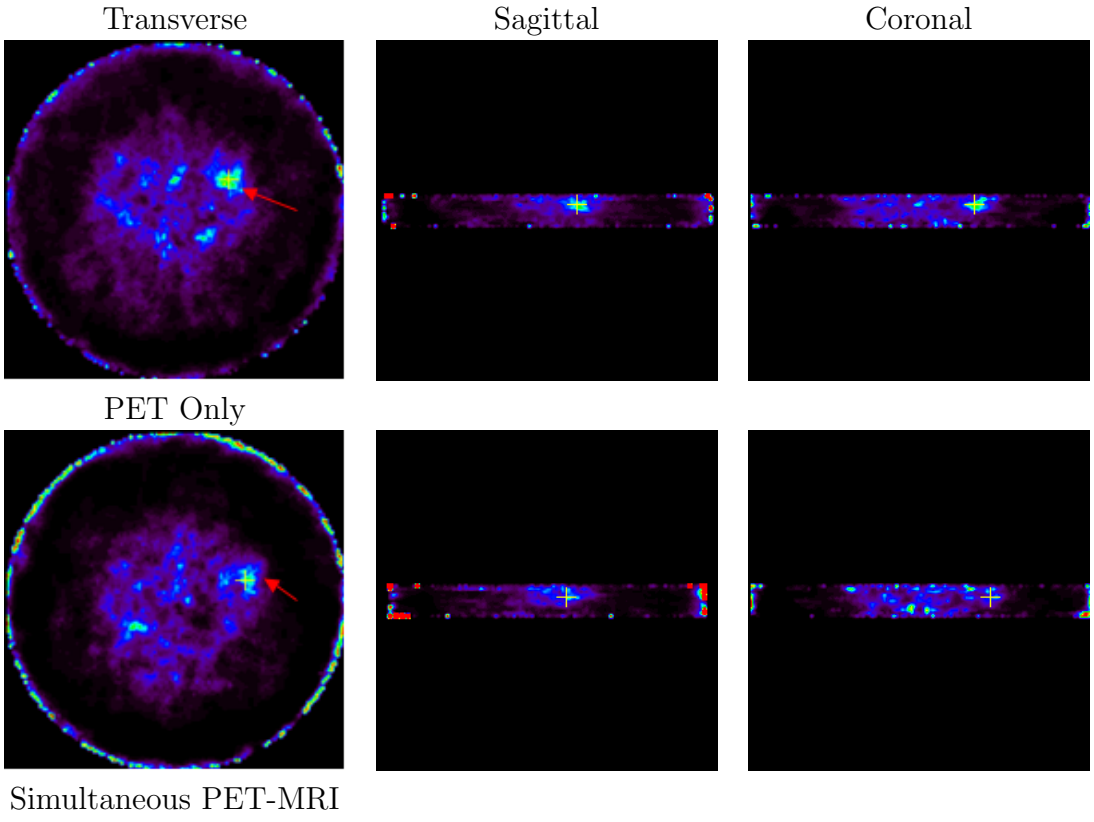

Figure 5.37: PET images - Patient 4

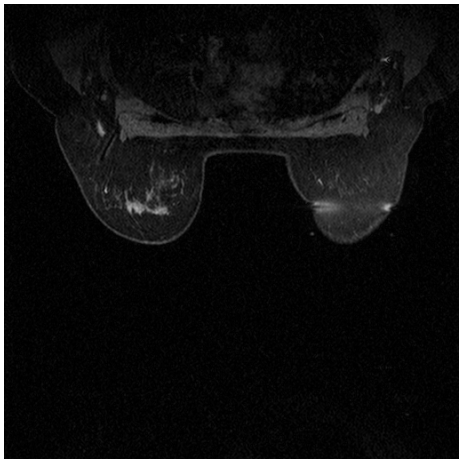

Slice 37

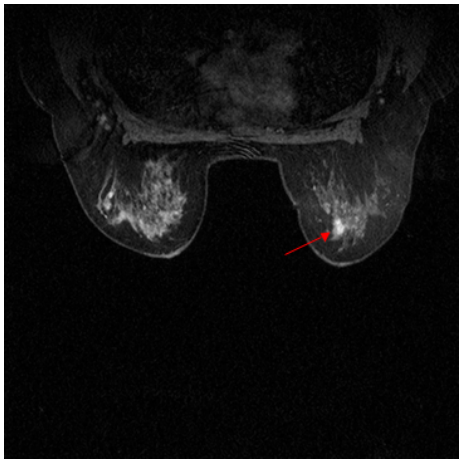

Slice 48

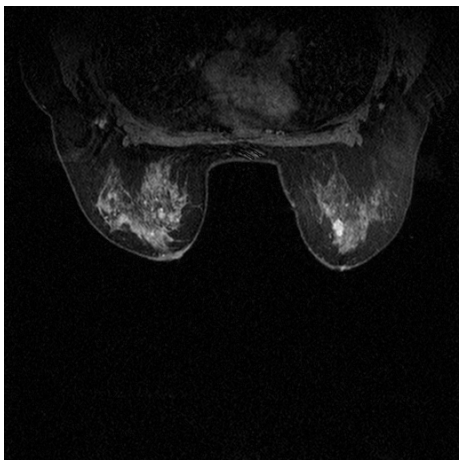

Slice 50

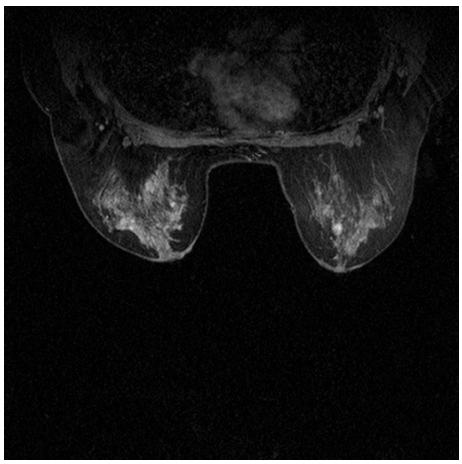

Slice 52

Figure 5.38: Patient 4, Post-contrast MRI

Chapter 6

Conclusions

Through the work of this thesis, the extension of RatCAP technology towards the development of a PET system for simultaneous PET-MRI imaging in human subjects was achieved. Several prototype versions of the scanner were constructed, and their performance evaluated on the bench and in the MRI environment [124, 125]. Through these tests, the feasibility of such a system was proven, as one could obtain good quality MRI images and PET data simultaneously. Problems related to interference noise in the MRI images due to the PET scanner were addressed through installation of filters for the PET power supplies, and by maintaining the integrity of the RF shielding of the MRI room. PET cooling was tapped off the MRI gradient coil's water cooling mechanism, and this allowed a contained system. Furthermore, components on the PET scanner that were magnetic and caused artifacts in the MRI images were replaced with non-magnetic ones (e.g.- the tin coated copper cables). In other cases, such as the magnetic data cable connectors, it was decided to continue testing with the potential signal loss due to time constraints. Nevertheless, non-magnetic versions of the data cable connectors are now available for replacement and have shown very good MRI compatibility. Hence, future versions of the scanner can have better MRI image quality. The use of the non-magnetic data cable connectors may potentially solve another problem of the simultaneous PET-MRI measurements - the increase in the PET count rate during RF pulsing since the connectors are part of the data transmission chain. This kind of interference is also present in the RatCAP small animal PET-MRI scanner. Currently, the way to work around this problem is to gate out the PET data acquired during the RF pulsing period of the MR sequence.

After successful tests using point sources and phantoms, a small scale clinical feasibility study was conducted. The goal of this study was to try out simultaneous PET-MRI breast imaging in patients with highly suspicious or biopsy proven breast cancer. A PET system was built that was optimized in its size to image the average Asian woman, as the clinical study was going to be conducted at the Taipei Medical University Hospital, Taiwan. The clinical PET prototype was assembled, tested and shipped to the Aurora breast imaging center at the Taipei Medical University Hospital. Simultaneous PET-MRI studies of 4 pa-

tients were conducted using the prototype system. Along with the simultaneous imaging, whole body PET in both the supine and prone position (chest only) were also acquired for comparison. The prototype PET system was also used to acquire PET only data (i.e. without MRI pulsing) after the simultaneous imaging concluded for each patient in order to directly compare the PET image quality in patients with and without MRI. The overlaid simultaneous PET-MRI images show very good agreement in the MRI depiction of the lesion and the PET FDG uptake. For one subject, the PET datastream during the MRI pulse sequence, suffered periodic data loss, which results in lower statistics and hence poorer image quality. The cause for this data loss during part of the pulse sequence is unknown. MRI Gradient switching may be an influencing factor, although such behavior has not been observed previously. It is well known from experience, that the PET data taking capability in the MRI is very much dependent on the correct orientation of the PET data cables, hence the orientation of the cables may play a part in this problem. Nevertheless, the feasibility of the prototype PET ring for breast cancer imaging was established, and its capability for simultaneous and sequential PET-MRI imaging looks promising. This is the first time a study of this kind has been conducted.

One of the main drawbacks observed for the PET system in its current configuration was the difficulty in imaging lesions that were close to the chest wall. This is an intrinsic limitation of the scanner geometry. Future tests should improve upon gamma shielding. In the tests conducted here, gamma shielding material was used to shield only the top surface of the ring. One could potentially shield all the surfaces of the ring except the one facing the imaging field of view. This could reduce the randoms contributions significantly thereby improving the PET image quality. However, MRI image quality degradation (if any) needs to be evaluated when making any such additions. Lead glass appears to be a good candidate for this purpose as it exhibited no artifacts.

A new version of the prototype breast scanner with a larger axial coverage is currently under development. This system has an axial height of approx. 5 cm, hence such a system will be able to be image a larger portion of the breast in a single imaging session and also have improved sensitivity. Monte Carlo simulations (Figure 6.1) carried out for this system show a coincidence sensitivity of 1.8%.

Apart from the breast imaging studies, arterial input function studies were also conducted using PET rings based on the same architecture as the breast PET system. Human studies were conducted using this system as well [126], wherein the time activity curve extracted from the artery of the human wrist was compared to the blood sampling data obtained simultaneously. These studies have established the feasibility of non-invasive determination of arterial input function by means of a PET scanner using various radioisotopes and scan configurations. Future work should involve focus on restricting or tracking movement of the wrist, after which, this system will be ready for routine clinical use.

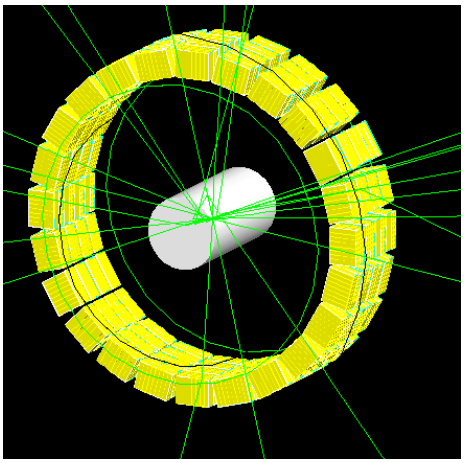

Figure 6.1: GATE model of the larger field of view prototype breast scanner

Bibliography

[1] W. L. Donegan and J. S. Spratt. *Cancer of the Breast*. Saunders, Philadelphia, Pa, 5th ed edition, 2003.

[2] D. J. Winchester et al. *Breast cancer*. PMPH USA, 2nd ed edition, 2005.

[3] D. Schulz et al. Simultaneous assessment of rodent behavior and neurochemistry using a miniature positron emission tomograph. *Nature Methods*, 8:347–352, 2011.

[4] http://www.spect.com/pub/Mini_and_Micro_Deluxe_Phantom_and_Hot_Spot_Insert.pdf.

[5] http://www.ezag.com/fileadmin/ezag/user-uploads/pdf/isotope/IPL_Multimodal_Sources.pdf.

[6] http://www.cancer.org/Cancer/BreastCancer/DetailedGuide/breast-cancer-survival-by-stage.

[7] T. F. Budinger. PET instrumentation: what are the limits? *Semin. Nucl. Med*, 28(3): 247–67, 1998.

[8] American cancer society: Cancer facts and figures 2011.

[9] Faina Nakhlis and Monica Morrow. Ductal carcinoma in situ. *Surgical Clinics of North America*, 83(4):821 – 839, 2003.

[10] Stephen A. Feig. Ductal carcinoma in situ: Implications for screening mammography. *Radiologic Clinics of North America*, 38(4):653 – 668, 2000.

[11] R. Holland et al. Extent, distribution, and mammographic/ histological correlations of breast ductal carcinoma in situ. *The Lancet*, 335(8688):519 – 522, 1990.

[12] Benjamin O. Anderson et al. Evolving concepts in the management of lobular neoplasia. *Journal of the National Comprehensive Cancer Network*, 4(5):511–522, 2006.

[13] Ramachandran Venkitaraman. Lobular neoplasia of the breast. *The Breast Journal*, 16(5):519–528, 2010.

[14] Peter T. Simpson et al. The diagnosis and management of pre-invasive breast disease: Pathology of atypical lobular hyperplasia and lobular carcinoma in situ. *Breast Cancer Research*, 5(5):258–262, 2003.

[15] V. Martinez and J. G. Azzopardi. Invasive lobular carcinoma of the breast: incidence and variants. *Histopathology*, 3(6):467–488, 1979.

[16] G. Arpino et al. Infiltrating lobular carcinoma of the breast: tumor characteristics and clinical outcome. *Breast Cancer Res.*, 6(3):149–156, 2004.

[17] Ingold JA. Borst MJ. Metastatic patterns of invasive lobular versus invasive ductal carcinoma of the breast. *Surgery*, 114(4):637–641, 1993.

[18] Luna-More S et al. Invasive micropapillary carcinoma of the breast. a new special type of invasive mammary carcinoma. *Pathol Res Practl*, 190(7):668–674, 1994.

[19] Ren L. Ridolfi et al. Medullary carcinoma of the breast. a clinicopathologic study with 10 year follow-up. *Cancer*, 40(4):1365–1385, 1977.

[20] S. B. Edge et al. *AJCC Cancer Staging Manual*. Springer, 7th ed edition, 2010.

[21] Y. Shen et al. Role of detection method in predicting breast cancer survival: analysis of randomized screening trials. *J Natl Cancer Inst*, 97(16):1195–203, 2005.

[22] K. Kerlikowske et al. Performance of screening mammography among women with and without a first-degree relative with breast cancer. *Ann Intern Med*, 133(11):855–63, 2000.

[23] L. Tabar et al. Recent results from the Swedish Two-County Trial: the effects of age, histologic type, and mode of detection on the efficacy of breast cancer screening. *J Natl Cancer Inst Monogr*, (22):43–7, 1997.

[24] E. Lidbrink et al. Neglected aspects of false positive findings of mammography in breast cancer screening: analysis of false positive cases from the Stockholm trial. *BMJ*, 312 (7026):273–6, 1996.

[25] D. B. Kopans et al. Positive predictive value of breast biopsy performed as a result of mammography: there is no abrupt change at age 50 years. Radiology. 200(2):357–60, 1996.

[26] A. R. Aro et al. False-positive findings in mammography screening induces short-term distress - breast cancer-specific concern prevails longer. *Eur J Cancer*, 36(9):1089–97, 2000.

[27] I. T. Gram, E. Lund, and S.E. Slenker. Quality of life following a false positive mammogram. *Br J Cancer*, 62(6):1018–22, 1990.

[28] A. R. Aro et al. Pain and discomfort during mammography. *Eur J Cancer A*, 32(10): 1674–9, 1996.

[29] R. Freitas 2nd et al. Discomfort and pain during mammography. *Rev Assoc Med Bras*, 52(5):333–6, 2006.

[30] P. J. Kornguth et al. Mammography pain in women treated conservatively for breast cancer. *J Pain*, 1(4):268–74, 2000.

[31] V.P. Jackson. The role of US in breast imaging. *Radiology*, 177(2):305–11, 1990.

[32] E. L. Rosen, W. B. Eubank, and D. A. Mankoff. FDG PET, PET/CT and Breast Cancer Imaging. *Radiographics*, 27(Suppl. 1):215–29, 2007.

[33] R. Kumar et al. Clinicopathologic factors associated with false negative FDG-PET in primary breast cancer. *Breast Cancer Research and Treatment*, 98:267–274, 2006.

[34] K. A. Miles and R. E. Williams. Warburg revisited: imaging tumour blood flow and metabolism. *Cancer Imaging*, 8:81–86, 2008.

[35] X. L. Zu and M. Gupy. Cancer metabolism: facts, fantasy and fiction. *Biochemical and Biophysical Research Communications*, 313:459–465, 2004.

[36] W. B. Eubank and D. A. Mankoff. Evolving role of positron emission tomography in breast cancer imaging. *Semin. Nucl. Med*, 35:84–99, 2005.

[37] M. Schelling et al. Positron emission tomography using [$^{1}8f$] fluorodeoxyglucose for monitoring primary chemotherapy in breast cancer. *Journal of Clinical Oncology*, 18 (8):1689–1695, 2000.

[38] L. K. Dunnwald et al. Tumor metabolism and blood flow changes by positron emission tomography: Relation to survival in patients treated with neoadjuvant chemotherapy for locally advanced breast cancer. *J Clinical Oncology*, 26(27):4449–4457, 2008.

[39] Ehab M. Kamel et al. [18f]-fluorodeoxyglucose positron emission tomography in patients with suspected recurrence of breast cancer. *Journal of Cancer Research and Clinical Oncology*, 129:147–153, 2003. ISSN 0171-5216. URL http://dx.doi.org/10.1007/s00432-003-0424-z. 10.1007/s00432-003-0424-z.

[40] J. E. Martimer et al. Metabolic flare: Indicator of hormone responsiveness in advanced breast cancer. *J Clin Oncology*, 19(11):2797–2803, 2001.

[41] A. K. Buck, H. Schirrmeister, T. Mattfeldt, and S. N. Reske. Biological characterisation of breast cancer by means of pet. *Eur J Nucl Med Mol Imaging*, 31(Suppl 1):80–7, 2004.

[42] R. Bos, J. J. van der Hoeven, E. van der Wall, P. van der Groep, et al. Biologic correlates of flourodeoxyglucose uptake in human breast cancer measured by positron emission tomography. *J. Clin. Oncol.*, 20:379–387, 2002.

[43] N. Avril et al. Glucose Metabolism of Breast Cancer Assessed by 18F-FDG PET: Histologic and Immunohistochemical Tissue Analysis. *J Nucl Med*, 42:9–16, 2001.

[44] D. Saslow et al. American Cancer Society guidelines for breast screening with MRI as an adjunct to mammography. *A Cancer Journal for Clinicians*, 57:75–89, 2007.

[45] N. H. Peters et al. Meta-analysis of MR imaging in the diagnosis of breast lesions. *Radiology*, 246(1):116–124, 2007.

[46] B. Erguvan-Dogan et al. BI-RADS-MRI: A Primer. *Am. J. Roentgenol.*, 187(2):W152–160, 2006.

[47] C. K. Kuhl. MRI of breast tumors. *European Radiology*, 10:46–58, 2000.

[48] S.C. Partridge et al. Association between serial dynamic contrast-enhanced MRI and dynamic 18F-FDG PET measures in patients undergoing neoadjuvant chemotherapy for locally advanced breast cancer. *Journal of Magnetic Resonance Imaging*, 32(5): 1124–1131, 2010.

[49] O. I. Craciunescu et al. DCE-MRI parameters have potential to predict response of locally advanced breast cancer patients to neoadjuvant chemotherapy and hyperthermia: A pilot study. *International Journal of Hyperthermia*, 25(6):405–415, 2009.

[50] S.C. Partridge et al. MRI Measurements of Breast Tumor Volume Predict Response to Neoadjuvant Chemotherapy and Recurrence-Free Survival. *Am. J. Roentgenol.*, 184 (6):1774–1781, 2005.

[51] C. E. Loo et al. Dynamic Contrast-Enhanced MRI for Prediction of Breast Cancer Response to Neoadjuvant Chemotherapy: Initial Results. *Am. J. Roentgenol.*, 191(5): 1331–1338, 2008. doi: 10.2214/AJR.07.3567.

[52] C. E. Loo et al. Magnetic Resonance Imaging Response Monitoring of Breast Cancer During Neoadjuvant Chemotherapy: Relevance of Breast Cancer Subtype. *Journal of Clinical Oncology*, 29(6):660–666, 2011.

[53] R. L. Wahl et al. Detection of breast cancer in women after augmentation mammoplasty using fluorine-18-fluorodeoxyglucose-PET. *J Nucl Med*, 35(5):872–5, 1994.

[54] F. Dehdashti et al. Positron tomographic assessment of estrogen receptors in breast cancer: comparison with FDG-PET and in vitro receptor assays. *J Nucl Med*, 36(10): 1766–74, 1995.

[55] W. J. Koh et al. Imaging of hypoxia in human tumors with [F-18]fluoromisonidazole. *Int J Radiat Oncol Biol Phys*, 22(1):199–212, 1992.

[56] L. M. Kenny et al. Quantification of cellular proliferation in tumor and normal tissues of patients with breast cancer by [18F]fluorothymidine-positron emission tomography imaging: evaluation of analytical methods. *Cancer Res*, 65(21):10104–12, 2005.

[57] L. Kenny et al. Imaging early changes in proliferation at 1 week post chemotherapy: a pilot study in breast cancer patients with 3'-deoxy-3'-[18F]fluorothymidine positron emission tomography. *Eur J Nucl Med Mol Imaging*, 34(9):1339–47, 2007.

[58] R. H. Mach et al. Sigma 2 receptors as potential biomarkers of proliferation in breast cancer. *Cancer Res*, 57(1):156–61, 1997.

[59] C. S. Dence et al. Synthesis and evaluation of [18F] labeled benzamides: high affinity sigma receptor ligands for PET imaging. *Nucl Med Biol*, 24(4):333–40, 1997.

[60] Z. Tu et al. Carbon-11 labeled sigma2 receptor ligands for imaging breast cancer. *Nucl Med Biol*, 32(5):423–30, 2005.

[61] J. M. Collins. *PET and Drug Development, in Principles and Practice of Positron Emission Tomography*. Lippincott Williams & Wilkins, 2002.

[62] J. M. Collins et al. *Imaging of drug accumulation as a guide to antitumor therapy*. The United States of America as represented by the Secretary of Health and Human Services: USA, 2007.

[63] Y. Ando et al. Diagnostic utility of tumor vascularity on magnetic resonance imaging of the breast. *Magn Reson Imaging*, 18(7):807–13, 2000.

[64] N. Avril et al. Metabolic characterization of breast tumors with positron emission tomography using F-18 fluorodeoxyglucose. *J Clin Oncol*, 14(6):1848–57, 1996.

[65] S. C. Huang. Anatomy of SUV. Standardized uptake value. *Nucl Med Biol*, 27(7): 643–6, 2000.

[66] J. Czernin. Clinical applications of FDG-PET in oncology. *Acta Med Austriaca*, 29 (5):162–70, 2002.

[67] Frederic H. Fahey. Data Acquisition in PET Imaging. *Journal of Nuclear Medicine Technology*, 30(2):39–49, 2002.

[68] NEMA. NEMA Standards Publication NU 2-2007 Performance Measurements of Positron Emission Tomographs. 2007.

[69] NEMA. NEMA Standards Publication NU 4-2008 Performance Measurements of Small Animal Positron Emission Tomographs. 2008.

[70] M. E. Phelps, editor. *PET: Physics, Instrumentation, and Scanners*, page 136. Springer, 1st ed edition, 2006.

[71] C.J. Thompson. Instrumentation for Positron Emission Mammography. *J CPET*, 1 (1):33–38, 2006.

[72] Habib Zaidi and Christopher Thompson. Evolution and Developments in Instrumentation for Positron Emission Mammography. *PET Clinics*, 4(4):317 – 327, 2009.

[73] Lawrence MacDonald et al. Clinical Imaging Characteristics of the Positron Emission Mammography Camera: PEM Flex Solo II. *Journal of Nuclear Medicine*, 50(10): 1666–1675, October 2009.

[74] W. Luo et al. Performance Evaluation of a PEM Scanner Using the NEMA NU 42008 Small Animal PET Standards. *Nuclear Science, IEEE Transactions on*, 57:94 – 103, 2010.

[75] Yibao Wu, Spencer L Bowen, Kai Yang, Nathan Packard, Lin Fu, George Burkett Jr, Jinyi Qi, John M Boone, Simon R Cherry, and Ramsey D Badawi. PET characteristics of a dedicated breast PET/CT scanner prototype. *Physics in Medicine and Biology*, 54(13):4273, 2009.

[76] M. C. Abreu et al. Clear-PEM: A dedicated pet camera for improved breast cancer detection. *Radiation Protection Dosimetry*, 116(1-4):208–210, 20 December 2005.

[77] M. C. Abreu et al. Clear-PEM: A PET imaging system dedicated to breast cancer diagnostics. *Nuclear Instruments and Methods in Physics Research Section A: Accelerators, Spectrometers, Detectors and Associated Equipment*, 571(1-2):81 – 84, 2007.

[78] T.G. Turkington et al. A large field of view positron emission mammography imager. *Nuclear Science Symposium Conference Record, 2002 IEEE*, pages 1883–1886, 2002.

[79] Raymond R Raylman et al. The positron emission mammography/tomography breast imaging and biopsy system (PEM/PET): design, construction and phantom-based measurements. *Physics in Medicine and Biology*, 53(3):637, 2008.

[80] P .D. Cutler et al. Design features and performance of a PET system for animal research. *J Nucl Med*, 33:595–604, 1992.

[81] B. E. Hammer. NMR-PET scanner apparatus. US Patent Number 4,939, 464, 1990.

[82] N.L. Christensen et al. Positron emission tomography within a magnetic field using photomultiplier tubes and lightguides. *Phys Med Biol*, 40:691–7, 1995.

[83] Y. Shao et al. Development of a PET detector system compatible with MRI/NMR systems. *IEEE Transactions on Nuclear Science*, 44:1167–1171, 1997.

[84] P. B. Garlick et al. PET and NMR dual acquisition (PANDA): applications to isolated, perfused rat hearts. *NMR Biomed*, 10:138–42, 1997.

[85] R. Slates et al. Design of a small animal MR compatible PET scanner. *IEEE Transactions on Nuclear Science*, 46:565–570, 1999.

[86] R. Lecomte et al. Performance characteristics of BGO-silicon avalanche photodiode detectors for PET. *IEEE Transactions on Nuclear Science*, 32:482–486, 1985.

[87] G. A. Petrillo et al. Scintillation detection with large-area reach-through avalanche photodiodes. *IEEE Transactions on Nuclear Science*, 31:417–423, 1984.

[88] R. Lecomte et al. Status of BGO-avalanche photodiode detectors for spectroscopic and timing measurements. *Nucl. Instrum. Meth. Phys. Res*, 278:585–597, 1989.

[89] R. Lecomte et al. High resolution positron emission tomography with a prototype camera based on solid state scintillation detectors. *IEEE Transactions on Nuclear Science*, 37:805–811, 1990.

[90] R. Lecomte et al. Initial results from the Sherbrooke avalanche photodiode positron tomograph. *IEEE Transactions on Nuclear Science*, 43:1952–1957, 1996.

[91] C. Schmelz et al. Feasibility study of an avalanche photodiode readout for a highresolution PET with nsec time resolution. *IEEE Transactions on Nuclear Science*, 42: 1080–1084, 1995.

[92] M. E. Casey et al. An LSO block detector for PET using an avalanche photodiode array. *IEEE Nuclear Science Symposium Conference Record*, 2:1105–1108, 1998.

[93] D. Schlyer et al. Development of a simultaneous PET/MRI scanner. *Nuclear Science Symposium Conference Record 2004 IEEE*, 6:3419–3421, 2004.

[94] B. J. Pichler et al. Lutetium oxyorthosilicate block detector readout by avalanche photodiode arrays for high resolution animal PET. *Phys Med Biol*, 49:4305–19, 2004.

[95] B. Pichler et al. Studies with a prototype high resolution PET scanner based onLSO-APD modules. *IEEE Transactions on Nuclear Science*, 45:1298–1302, 1998.

[96] B. Pichler et al. Performance test of a LSO-APD PET module in a 9.4 Tesla magnet. *IEEE Nuclear Science Symposium*, 2:1237–1239, 1997.

[97] M. S. Judenhofer et al. PET/MR images acquired with a compact MR-compatible PET detector in a 7-T magnet. *Radiology*, 244:807–14, 2007.

[98] D. Schlyer et al. A Simultaneous PET/MRI scanner based on RatCAP in small animals. *IEEE Nuclear Science Symposium Conference Record*, 5:3256–3259, 2007.

[99] S. H. Maramraju et al. An MR compatible PET scanner based on RatCAP for small animal imaging at 9.4 T. *IEEE Nuclear Science Symposium Conference Record*, pages 3679–3682, 2008.

[100] C. Catana et al. Simultaneous acquisition of multislice PET and MR images: initial results with a MR-compatible PET scanner. *J Nucl Med*, 47:1968–76, 2006.

[101] C. S. Levin et al. Investigation of position sensitive avalanche photodiodes for a new high-resolution PET detector design. *IEEE Transactions on Nuclear Science*, 51:805–810, 2004.

[102] Y. Yang et al. A prototype PET scanner with DOI-encoding detectors. *Journal of Nuclear Medicine*, 49:1132, 2008.

[103] K. C. Burr et al. Evaluation of a prototype small-animal PET detector with depth-of-interaction encoding. *IEEE Transactions on Nuclear Science*, 51:1791–1798, 2004.

[104] P. A. Dokhale et al. Performance measurements of a depth-encoding PET detector module based on position-sensitive avalanche photodiode read-out. *Physics in Medicine and Biology*, 49:4293–4304, 2004.

[105] Y. Yang et al. Depth of interaction resolution measurements for a high resolution PET detector using position sensitive avalanche photodiodes. *Physics in Medicine and Biology*, 51:2131–2142, 2006.

[106] V. Saveliev and V. Golovin. Silicon avalanche photodiodes on the base of metal-resistor-semiconductor (MRS) structures. *Nuclear Instruments and Methods in Physics Research Section A*, 442:223–229, 2000.

[107] A. N. Otte et al. A test of silicon photomultipliers as readout for PET. *Nuclear Instruments and Methods in Physics Research Section A*, 545:705–715, 2005.

[108] A.J. Lucas et al. Development of a combined microPET-MR system. *Technol Cancer Res Treat*, 5:337–41, 2006.

[109] K. M. Gilbert et al. Design of field-cycled magnetic resonance systems for small animal imaging. *Physics in Medicine and Biology*, 51:2825–2842, 2006.

[110] K. M. Gilbert et al. Evaluation of a positron emission tomography (PET)-compatible field-cycled MRI (FCMRI) scanner. *Magn Reson Med*, 62:1017–25, 2009.

[111] H Zaidi et al. Design and performance evaluation of a whole-body Ingenuity TF PET-MRI system. *Physics in Medicine and Biology*, 56(10):3091, 2011.

[112] P. Vaska et al. RatCAP: miniaturized head-mounted PET for conscious rodent brain imaging. *Nuclear Science, IEEE Transactions on*, 51(5):2718–2722, 2004.

[113] J. F. Pratte et al. The RatCAP Front-End ASIC. *IEEE Transactions on Nuclear Science*, 55:2727–2735, 2008.

[114] S. S. Junnarkar et al. Next Generation of Real Time Data Acquisition, Calibration and Control System for the RatCAP Scanner. *IEEE Transactions on Nuclear Science*, 55:220–224, 2008.

[115] S. H. Maramraju et al. Small animal simultaneous PET/MRI: initial experiences in a 9.4 T microMRI. *Physics in Medicine and Biology*, 56(8):2459, 2011.

[116] S. E. Harms et al. MR imaging of the breast with rotating delivery of excitation off resonance: clinical experience with pathologic correlation. *Radiology*, 187(2):493–501, 1993.

[117] S Jan et al. GATE: a simulation toolkit for PET and SPECT. *Physics in Medicine and Biology*, 49(19):4543–4561, 2004.

[118] W Segars. *Development of a new dynamic NURBS-based cardiac-torso(NCAT) phantom*. PhD thesis, University of North Carolina, 2001.

[119] T. Lewellen, R. Harrison, and S. Vannoy. *The SIMSET Program*, volume 20, page 77. IoP, 1999.

[120] M.D. Abramoff and others. Image processing with ImageJ. *Biophotonics International*, 11(7):36–42, 2004.

[121] S. Southekal et al. Quantitative PET Imaging Using a Comprehensive Monte Carlo System Model. *IEEE Transactions on Nuclear Science*, page 1, 2011.

[122] A. Kriplani et al. Feasibility studies for extracting an input function for quantitative positron emission tomography using a wrist scanner. *Nuclear Science Symposium Conference Record*, 6, 2007.

[123] D. Strul and others. Gamma shielding materials for MR-compatible PET. *Nuclear Science, IEEE Transactions on*, 50(1):60–69, Feb 2003.

[124] B. Ravindranath et al. A simultaneous PET/MRI breast scanner based on the RatCAP. *Nuclear Science Symposium Conference Record*, pages 4650 – 4655, 2008.

[125] B. Ravindranath et al. Results from prototype II of the BNL simultaneous PET-MRI dedicated breast scanner. *Nuclear Science Symposium Conference Record*, pages 3315 – 3317, 2009.

[126] B. Ravindranath et al. 3D tomographic wrist scanner for non-invasive determination of input function. *Nuclear Science Symposium Conference Record*, pages 2917 – 2919, 2009.